

**IMAGE FORMATION FROM SQUINT MODE SYNTHETIC APERTURE  
RADAR DATA**

By

Gordon W. Davidson

B. Sc. (Electrical Engineering) University of Calgary

M. Eng. (Systems and Computer Engineering) Carleton University

**A THESIS SUBMITTED IN PARTIAL FULFILLMENT OF  
THE REQUIREMENTS FOR THE DEGREE OF  
DOCTOR OF PHILOSOPHY**

in

**THE FACULTY OF GRADUATE STUDIES**

Department of

**ELECTRICAL ENGINEERING**

We accept this thesis as conforming  
to the required standard

---

**THE UNIVERSITY OF BRITISH COLUMBIA**

September 1994

© Gordon W. Davidson, 1994

In presenting this thesis in partial fulfillment of the requirements for an advanced degree at the University of British Columbia, I agree that the Library shall make it freely available for reference and study. I further agree that permission for extensive copying of this thesis for scholarly purposes may be granted by the head of my department or by his or her representatives. It is understood that copying or publication of this thesis for financial gain shall not be allowed without my written permission.

(Signature)

Department of Electrical Engineering

The University of British Columbia  
Vancouver, Canada

Date Sept. 19, 1994

## Abstract

The objective of this thesis is the investigation of image formation from squint mode, strip-map synthetic aperture radar (SAR) data, and the extension of the recently developed chirp scaling algorithm to accommodate problems in this type of imaging. In squint mode SAR, the antenna is pointed forward or backward of the perpendicular position used in conventional SAR, allowing different azimuth viewing angles of the surface. Squint mode has been used previously in spotlight SAR imaging, but signal characteristics and efficient signal processing for a spaceborne, strip-mapping squint mode SAR have not been thoroughly understood.

Several SAR processing algorithms are reviewed and analyzed to compare their processing errors at high squint and the type of operations they require. This includes the range-Doppler, squint imaging mode, polar format, wave equation and chirp scaling algorithms. In contrast to other algorithms, the chirp scaling algorithm does not require an interpolator in either the two-dimensional frequency domain or the range-Doppler domain, and it removes the range dependence of range cell migration correction (RCMC) efficiently by taking advantage of the properties of uncompressed linear FM pulses. Also, it achieves accurate processing for moderate squint angles by accommodating the azimuth-frequency dependence of secondary range compression (SRC).

Next, the properties of the squinted SAR signal are investigated to determine their effect on processing. A solution is presented for the yaw and pitch angles of the antenna which minimize the Doppler centroid variation with range and terrain height. The residual variation for a satellite platform is found to be negligible for an L-band SAR, while for C-band the variation was moderate and some accommodation in processing may be required. Then, the squinted beamwidth, which determines the azimuth bandwidth, is derived, and it is shown that choosing the yaw and pitch angles to minimize Doppler centroid variation results in an azimuth

bandwidth that is independent of range. The resulting azimuth bandwidth and pulse repetition frequency (PRF), as a function of squint angle, is used to derive a fundamental limit on the squint angle such that a received echo fits between adjacent transmitted pulses. For spaceborne SAR and a 40 km slant range swath, the squint angle is limited to about 35 degrees for L-band, and 50 degrees for C-band.

The chirp scaling algorithm is then investigated by analysis and simulation, and extended for processing high squint SAR data. The side-effects of chirp scaling include a range dependent range-frequency shift which may result in a loss of range bandwidth if frequency components are allowed to be shifted outside the window of the range matched filter.

The original chirp scaling algorithm approximates the range dependence of RCMC by assuming a constant  $B$  parameter in the distance equation for an orbital geometry. This causes a noticeable degradation in the point spread function for squint angles above about 15 degrees for L-band and 30 degrees for C-band. To provide accurate RCMC at high squint angles in an orbital geometry, the chirp scaling algorithm is extended so that the range dependence of the  $B$  parameter is accommodated in RCMC, by including a higher order term in the chirp scaling phase function.

Finally, the original chirp scaling algorithm neglects the range dependence of SRC, and this affects the quality of processing for squint angles above 10 degrees for L-band and 20 degrees for C-band. To solve this problem, the concept of nonlinear FM chirp scaling is introduced, in which a nonlinear FM component is incorporated into the received range signal which interacts with chirp scaling to remove the range dependence of SRC. This allows accurate processing of strip map SAR data for squint angles up to the limitations imposed by the SAR imaging constraints. Two methods of nonlinear FM chirp scaling are introduced. The nonlinear FM filtering method introduces the nonlinear FM component by an extra filtering step during processing, and is more accurate. The nonlinear FM pulse method incorporates the component into the transmitted pulse, thus requiring no extra computation, although it is slightly less accurate. The processing errors of both methods are analyzed and the expected performance is verified by the processing

of simulated point scatterer data. In addition, conventional spaceborne SAR data from Seasat was skewed to emulate the signal from a high squint SAR, and processed with the original chirp scaling algorithm and the nonlinear FM chirp scaling algorithm. The resulting images show the improvement in range resolution with nonlinear FM chirp scaling.

## Table of Contents

<b>Abstract</b>	<b>ii</b>
<b>Table of Contents</b>	<b>v</b>
<b>List of Tables</b>	<b>ix</b>
<b>List of Figures</b>	<b>xi</b>
<b>List of Symbols</b>	<b>xiv</b>
<b>Acknowledgement</b>	<b>xviii</b>
<b>1 Introduction</b>	<b>1</b>
1.1 Background . . . . .	1
1.1.1 SAR in Remote Sensing . . . . .	1
1.1.2 SAR Processing . . . . .	3
1.1.3 Squint Mode SAR . . . . .	4
1.2 Thesis Objectives . . . . .	6
<b>2 Theory of SAR Imaging</b>	<b>8</b>
2.1 Introduction . . . . .	8
2.2 SAR Signal Model . . . . .	8
2.2.1 Point Scatterer Response . . . . .	8
2.2.2 Orbital Geometry . . . . .	14
2.2.3 SAR Constraints . . . . .	16
2.3 Pulse Compression . . . . .	17

2.3.1	Matched Filter . . . . .	17
2.3.2	Compression Error . . . . .	20
2.4	Exact SAR Correlation . . . . .	21
2.4.1	Time Domain Correlation . . . . .	21
2.4.2	Frequency Domain Correlation . . . . .	22
2.4.3	Point Spread Function . . . . .	24
2.5	Image Resampling . . . . .	26
<b>3</b>	<b>SAR Processing Algorithms</b>	<b>27</b>
3.1	Introduction . . . . .	27
3.2	Range-Doppler Domain Algorithms . . . . .	27
3.2.1	Mathematical Formulation . . . . .	27
3.2.2	Range-Doppler With SRC . . . . .	30
3.2.3	Squint Imaging Mode Algorithm . . . . .	31
3.2.4	Time Domain SRC . . . . .	33
3.3	Polar Format Algorithm . . . . .	34
3.4	Wave Equation Algorithms . . . . .	37
3.4.1	Stolt Interpolation . . . . .	37
3.4.2	Approximations . . . . .	39
3.5	Chirp Scaling Algorithm . . . . .	40
<b>4</b>	<b>Considerations for High Squint</b>	<b>48</b>
4.1	Introduction . . . . .	48
4.2	Doppler Centroid Variation . . . . .	48
4.2.1	Squint Angle Derivation . . . . .	48
4.2.2	Minimization of Doppler Centroid Variation . . . . .	52
4.3	Signal Properties . . . . .	58
4.3.1	Squinted Beamwidth . . . . .	58

4.3.2	SAR Signal Constraints . . . . .	62
4.4	Stop-Start Assumption . . . . .	66
4.5	Signal Model for SAR Processing . . . . .	69
4.6	Spectrum and Point Spread Function . . . . .	73
4.6.1	Data Spectrum . . . . .	73
4.6.2	Image Spectrum . . . . .	76
<b>5</b>	<b>Investigation of Chirp Scaling</b>	<b>78</b>
5.1	Introduction . . . . .	78
5.2	Comparison with Range-Doppler . . . . .	78
5.2.1	Image Quality At Low Squint . . . . .	78
5.2.2	Azimuth Frequency Dependence of SRC . . . . .	86
5.3	Side-Effects of Chirp Scaling . . . . .	89
5.4	Approximations in Chirp Scaling . . . . .	91
5.4.1	Constant $B$ Assumption . . . . .	91
5.4.2	Constant Range Frequency Rate Assumption . . . . .	93
5.4.3	Linear FM Assumption . . . . .	95
5.4.4	Simulations . . . . .	98
5.5	Effect of Pulse Phase Errors . . . . .	101
<b>6</b>	<b>Extensions to Chirp Scaling for RCMC</b>	<b>105</b>
6.1	Introduction . . . . .	105
6.2	Representation of Desired Trajectory . . . . .	105
6.3	Higher Order Chirp Scaling . . . . .	108
<b>7</b>	<b>Nonlinear FM Chirp Scaling for Range-Variant SRC</b>	<b>112</b>
7.1	Introduction . . . . .	112
7.2	Nonlinear FM Filtering Method . . . . .	114
7.2.1	Description . . . . .	114

7.2.2	Limitations . . . . .	120
7.2.3	Computation . . . . .	124
7.3	Nonlinear FM Pulse Method . . . . .	129
7.3.1	Description and Limitations . . . . .	129
7.3.2	Accommodation of Error in Squint Estimate . . . . .	132
7.3.3	Effect of Pulse Doppler Shift . . . . .	135
7.4	Simulations . . . . .	137
7.5	Experiments With Skewed Seasat Data . . . . .	142
7.5.1	Approach . . . . .	142
7.5.2	Signal Model . . . . .	144
7.5.3	Results . . . . .	147
<b>8</b>	<b>Conclusion</b>	<b>150</b>
8.1	Summary . . . . .	150
8.2	Contributions . . . . .	156
8.3	Further Work . . . . .	157
	<b>Bibliography</b>	<b>158</b>
<b>A</b>	<b>Approximation to Inverse Fourier Transform With Cubic Phase Term</b>	<b>162</b>
<b>B</b>	<b>Approximation to Fourier Transform With Higher Order Phase Terms</b>	<b>164</b>
<b>C</b>	<b>Approximation to Fourier Transform With General Pulse Phase Error</b>	<b>168</b>

## List of Tables

2.1	Peak phase error in compressed pulse due to compression error. . . . .	20
4.2	Spaceborne SAR parameters. . . . .	55
4.3	Azimuth bandwidth versus squint: Yaw rotation only; and with optimal yaw and pitch. . . . .	62
4.4	Maximum azimuth phase error at the edge of the aperture for hyperbolic fit to distance equation at beam center time. . . . .	73
5.5	Average resolution and integrated sidelobe ratio for range-Doppler and chirp scaling processors, and mean and standard deviation of difference in peak phase. . . . .	86
5.6	Registration and in-band RCMC errors (in range cells) due to constant $B$ approximation in the desired trajectory in the chirp scaling algorithm. . . . .	93
5.7	Registration and in-band RCMC errors (in range cells) in the chirp scaling due to range dependence of $K_m$ . . . . .	95
5.8	Maximum quadratic phase error in SRC due to its range-dependence. . . . .	96
5.9	Errors due to cubic phase term in SAR transfer function, L-band. . . . .	98
5.10	Errors due to cubic phase term in SAR transfer function, C-band. . . . .	99
5.11	Simulation results of maximum sidelobe level in the range direction for the chirp scaling algorithm with scatterer at different distances from the reference range. . . . .	100
5.12	Registration and RCMC errors (in cells) due to chirp scaling with quadratic phase error in pulse. L-band and C-band spaceborne SAR parameters, with $(r - r_{ref}) = 20km$ . . . . .	103

6.13	Maximum RCMC error (in range cells) due to the approximation to desired trajectory when using only modified linear scaling, and when using both linear and quadratic scaling. . . . .	108
7.14	Maximum phase and RCMC errors for nonlinear FM chirp scaling. . . . .	123
7.15	Maximum phase and RCMC errors for nonlinear FM chirp scaling. . . . .	123
7.16	Percent change in range bandwidth and percent range-frequency shift due to chirp scaling with nonlinear FM filtering method. . . . .	125
7.17	Side-effects of chirp scaling and error due to approximation in the nonlinear FM pulse method: Change in range bandwidth, range-frequency shift, and maximum quadratic phase error at azimuth band edge. . . . .	132
7.18	Side-effects of chirp scaling and error due to approximation in the nonlinear FM pulse method: Change in range bandwidth, range-frequency shift, and maximum quadratic phase error at azimuth band edge. . . . .	132
7.19	Side-effects and maximum phase error with $f_{\eta r}$ changed to accommodate a $\pm 1$ degree squint estimate error. . . . .	135
7.20	Side-effects and maximum phase error with $f_{\eta r}$ changed to accommodate a $\pm 1$ degree squint estimate error. . . . .	136
7.21	Simulation results of measured maximum sidelobe level of point spread function in range direction: nonlinear FM filtering method and nonlinear FM pulse method.	140
7.22	Simulation results of measured range registration error of point spread function: nonlinear FM filtering method and nonlinear FM pulse method. . . . .	141
7.23	Simulation results of measured phase error at expected peak sample of point spread function: nonlinear FM filtering method and nonlinear FM pulse method.	142

## List of Figures

2.1	General SAR imaging geometry. . . . .	9
2.2	Point scatterer response. . . . .	13
2.3	Effect of a quadratic phase error in pulse compression. . . . .	21
2.4	Contour plots of two-dimensional amplitude spectrum and point spread function for small squint. . . . .	25
3.5	Aliased range migration curves with Doppler centroid variation. . . . .	33
3.6	Range migration trajectories in chirp scaling. . . . .	42
3.7	Frequency-time diagram of range line with linear FM pulses. . . . .	44
3.8	Block diagram of chirp scaling algorithm. . . . .	46
4.9	Coordinate system showing elevation and squint of vector pointing from antenna to scatterer. . . . .	49
4.10	Orbital geometry. . . . .	54
4.11	Doppler centroid error versus squint, due to range variation and height variation, at near incidence. Solid curve indicates zero degree antenna pointing error, dashed curve indicates $\pm 0.5$ degree error, and dot-dash curve indicates $\pm 1$ degree error. . . . .	56
4.12	Doppler centroid error versus squint, due to range variation and height variation, at far incidence. Solid curve indicates zero degree antenna pointing error, dashed curve indicates $\pm 0.5$ degree error, and dot-dash curve indicates $\pm 1$ degree error. . . . .	57
4.13	Squinted beamwidth. Illustration of elevation angles at beam edges before and after squinting. . . . .	59
4.14	Transmitted pulses and received echo. . . . .	63

4.15	Closest approach range swath versus squint for L-band and C-band and for near and far incidence. $T_{sp} = 200\mu s$ . Solid lines: antenna length $L = 10.5m$ . Dashed lines: antenna length $L = 12m$ . . . . .	65
4.16	Path travelled by pulse without stop-start assumption. . . . .	67
4.17	Illustration of actual distance equation, hyperbolic fit at closest approach time, and hyperbolic fit at beam center. . . . .	71
4.18	Skewed region of support of data spectrum. . . . .	75
4.19	Replication of parts of spectrum to expand azimuth bandwidth. . . . .	75
4.20	Contour plots of image spectrum and point spread function after range variant processing. . . . .	77
5.21	Seasat Goldstone scene processed with range-Doppler algorithm. . . . .	80
5.22	Seasat Goldstone scene processed with chirp scaling algorithm. . . . .	81
5.23	Range slice of point spread function for range-Doppler algorithm. . . . .	82
5.24	Azimuth slice of point spread function for range-Doppler algorithm. . . . .	83
5.25	Range slice of point spread function for chirp scaling algorithm. . . . .	84
5.26	Azimuth slice of point spread function for chirp scaling algorithm. . . . .	85
5.27	Contour plot of point spread function for range-Doppler algorithm, spaceborne L-band parameters, zero and 10 degree squint. . . . .	87
5.28	Range resolution versus squint for range-Doppler and chirp scaling algorithms. Scatterer at reference range. Top: L-band. Bottom: C-band. . . . .	88
5.29	Simulation results of measured range resolution versus squint for chirp scaling algorithm with scatterer at different distances from the reference range. Top: L-band. Bottom: C-band. . . . .	100
7.30	Frequency-time diagram of range line with nonlinear FM pulses. . . . .	113
7.31	Block diagram of nonlinear FM filtering method. . . . .	116

7.32	Time domain filter length required for less than 3 percent broadening, versus maximum quadratic phase error in degrees. . . . .	126
7.33	Computation of time domain SRC filter (t-d) versus frequency domain cubic phase filtering step (fft). Top: L-band SAR at squint angles of 20 and 40 degrees. Bottom: C-band SAR at squint angles of 30 and 50 degrees. . . . .	128
7.34	Contour plots of point spread functions for L-band at 25° squint, $(r - r_{ref}) = 20km$ , using original chirp scaling algorithm, nonlinear FM filtering method, and nonlinear FM pulse method. . . . .	139
7.35	Simulation results of measured range resolution in cells vs. squint angle in degrees: (1) original chirp scaling algorithm; (2) nonlinear FM filtering method; and (3) nonlinear FM pulse method. . . . .	140
7.36	Magnitude of range slice of point spread function for L-band at 35° squint, $(r - r_{ref}) = 20km$ , using nonlinear FM chirp scaling: filtering method and pulse method. . . . .	143
7.37	Magnitude of range slice of point spread function for C-band at 50° squint, $(r - r_{ref}) = 20km$ , using nonlinear FM chirp scaling: filtering method and pulse method. . . . .	143
7.38	Illustration of skewed SAR data. . . . .	145
7.39	Image of Vancouver scene formed from skewed data with the original chirp scaling algorithm, with the reference range 20 km from the center of the image. . . . .	148
7.40	Image of Vancouver scene formed from skewed data with the nonlinear FM chirp scaling algorithm, with the reference range 20 km from the center of the image. . . . .	149
7.41	Image of Vancouver scene formed from skewed data with the original chirp scaling algorithm, with the reference range at the center of the image. . . . .	149

## List of Symbols

$\alpha_r$	angle from orbital plane to scatterer
$\alpha, \alpha_B$	scale factors in chirp scaling
$\beta$	higher order scale factor in chirp scaling
$\gamma(f_\eta; r)$	factor relating range to range migration trajectory
$\gamma_e, \gamma_i$	elevation angle of antenna
$\psi$	yaw angle
$\Delta\psi$	yaw interval in beam
$\delta$	pitch angle
$\varepsilon$	pulse phase error
$\phi_p$	transmitted pulse phase
$\Phi_p$	phase of pulse spectrum
$\Phi$	SAR focussing phase of SAR transfer function
$\phi_0, \phi_1, \phi_2, \phi_3$	phase coefficients of SAR transfer function
$\phi_{err}$	processing phase error in SAR transfer function
$\phi_\Delta$	phase correction in chirp scaling
$\lambda$	wavelength
$\theta$	squint angle
$\theta_s$	instantaneous squint angle
$\Delta\theta$	squinted beamwidth
$\eta$	azimuth-time
$\eta_0, \eta_i$	closest approach azimuth-time
$\eta_c$	beam center offset time
$\Delta\eta$	exposure time
$\eta_a$	reference azimuth-time in polar algorithm
$\eta_h$	azimuth-time offset in hyperbolic model

$\eta_{ref}$	reference azimuth-time for skewing raw data
$\sigma$	scatterer reflectivity
$\hat{\sigma}$	processed image of reflectivity
$\tau$	range travel-time
$\tau_d, \tau_{ref}$	range migration trajectories
$\tau_s$	desired trajectory in chirp scaling
$\hat{\tau}_s$	scaled trajectory after chirp scaling
$\Delta\tau$	range migration relative to reference trajectory
$\tau_{Berr}, \tau_{Ks}$	range migration correction errors
$A(f_\eta, f_\tau)$	amplitude of SAR transfer function
$B, B_h$	parameter of hyperbolic distance equation
$B_r, B_s, B_a$	coefficients of $B$ polynomial in range
$c$	speed of light
$\Delta C, \Delta C_m$	cubic phase error coefficients
$f_0$	carrier frequency
$f_a$	azimuth-frequency variable in polar algorithm
$f_\eta$	azimuth-frequency
$f_{\eta c}$	Doppler centroid
$f_{\eta r}$	reference azimuth-frequency
$\Delta f_\eta$	azimuth bandwidth
$f_{\eta cs}$	Doppler centroid of skewed data
$\Delta f_{\eta cr}$	Doppler centroid variation in range
$\Delta f_{\eta ch}$	Doppler centroid variation in terrain height
$f_\tau$	range-frequency
$\delta f_\tau$	range-frequency shift due to chirp scaling
$\Delta f_\tau$	pulse bandwidth
$f_t$	range frequency variable in image dimension

$F_{ac}(f_\eta; r)$	conjugate of azimuth compression filter
$G_p, G$	complex constants
$H$	radius of platform orbit
$h$	platform altitude
$h(\eta, \tau; r)$	point spread function
$K$	range frequency rate
$K_m, K_{mref}$	modified range frequency rate
$K_s, K_{s0}$	slope of range frequency rate
$\Delta K$	frequency rate error
$L$	antenna length in azimuth
$m(\tau)$	transmitted pulse amplitude
$M(f_\tau)$	amplitude of pulse spectrum
$n_{ops}$	number of complex multiplications
$o_s$	oversampling rate
PRF	pulse repetition frequency
$p(\tau)$	transmitted pulse
$P(f_\tau)$	pulse spectrum
$q_2, q_3$	coefficients of chirp scaling phase function
RCMC	range cell migration correction
$R$	instantaneous platform to scatterer distance
$R_\Delta$	azimuth varying part of $R$
$R_p$	platform to scatterer distance including platform motion
$R_s$	effective $R$ for skewed data
$R_h$	hyperbolic model of $R$ for skewed data
$r_s$	slope of skew in skewed data
$r_e$	radius of earth
$r_0, r$	closest approach range

$r_{ref}$	reference range
$r_h$	closest approach range in hyperbolic model
$\Delta r$	range swath width
$\delta r$	spatial range resolution
SAR	synthetic aperture radar
SRC	secondary range compression
$S(f_\eta, \tau; r)$	range-Doppler representation of signal
$S_\alpha(f_\eta, \tau; r)$	range-Doppler representation of chirp scaled signal
$S_Y(f_\eta, \tau; r)$	range-Doppler representation of filtered signal
$S_{Y\alpha}(f_\eta, \tau; r)$	range-Doppler representation of filtered, chirp scaled signal
$S_2(f_\eta, f_\tau; r)$	SAR transfer function
$S_{2\alpha}(f_\eta, f_\tau; r)$	SAR transfer function of chirp scaled signal
$S_{2Y}(f_\eta, f_\tau; r)$	SAR transfer function of filtered signal
$S_{2Y\alpha}(f_\eta, f_\tau; r)$	SAR transfer function of filtered, chirp scaled signal
$T$	transmitted pulse length
$T_m$	pulse length in range-Doppler domain
$T_{sp}$	guard space between transmitted pulses
$t_0, t_i$	closest approach range-time
$t_a$	reference range-time in polar algorithm
$v$	platform velocity
$v_g$	ground velocity of antenna footprint
$w(\eta)$	antenna pattern
$W(f_\eta)$	azimuth frequency weighting from antenna pattern
$\delta x$	spatial azimuth resolution
$Y, Y_c$	cubic phase coefficient
$Y_m, Y_{mc}$	modified cubic phase coefficient

## Acknowledgement

I would like to thank my supervisors, Dr. Cumming and Dr. Ito, for providing me with the opportunity to work in the field of synthetic aperture radar processing: Dr. Cumming for his knowledge of SAR and for providing access to expertise and data at MacDonald Dettwiler; and Dr. Ito for academic guidance and for his help in reviewing my work and my presentations. I would also like to thank Dr. Frank Wong of MacDonald Dettwiler for technical advice and many useful discussions.

For financial support I am grateful to the University of British Columbia, the Natural Science and Engineering Research Council of Canada, and the B. C. Science Council.

Finally, I would like to say thanks to fellow graduate students for their support over the years, and especially to those of the Radar Remote Sensing Group for a relaxed, fun, yet interesting and productive working environment.

## Chapter 1

### Introduction

#### 1.1 Background

##### 1.1.1 SAR in Remote Sensing

Synthetic aperture radar (SAR) is a technique for creating high resolution images of the earth's surface. The data for a SAR image are collected by an aircraft or satellite with a side-looking antenna, which transmits a stream of radar pulses and records the backscattered signal corresponding to each pulse. The received echoes are arranged in a rectangular format, with one dimension being the pulse transmission time (along the flight track) and the other being the delay time within an echo (cross track). This two-dimensional data set is then processed to form an image. Since the moving antenna beam covers a strip of the earth's surface, this type of SAR imaging is referred to as strip-map SAR.

A SAR image represents the backscatter of microwave energy over the area of the surface being observed, and this in turn depends on properties of the surface such as slope, roughness, inhomogeneities, and dielectric constant [1]. These dependencies allow SAR imagery to be used in conjunction with models of the scattering mechanism to measure various characteristics of the earth's surface. Also, an important aspect of SAR is that it is an active microwave sensor. That is, it transmits its own energy in order to receive the backscatter, as opposed to passive sensors which receive either the earth's radiation or the reflected illumination from the sun. Another advantage is the ability of microwaves to penetrate cloud cover. Overall, the ability to form images day or night and in a variety of weather conditions makes SAR a valuable remote sensing tool.

There are many applications of SAR imagery in the physical sciences. In oceanography, for

example, images are analyzed to determine the direction and wavelength of ocean waves. Also, in polar regions, SAR imagery can be used to distinguish between first-year ice and multi-year ice, which is important for navigation. Geological applications include the classification of rock type based on surface roughness, and the determination of large scale structural features. In vegetated areas, the scattering mechanism depends on plant type and density, so that SAR imagery can be applied to crop classification and the monitoring of deforestation. For an overview of applications and for references, see [1] and [2].

The first spaceborne SAR was launched on the Seasat satellite by NASA in 1978. This was followed by the shuttle imaging radar missions, SIR-A, SIR-B and SIR-C, in 1981, 1984 and 1994 respectively [3]. These missions demonstrated the usefulness of SAR as a remote sensing tool, and inspired much interest in SAR around the world. There are currently two satellites in orbit with SAR capability: the European Space Agency's Earth Resources Satellite (E-ERS-1) launched in 1991 [4], and Japan's J-ERS-1 launched in 1992 [5]. Also, the Canadian Space Agency is expected to launch its Radarsat satellite in 1995 [6]. Finally, in addition to spaceborne platforms for SAR, airborne SAR's are commonly flown in several countries.

Current SAR systems are being designed to obtain images at multiple wavelengths, polarizations, and incidence angles [7]. This allows more information to be extracted from SAR imagery because the scattering mechanisms are sensitive to these parameters. Another recent development is the emergence of applications of SAR imagery which make use of the phase of the image pixels. For example, the phase difference between images obtained using different polarizations can be related to scene properties [8]. Also, in interferometric SAR, the phase difference between images obtained at slightly different viewing angles can be related to terrain height [9]. As the applications of SAR imagery become more sophisticated, the accuracy and calibration of the images become more important. Thus, it is important that the processing of the SAR data is done accurately throughout the image.

### 1.1.2 SAR Processing

In the scene being imaged, the dimension along the flight path is referred to as azimuth, and the dimension perpendicular to the flight path is referred to as range. Resolution in the range direction is achieved by transmitting a large bandwidth pulse. To improve signal to noise ratio, a long phase-encoded pulse such as a linear FM chirp is transmitted, and the received signal is compressed in the range dimension by means of a matched filter [10, 11]. Without further processing, the azimuth resolution would be limited to the beamwidth of the antenna. To see how azimuth resolution can be improved, consider the signal received from a single point scatterer. The moving platform is in a different position at each time a pulse is transmitted and received. (Since the speed of light is much greater than the platform velocity, it is assumed that transmission and reception of a pulse take place at the same azimuth position.) If the received signal is coherently demodulated, then the phase of the received echoes will vary with respect to azimuth position in a predictable manner. To compress the data in the azimuth direction, this phase variation can be matched, and the received echoes can be processed like elements in a phased array [12, 13]. The length of this synthesized array — called the aperture — is determined by the amount of time the scatterer is covered by the antenna beam.

Processing is complicated by the fact that the distance to the point scatterer can vary over the aperture by more than the range resolution. This is called range cell migration. Thus, in order to form the synthesized array for a point scatterer, the data values along the range migration curve need to be interpolated. Performing this operation for every point in the image amounts to a two-dimensional correlation of the data with the signal that would be received from a point scatterer — the point scatterer response. Also, because the point scatterer response depends on the scatterer's location in the range direction, this correlation must be range-variant. The aperture for a spaceborne SAR can be several thousands of samples long, so that a direct time-domain implementation of this correlation is very computationally expensive. The objective of SAR processing algorithms is to make suitable approximations to the exact correlation, so that images can be formed efficiently, but without noticeable degradation in

image quality.

In conventional SAR, the antenna is pointed perpendicular, or broadside, to the flight path. In this case the range migration is small enough for the point scatterer response to be nearly in line with the azimuth direction in the signal data. As a result, approximations to the exact correlation can be made which allow processing to be done in the azimuth-frequency and range-time domain [14], [15]. This domain is a natural one for SAR, since the instantaneous azimuth-frequency (or Doppler frequency) of the signal varies with the scatterer's position within the antenna beam. In this sense, SAR processing can be thought of as using the range-time delay and the Doppler history of a scatterer in order to locate its position in the image. The ability to operate in the azimuth-frequency domain greatly simplifies processing, because of the availability of computationally efficient Fast Fourier Transform (FFT) techniques. Also, the range-time domain allows for range-variant implementation of azimuth compression and range cell migration correction.

In most SAR processing algorithms, however, the range-dependent interpolation required in range cell migration correction is difficult to implement, and truncation of the interpolation kernel causes a loss of range resolution and introduces artifacts into the image [16]. Recently, an algorithm has been proposed which avoids this problem [17], [18], [19]. This algorithm, called chirp scaling, makes use of the linear FM property of the transmitted pulses in order to scale the range time axis at each azimuth frequency. This is done to remove the range-dependence of range cell migration correction, so that the bulk of the correction can then be performed in the two-dimensional frequency domain. Thus, the chirp scaling algorithm provides more accurate processing while requiring only multiplication and FFT operations.

### 1.1.3 Squint Mode SAR

The squint angle is the angle by which the antenna is pointed forward or backward from the broadside position. In conventional SAR, the squint angle due to antenna pointing errors or earth rotation is less than four degrees. In squint mode SAR, however, the antenna is

deliberately pointed forward or backward by as much as several tens of degrees. Squint mode has previously been used in airborne platforms in conjunction with a type of SAR imaging called spotlight SAR, in which the antenna is continuously steered to point at a fixed, small area on the ground. Algorithms for processing spotlight SAR data, based on polar formatting, can be used for high squint [20, 21, 22]. However, their application to strip map SAR data, in which the squint angle is held fixed while collecting data from a large area, is difficult and inefficient [23].

While strip-mapping squint mode is not currently used in spaceborne remote sensing SARs, it has the potential to allow more information to be extracted from SAR imagery. Multiple look angles in the azimuth direction enables the measurement of the azimuthal angle dependence of backscatter, which would provide information about surface structure. Also, the ability to form images from different viewing angles would aid in the interpretation of SAR imagery of complex terrain [3]. Another possible application of squint is in beam coverage. By utilizing the squint and elevation angles of the antenna, areas of the earth's surface could be imaged within a single satellite pass that could not be covered with a conventional SAR geometry. However, before squint mode SAR can become practical in a remote sensing context, the efficient processing of strip-map SAR data acquired with a large squint angle needs to be better understood. For remote sensing SARs, the approximations used in conventional SAR processing algorithms become invalid as the squint angle increases, leading to a degradation in image quality. This effect becomes more noticeable at even moderate squint angles when the application of the imagery places very demanding requirements on the accuracy of the processor. Thus, by investigating the processing of squint mode SAR data, improvements can be made in processing accuracy and efficiency that will benefit strip-map SAR processing in general. Also, the investigation of SAR imaging in the context of squint mode allows for a more general understanding of the properties of the SAR signal.

Processing problems arise from the fact that with a large squint angle, the range migration becomes very large, so that the point scatterer response follows an oblique trajectory in the

two-dimensional data set. This causes higher order range-azimuth coupling terms to become significant in the phase of the two-dimensional Fourier transform of the point scatterer response. Thus the approximations that are used by conventional SAR processing algorithms lead to significant degradations in the image. For moderate squint angles, processing can be improved by performing some steps in the two-dimensional frequency domain [17], [24]. However, this neglects the range-dependence of the coupling terms, which can cause significant degradation in the image at higher values of squint. Among the algorithms that perform some steps in the two-dimensional frequency domain, the chirp scaling algorithm makes use of a novel technique to remove the range dependence of range cell migration correction. This algorithm has the potential to process high squint SAR data, especially if the chirp scaling technique can be extended to accommodate other range-dependencies in SAR processing. Such extensions include the use of different types of transmitted pulses or filtering steps during processing that may affect chirp scaling. The properties and limitations of this relatively new algorithm need to be fully understood.

## 1.2 Thesis Objectives

The problem addressed in this thesis is the accurate processing of strip-map SAR data, acquired in squint mode from a spaceborne platform. In addition, the chirp scaling technique is investigated to determine how it can be used to solve problems in processing high squint data.

The objectives of this thesis can be summarized as follows:

- Review the theory of SAR imaging and SAR processing algorithms, and describe the chirp scaling algorithm.
- Investigate the effects of a squint mode imaging geometry on the SAR signal properties and the processing of SAR data.
- Investigate the chirp scaling algorithm for conventional and high squint SAR. Implement the chirp scaling algorithm on Seasat data.

- Extend the chirp scaling algorithm to improve the accuracy of range cell migration correction for more general imaging geometries.
- Present a new algorithm, based on the chirp scaling of nonlinear FM pulses, for accurately processing squint mode SAR data. Implement the algorithm on simulated high squint data.

## Chapter 2

### Theory of SAR Imaging

#### 2.1 Introduction

The purpose of this chapter is to introduce notation and to provide a theoretical basis for understanding strip-map SAR image formation. The following points are covered: First, the general SAR imaging geometry is described, and the basic assumptions that are used to model the SAR signal are presented. Some of these assumptions will be re-examined for the case of high squint in a later chapter. Next, the topic of pulse compression is reviewed, as this provides some of the concepts that are used in SAR processing. Then, a description is given of the SAR exact correlation and the resulting point spread function. Finally, the technique of image resampling to ground coordinates is briefly described.

#### 2.2 SAR Signal Model

##### 2.2.1 Point Scatterer Response

To describe the collection and processing of SAR data, it is convenient to consider the case of a single point scatterer. This is sufficient to model the signal and the processing operations, since the data which is used to form an image is the superposition of signals from a distribution of point scatterers. To introduce the notation for describing the signal, consider the general SAR imaging geometry shown in Figure 2.1, in which a platform travels over the earth's surface at an altitude  $h$ , and with a velocity  $v$ . The side-looking antenna is pointed at an angle  $\gamma_e$  from nadir, called the elevation angle. The beamwidth in elevation determines the width of the strip on the surface being imaged, called the swath. The squint angle of the antenna,  $\theta$ , is the angle

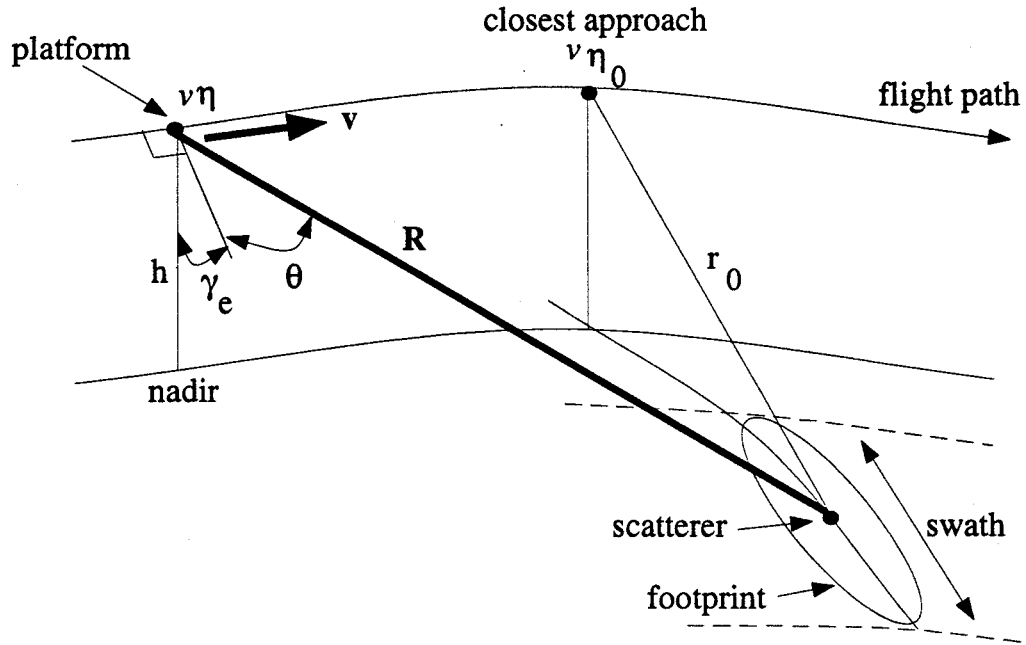


Figure 2.1: General SAR imaging geometry.

from broadside to the direction of the beam center, and the beamwidth in azimuth determines the exposure time of a scatterer during which the synthetic aperture can be formed. Let  $\eta$  denote the azimuth-time variable, also called slow time, so that the position of the platform along the flight path is given by  $v\eta$ , as shown in the figure. The azimuth position of a single point scatterer is given by the azimuth-time at which the platform is closest to the scatterer,  $\eta_0$ . In SAR data, the cross-track direction is measured from flight path to the scatterer – sometimes called slant range – rather than the along the surface. The scatterer location in this dimension is indicated by its closest approach range,  $r_0$ , as shown in the figure. Letting  $c$  denote the speed of light, the closest approach range-time of a scatterer is represented by  $t_0 = 2r_0/c$ . Thus, the scatterer distribution that is being imaged has coordinates of  $(\eta_0, t_0)$ .

For satellite SARs such as Seasat and ERS-1, the swath width on the surface is about  $100\text{ km}$ , giving a change in closest approach range across the swath – or range swath – of about  $40\text{ km}$ . The width of the footprint on the surface for a given platform depends on the

wavelength. For an L-band spaceborne SAR such as Seasat the aperture is about 20 km, and for the ERS-1 C-band SAR it is about 5 km.

To collect the data for a SAR image, pulses are transmitted periodically at a rate called the pulse repetition frequency (*PRF*) as the platform moves in the azimuth direction. The instantaneous range or distance from the platform to the scatterer changes with each pulse, and for a scatterer at closest approach range  $r_0$ , let this instantaneous distance be indicated by  $R(\eta - \eta_0; r_0)$ . Also,  $R(\eta - \eta_0; r_0)$  and the flight path are assumed to describe the platform motion relative to the scatterer, including the effect of scatterer motion due to earth rotation. The effect of earth rotation on the signal will be described briefly in a later section. An expression for  $R(\eta - \eta_0; r_0)$  depends on the particular geometry of the platform motion. The simplest geometry consists of a platform travelling in a straight line. This is referred to as a rectilinear geometry, and is sufficient to describe the signal in an airborne SAR after motion compensation. The distance equation in this case is given by:

$$R(\eta - \eta_0; r_0) = \sqrt{r_0^2 + v^2(\eta - \eta_0)^2}. \quad (2.1)$$

A transmitted pulse can be expressed as

$$s_{tx}(\tau) = \text{Re}[p(\tau) \exp(j2\pi f_0 \tau)], \quad (2.2)$$

where  $\tau$  is the pulse travel-time or fast-time variable,  $f_0$  is the carrier frequency, and  $p(\tau)$  is the complex baseband representation of the pulse. For example, a linear FM pulse with a rectangular amplitude of duration  $T$  is given by

$$p(\tau) = \text{rect}\left(\frac{\tau}{T}\right) \exp(-j\pi K \tau^2), \quad (2.3)$$

where  $K$  is the frequency rate. Since the speed of light,  $c$ , is much greater than the platform velocity, it can be assumed that the platform is stationary during the transmission and reception of a pulse. This is the 'stop-start' assumption, and has a negligible effect for moderate squint angles [16]. Pulses received from a point scatterer are thus delayed by the round trip travel time,  $2R(\eta - \eta_0; r_0)/c$ . This delay arises in both the complex baseband pulse and in the phase

of the carrier. If the received signal is coherently demodulated, then the phase of the carrier as it varies from pulse to pulse can be retained. The received SAR signal from a point scatterer at  $(\eta_0, t_0)$  in complex baseband form is represented as

$$d(\eta, \tau) = \sigma' w(\eta - \eta_0 - \eta_c) p\left[\tau - \frac{2R(\eta - \eta_0; r_0)}{c}\right] \exp\left[\frac{-j4\pi f_0 R(\eta - \eta_0; r_0)}{c}\right]. \quad (2.4)$$

In this expression,  $\sigma'$  is the scatterer reflectivity, including range attenuation and the antenna pattern in elevation. The function  $w(\eta)$  is the antenna pattern in azimuth, which weights the pulses received from the scatterer as it passes through the footprint, and thus determines the exposure time. Assume that the antenna beamwidth in the azimuth direction is  $\frac{\lambda}{L}$ , where  $\lambda = \frac{c}{f_0}$  is the wavelength and  $L$  is the antenna length in azimuth. For a rectilinear geometry, the exposure time for small squint angles is

$$\Delta\eta = \frac{\lambda r_0}{Lv}. \quad (2.5)$$

The parameter  $\eta_c$  in the antenna weighting represents the effect of the squint angle. At zero squint, the scatterer is in the center of the beam when the platform is in the closest approach position. Thus, in this case  $\eta_c$  is zero and the received SAR signal is weighted in the azimuth direction by  $w(\eta - \eta_0)$ . When the antenna is squinted by the angle  $\theta$ , the time at which the scatterer is in the center of the beam is offset from the closest approach time by  $\eta_c$ . In this case, the signal is weighted in azimuth by  $w(\eta - \eta_0 - \eta_c)$ . For example, for a rectilinear geometry, the beam center offset time is

$$\eta_c = -\frac{r_0 \tan(\theta)}{v}. \quad (2.6)$$

Note that for forward squint, the squint angle is positive and the beam center offset time,  $\eta_c$ , is negative.

The azimuth phase in Equation (2.4) is proportional to the distance to the scatterer,  $R(\eta - \eta_0; r_0)$ , which can be broken into an azimuth-varying term, and a constant term equal to the closest approach range:

$$R_{\Delta}(\eta - \eta_0; r_0) = R(\eta - \eta_0; r_0) - r_0. \quad (2.7)$$

It is the azimuth-varying term that allows SAR data to be compressed in the azimuth direction, while the constant term can be incorporated into the scatterer reflectivity:

$$\sigma = \sigma' \exp\left(\frac{-j4\pi f_0 r_0}{c}\right). \quad (2.8)$$

This phase component of the complex image is used in SAR applications such as interferometry.

Using the above definitions, the SAR data received from a point scatterer at range  $r_0$  can be represented by

$$d(\eta, \tau) = \sigma s(\eta - \eta_0, \tau - t_0; r_0), \quad (2.9)$$

where  $s(\eta, \tau; r_0)$  is the point scatterer response defined with respect to the closest approach azimuth-time and closest approach range-time, given by [15]

$$s(\eta, \tau; r_0) = w(\eta - \eta_c) p\left[\tau - \frac{2R_\Delta(\eta; r_0)}{c}\right] \exp\left[\frac{-j4\pi f_0 R_\Delta(\eta; r_0)}{c}\right]. \quad (2.10)$$

The point scatterer response is a function of the temporal variables,  $\eta$  and  $\tau$ , and is also dependent on the scatterer's range,  $r_0$ . In practice, there may also be a slight dependence on azimuth position. In spaceborne SAR, this is due to changes in the platform velocity and altitude between different positions within the orbit. However, the effect of this variation on forming an image is small, and will not be considered in the signal model. The point scatterer response represents the dispersion of information from a point scatterer in the signal data, and its form is illustrated in Figure 2.2. This figure shows the region of support of the received signal, which is centered in azimuth-time at  $(\eta_0 + \eta_c)$  and has an azimuth-time duration of  $\Delta\eta$ . In range-time, the signal is delayed by the round trip travel time as shown by the range migration curve, and has a duration equal to the pulse length,  $T$ . Increasing the squint angle increases the magnitude of the beam center offset time,  $\eta_c$ , thus increasing the slope of the range migration curve within the exposure time of the scatterer. In addition, since the azimuth phase also depends on  $R(\eta - \eta_0; r_0)$ , increasing the squint angle results in an increase in the linear component of this phase. This causes the SAR signal energy to be shifted in azimuth-frequency to a value called the Doppler centroid.

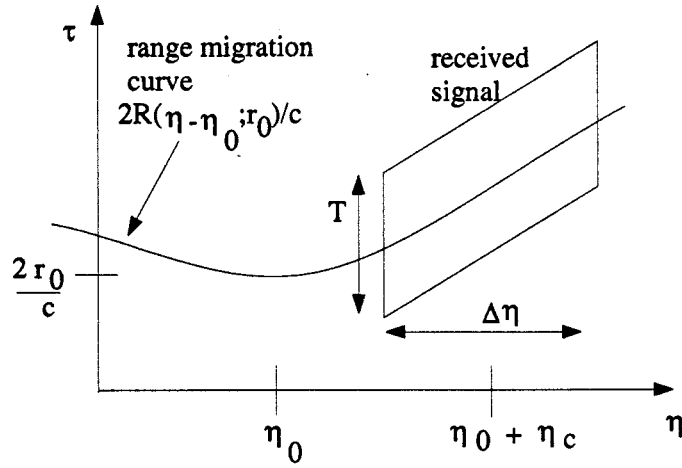


Figure 2.2: Point scatterer response.

The frequency content of the SAR signal in the range direction depends on the transmitted pulse,  $p(\tau)$ . In the azimuth direction, the instantaneous azimuth-frequency of the SAR signal as the scatterer passes through the antenna beam can be found as follows: Express the platform to scatterer distance as the magnitude of a vector,  $\mathbf{R}(\eta - \eta_0; r_0)$ . Then, taking the derivative of the azimuth phase in Equation (2.10) to find the instantaneous azimuth-frequency, gives [25]

$$f_\eta = \frac{-2f_0 \mathbf{v} \cdot \mathbf{R}(\eta - \eta_0; r_0)}{cR(\eta - \eta_0; r_0)}, \quad (2.11)$$

where  $\mathbf{v}$  is the velocity vector of the platform and  $\cdot$  represents dot product. The vectors  $\mathbf{v}$  and  $\mathbf{R}$  define a plane in which the angle to the scatterer with respect to broadside is defined. This angle changes as the scatterer passes through the beam, and will be referred to as the instantaneous squint angle,  $\theta_s(\eta - \eta_0)$ . At the beam center, this is equal to the nominal squint angle,  $\theta$ . Since the broadside direction is perpendicular to the velocity vector, the instantaneous azimuth-frequency in Equation (2.11) can be written as

$$f_\eta = \frac{2v f_0 \sin(\theta_s(\eta - \eta_0))}{c}. \quad (2.12)$$

Thus, the signal energy is centered in azimuth-frequency at the Doppler centroid,  $f_{\eta c}$ , given by

$$f_{\eta c} = \frac{2v f_0 \sin(\theta)}{c}. \quad (2.13)$$

The azimuth bandwidth is the difference between the azimuth-frequencies at the edges of the beam. Assuming a beamwidth of  $\lambda/L$ , this can be expressed as

$$\Delta f_{\eta} = \frac{2v}{\lambda} \left( \sin\left(\theta + \frac{\lambda}{2L}\right) - \sin\left(\theta - \frac{\lambda}{2L}\right) \right), \quad (2.14)$$

which for small squint angles is approximately

$$\Delta f_{\eta} = \frac{2v}{L}. \quad (2.15)$$

In practice, the Doppler centroid is estimated from the SAR data, since the antenna pointing accuracy is not sufficient to calculate it directly from the squint angle [26, 27]. In addition, the SAR signal is sampled in the azimuth direction by the pulse repetition frequency (PRF). This sampling rate is chosen to exceed the azimuth bandwidth, but can be many times less than the Doppler centroid. This causes the signal energy to be wrapped around in azimuth-frequency, resulting in an ambiguity in azimuth-frequency equal to an integer multiple of the PRF. However, the SAR transfer function depends on the actual, non-aliased value of azimuth-frequency, so that techniques for resolving the Doppler centroid ambiguity have been developed [28, 29, 30]. Finally, it should be noted that the Doppler centroid of the signal also depends on the closest approach range to the scatterer, and this will be discussed in detail in a later chapter.

### 2.2.2 Orbital Geometry

In spaceborne SAR, the orbital geometry of the platform motion, the earth's curvature, and the earth rotation must be taken into account. This affects the azimuth-time varying distance from the platform to a scatterer,  $R(\eta; r_0)$ . In general, an equation for this distance as a function of azimuth-time and closest approach range can be obtained from information about the satellite's orbit and the earth's geometry [16]. In addition, coefficients of  $R(\eta; r_0)$  can be refined by autofocus techniques [26].

In modelling the SAR signal for processing purposes, it is useful to have a simple form for  $R(\eta; r_0)$  to allow derivation of processing algorithms. The equation that is used to represent  $R(\eta; r_0)$  must be accurate enough to model the azimuth-varying phase and the range migration in the point scatterer response, so that these effects can be accurately matched during SAR processing. A good approximation for small to moderate squint angles can be obtained by fitting a hyperbolic equation to  $R(\eta; r_0)$  at  $\eta = 0$ , corresponding to the closest approach azimuth-time, as follows:

$$R(\eta; r_0) \approx \sqrt{r_0^2 + B(r_0)\eta^2}, \quad (2.16)$$

where  $B(r_0)$  is a range dependent coefficient. Note that this equation represents a rectilinear geometry when  $B$  is equal to the constant  $v^2$ . On the other hand, in an orbital geometry the parameter  $B(r_0)$  can be interpreted as the square of a range-dependent ‘effective velocity’ in modelling the point scatterer response [25, 31, 32, 33].

To illustrate the effects of an orbital geometry on the SAR signal properties, consider the simple example of a circular orbit and a spherical, nonrotating earth, where  $r_e$  is the earth’s radius and  $H = (r_e + h)$  is the radius of the orbit. Circular or near circular orbits are useful for remote sensing since they provide a nearly constant distance from the earth’s surface [34]. The platform orbits the earth in an orbital plane, which can be thought of as rotating about the earth’s center with an angular velocity of  $v/H$ . Denote the angle between the orbital plane and the scatterer, measured at the closest approach position, by  $\alpha_r$ . This is related to the closest approach range of the scatterer by:

$$\alpha_r(r_0) = \arccos\left[\frac{r_e^2 + H^2 - r_0^2}{2r_e H}\right]. \quad (2.17)$$

Since the antenna footprint can be thought of as rotating with the orbital plane, the fact that the footprint is closer to the earth’s center means that it has a lower velocity than that of the platform. This leads to the concept of the ground velocity of the antenna footprint,  $v_g(r_0)$ , which varies with the range from the platform:

$$v_g(r_0) = \frac{vr_e \cos[\alpha_r(r_0)]}{H}. \quad (2.18)$$

This affects the exposure time of a scatterer, since the footprint passes over the the scatterer with the ground velocity instead of the platform velocity [25]:

$$\Delta\eta = \frac{\lambda r_0}{Lv_g}. \quad (2.19)$$

Finally, the distance from the platform to the scatterer can be shown to be:

$$R(\eta - \eta_0; r_0) = \sqrt{r_e^2 + H^2 - (r_e^2 + H^2 - r_0^2) \cos\left(\frac{v(\eta - \eta_0)}{H}\right)}. \quad (2.20)$$

This expression can be used to find a hyperbolic representation of  $R(\eta; r_0)$ , where the parameter  $B(r_0)$  in this case is given by

$$B(r_0) = vv_g(r_0). \quad (2.21)$$

Another aspect of spaceborne SAR is the earth's rotation. In this case, the motion of the platform with respect to the scatterer is determined by subtracting the scatterer's velocity vector due to earth rotation from the velocity vector of the platform. Since the direction of the resultant can be different from the original direction of the platform, an antenna that was pointed at right angles to the original direction may no longer be perpendicular to the resultant velocity. Thus, the net effect of earth rotation is the introduction of a squint angle [25]. This effect is greatest at the equator in the case of a polar orbit, where the squint angle is about four degrees for a satellite altitude of about 800 km.

### 2.2.3 SAR Constraints

SAR imaging is subject to a fundamental constraint involving the azimuth resolution and the swath width. The received echo from the scatterer distribution within the swath must be short enough to fit between two consecutive transmitted pulses. Thus, for a given swath, this places an upper bound on the *PRF*. However, the *PRF* must also be large enough to sample the azimuth signal. Since the swath width depends on the antenna width in elevation, and the azimuth bandwidth depends on the antenna length in azimuth, these constraints can be combined to establish a minimum area for the antenna [12, 35, 13].

### 2.3 Pulse Compression

The objective of SAR processing is the compression of the point scatterer response into a narrow point spread function in order to obtain a high resolution image. Pulse compression refers to the technique of compressing a long, phase-encoded signal by means of a matched filter. This operation is performed on SAR data in the range and azimuth directions. In range, a transmitted pulse such as a linear FM signal is used to introduce the phase-encoding. This provides a large range bandwidth which is needed to achieve high resolution, but with the energy spread over a longer duration pulse so as to not exceed the peak power limitations of the transmitter. This causes the time-bandwidth product of the pulse, which is equal to the ratio of the lengths of the pulse before and after compression, to be significantly greater than unity [10, 11]. Similarly in azimuth, the phase-encoding results from the the azimuth-varying distance to the scatterer as discussed above, although azimuth compression must be performed after range cell migration correction.

#### 2.3.1 Matched Filter

To review the concepts of pulse compression, the operation of compressing a single received pulse in the range-time dimension will be briefly described. Since pulse compression is a linear filtering operation, it can be described in the frequency domain. Let the complex baseband representation of the transmitted pulse be

$$p(\tau) = m(\tau) \exp(j\phi_p(\tau)), \quad (2.22)$$

where  $m(\tau)$  is a slowly varying amplitude of duration  $T$ , and  $\phi_p(\tau)$  is the phase modulation. The Fourier transform is

$$P(f_\tau) = \int m(\tau) \exp(j(\phi_p(\tau) - 2\pi f_\tau \tau)) d\tau, \quad (2.23)$$

where  $f_\tau$  is the frequency variable corresponding to the range-time variable  $\tau$ . For large enough time-bandwidth product signals, an accurate approximation to this integral can be found by

using the method of stationary phase [10, 36]. Heuristically, the method of stationary phase takes advantage of the fact that the main contribution to the integral occurs at a point, called the stationary point,  $\tau_*$ , at which the derivative of the phase of the integrand is zero. At other points, the integrand is oscillating rapidly so that adjacent cycles cancel, and the contribution to the integral is negligible. In the above integral for the Fourier transform of  $p(\tau)$ , the stationary point is found by solving the equation

$$\frac{1}{2\pi} \frac{d\phi_p(\tau)}{d\tau} = f_\tau \quad (2.24)$$

to give an expression for  $\tau_*$  in terms of  $f_\tau$ . Note that given a frequency,  $f_\tau$ , the stationary point is that time in the signal at which the instantaneous frequency is equal to  $f_\tau$ . Thus, Equation (2.24) indicates a relationship between time and instantaneous frequency in large time-bandwidth product signals.

Given the stationary point, the Fourier transform of  $p(\tau)$  can be written as

$$P(f_\tau) = G_p M(f_\tau) \exp(j\Phi_p(f_\tau)), \quad (2.25)$$

where the factor  $G_p$  is approximately a constant, and is given by

$$G_p = \sqrt{\frac{2\pi}{|\phi_p''(\tau_*)|}} \exp\left(\frac{j\pi \operatorname{sgn}(\phi_p''(\tau_*))}{4}\right). \quad (2.26)$$

The function

$$M(f_\tau) = m(\tau_*) \quad (2.27)$$

is the amplitude spectrum which determines the range bandwidth, and

$$\Phi_p(f_\tau) = \phi_p(\tau_*) - 2\pi f_\tau \tau_* \quad (2.28)$$

is the phase of the spectrum. As an example, consider the linear FM pulse with rectangular amplitude shown earlier:

$$p(\tau) = \operatorname{rect}\left(\frac{\tau}{T}\right) \exp(-j\pi K\tau^2). \quad (2.29)$$

The stationary point is

$$\tau_* = -f_\tau/K, \quad (2.30)$$

which reflects the linear relationship between time and instantaneous frequency in a linear FM signal. The Fourier transform is approximately

$$P(f_\tau) = \frac{\exp(-j\pi/4)}{\sqrt{|K|}} \text{rect}\left(\frac{-f_\tau}{KT}\right) \exp\left(\frac{j\pi f_\tau^2}{K}\right) \quad (2.31)$$

and the bandwidth is  $KT$ .

Consider matched filtering of a linear FM transmitted pulse, which can be expressed in the frequency domain as

$$H_r(f_\tau) = P(f_\tau)P^*(f_\tau) \quad (2.32)$$

$$= \text{rect}\left(\frac{-f_\tau}{KT}\right), \quad (2.33)$$

where  $H_r(f_\tau)$  is the Fourier transform of the compressed pulse. Thus, after inverse Fourier transformation the compressed pulse is

$$h_r(\tau) = \text{sinc}(KT\tau), \quad (2.34)$$

which has a resolution width approximately equal to the inverse of the bandwidth. Pulse compression removes the quadratic and higher order phase variation of the spectrum of the received signal, leaving an amplitude spectrum that, when inverse Fourier transformed, gives the narrow compressed pulse. An important characteristic of the compressed pulse is the tradeoff between the resolution width and the sidelobe level, which is determined by the shape of the amplitude spectrum. A rectangular spectrum results in a *sinc*-shaped compressed pulse, which has relatively high sidelobes. To control the shape of the amplitude spectrum during pulse compression, the Fourier transform of the received signal can be multiplied by a weighting function such as a Kaiser or Hanning window. In this case the matched filter can be thought of as matching the phase of the pulse spectrum and weighting the amplitude. The Fourier transform of the compressed pulse is then expressed as

$$H_r(f_\tau) = P(f_\tau)W_r(f_\tau) \exp(-j\Phi_p(f_\tau)), \quad (2.35)$$

where  $W_r(f_\tau)$  is the weighting function.

$\phi_{err}$ (degrees)	peak phase error (degrees)
0	0
45	15
90	29
135	43

Table 2.1: Peak phase error in compressed pulse due to compression error.

### 2.3.2 Compression Error

Finally, the effect of a parameter error in the matched filter should be noted. In order to achieve the best possible resolution after pulse compression, the phase of the pulse spectrum must be matched accurately. For a linear FM pulse, this requires an accurate representation of the frequency rate,  $K$ . If the frequency rate of the matched filter differs from the correct value by an amount  $\Delta K$ , then the spectrum of the compressed pulse is approximately

$$H_r(f_\tau) = \text{rect}\left(\frac{-f_\tau}{KT}\right) \exp\left(\frac{j\pi\Delta K f_\tau^2}{K^2}\right), \quad (2.36)$$

assuming  $\Delta K \ll K$ . The residual phase due to  $\Delta K$  causes a broadening of the compressed pulse and an increase in sidelobe level. The compression error can be characterized by the maximum phase error at the edge of the frequency band, where  $f_\tau = \frac{KT}{2}$ :

$$\phi_{err} = \frac{\pi\Delta KT^2}{4}. \quad (2.37)$$

Figure 2.3 shows the amplitude of the compressed pulse and the per cent increase in 3dB resolution width for several values of  $\phi_{err}$ . Note that a broadening is accompanied by a decrease in the peak amplitude of the compressed pulse. Another effect of a compression error is the introduction of a phase error in the compressed pulse. Table 2.1 shows the phase error at the peak of the compressed pulse for several values of  $\phi_{err}$ .

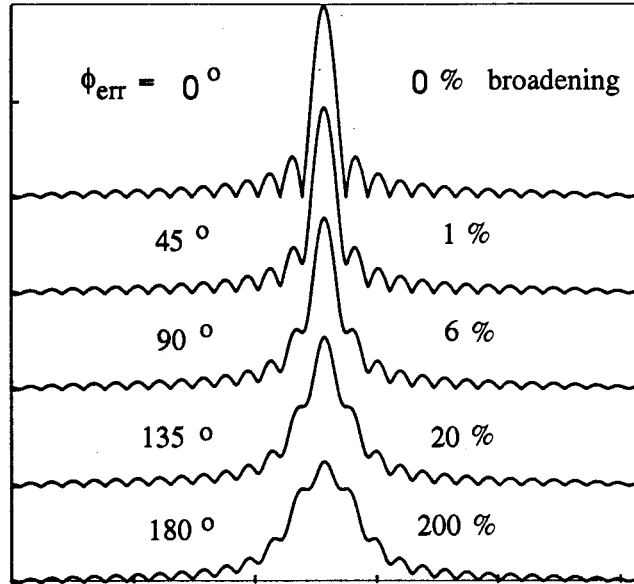


Figure 2.3: Effect of a quadratic phase error in pulse compression.

## 2.4 Exact SAR Correlation

### 2.4.1 Time Domain Correlation

Given the received data from a distribution of scatterers, SAR image formation consists of compressing the signal from each scatterer into a narrow point spread function by means of a correlation of the data with the range-dependent point scatterer response. To express this operation, it is first convenient to represent the SAR data as a convolution of the distribution of scatterer reflectivity,  $\sigma(\eta_0, t_0)$ , with the point scatterer response:

$$d(\eta, \tau) = \iint \sigma(\eta_0, t_0) s(\eta - \eta_0, \tau - t_0; r_0) d\eta_0 dt_0. \quad (2.38)$$

The time domain correlation of the data with the point scatterer response is written as

$$\hat{\sigma}(\eta_i, t_i) = \iint d(\eta, \tau) s^*(\eta - \eta_i, \tau - t_i; r) d\eta d\tau, \quad (2.39)$$

where  $\hat{\sigma}(\eta_i, t_i)$  is the processed image which is an estimate of the reflectivity in the scene. The image dimensions,  $\eta_i$  and  $t_i$ , correspond to the closest approach azimuth-time and closest

approach range-time of points in the image, with  $\tau$  denoting the closest approach range corresponding to an image point at  $t_i$ . The correlation in Equation (2.39) is the most direct method of image formation from SAR data. However, because of the large number of samples of the point scatterer response, a time domain correlation is very computationally expensive, and in general is not used in practice.

The relationship between the image and the scene can be found by substituting for  $d(\eta, \tau)$  in Equation (2.39), giving

$$\hat{\sigma}(\eta_i, t_i) = \iint \sigma(\eta_0, t_0) h(\eta_i - \eta_0, t_i - t_0; r, r_0) d\eta_0 dt_0, \quad (2.40)$$

where

$$h(\eta_i - \eta_0, t_i - t_0; r, r_0) = \iint s(\eta - \eta_0, \tau - t_0; r_0) s^*(\eta - \eta_i, \tau - t_i; r) d\eta d\tau. \quad (2.41)$$

Thus, the processed image is related to the scene by a convolution with the point spread function,  $h(\eta_i, t_i; r)$ , which determines the quality of the processed image in terms of resolution, sidelobe level, phase, and registration.

#### 2.4.2 Frequency Domain Correlation

Next, some insight into the SAR correlation can be gained by considering the data in the two-dimensional frequency domain. Also, SAR processing algorithms make use of the frequency domain in one or both dimensions in order to improve processing efficiency. Let  $D(f_\eta, f_\tau)$  be the Fourier transform of the SAR data,  $d(\eta, \tau)$ , where  $f_\eta$  is the frequency variable corresponding to azimuth-time,  $\eta$ , and  $f_\tau$  is the frequency variable corresponding to range-time,  $\tau$ . Taking the two-dimensional Fourier transform of Equation (2.38) gives

$$D(f_\eta, f_\tau) = \iint \sigma(\eta_0, t_0) S_2(f_\eta, f_\tau; r_0) \exp(-j2\pi f_\eta \eta_0) \exp(-j2\pi f_\tau t_0) d\eta_0 dt_0, \quad (2.42)$$

where  $S_2(f_\eta, f_\tau; r_0)$  is the Fourier transform of the point scatterer response,  $s(\eta, \tau; r_0)$ . The function  $S_2(f_\eta, f_\tau; r_0)$  is sometimes called the SAR transfer function for a scatterer at  $r_0$ .

The SAR transfer function can be evaluated by first Fourier transforming  $s(\eta, \tau; r_0)$  with respect to  $\tau$ , as shown in Equations (2.25) to (2.28). Then, the result can be Fourier transformed with respect to  $\eta$ , where again the method of stationary phase can be used because the azimuth-varying phase in the point scatterer response results in a large time-bandwidth product in the azimuth direction [37, 38]. In this way, the SAR transfer function can be shown to have the form

$$S_2(f_\eta, f_\tau; r_0) = G A(f_\eta, f_\tau) \exp[j\Phi_p(f_\tau) + j\Phi(f_\eta, f_\tau; r_0)]. \quad (2.43)$$

The factor  $G$  in this expression, given by

$$G = G_p \exp(-j\pi/4) \sqrt{\frac{cr_0}{2B(f_0 + f_\tau)} \left(1 - \frac{c^2 f_\eta^2}{4(f_0 + f_\tau)^2 B}\right)^{-3/2}}, \quad (2.44)$$

is a very slow function of frequency compared to the amplitude spectrum and can be treated as a constant. The amplitude of the SAR transfer function is given by

$$A(f_\eta, f_\tau) = M(f_\tau)W(f_\eta - f_{\eta c}) \quad (2.45)$$

where  $M(f_\tau)$  is the range-frequency amplitude spectrum of the transmitted pulse. The azimuth-frequency weighting,  $W(f_\eta - f_{\eta c})$ , is given by [37]

$$W(f_\eta - f_{\eta c}) = w \left( \frac{-r_0 c f_\eta}{2B(f_0 + f_\tau)} \left(1 - \frac{c^2 f_\eta^2}{4(f_0 + f_\tau)^2 B}\right)^{-1/2} - \eta_c \right). \quad (2.46)$$

Thus, it is due to the antenna pattern since different directions within the antenna beam correspond to different azimuth-frequencies in the signal. This weighting is centered on the Doppler centroid,  $f_{\eta c}$ . Finally, the phase of the SAR transfer function in Equation (2.43) contains the phase of the pulse spectrum,  $\Phi_p(f_\tau)$ , and the SAR focussing phase,  $\Phi(f_\eta, f_\tau; r_0)$ . The SAR focussing phase can be shown to be [37, 39]

$$\Phi(f_\eta, f_\tau; r_0) = \frac{-4\pi r_0 (f_0 + f_\tau)}{c} \left( \sqrt{1 - \frac{c^2 f_\eta^2}{4(f_0 + f_\tau)^2 B}} - 1 \right), \quad (2.47)$$

and is dependent on the scatterer's range,  $r_0$ . It is the phase of the SAR transfer function that is most important in SAR processing, since it must be matched accurately in order to perform

the correlation and obtain a focussed image. If the phase were independent of the scatterer's range, then SAR processing could be done simply in the two-dimensional frequency domain by multiplying the data in Equation (2.42) by the conjugate phase, as is done in pulse compression. Then, an inverse Fourier transformation would yield an image that is a bandlimited estimate of the scene. However, the range variance of  $\Phi(f_\eta, f_\tau; r_0)$  makes it difficult to do this for all points in the image. For example, if  $D(f_\eta, f_\tau)$  is multiplied by a conjugate phase that is calculated for a particular range, then the result is an image in which only points at that range are accurately focussed. Thus, the objective in SAR processing is the development of algorithms to accurately match this phase for all ranges in the image, in an efficient manner.

### 2.4.3 Point Spread Function

The description of the SAR signal in the frequency domain can be used to find a description of the two-dimensional point spread function of the processed image. If the range dependent phase of the SAR transfer function is matched accurately, then an inverse two-dimensional Fourier transform of the result gives the point spread function. For the narrow beamwidths in SAR, the region of support of the signal spectrum is approximately rectangular, as illustrated for small squint angles in Figure 2.4. Assuming rectangular functions for the amplitude weightings  $M(f_\tau)$  and  $W(f_\eta)$ , the amplitude spectrum is a two-dimensional rectangular function, and the point spread function is the two-dimensional *sinc* function whose contour plot is shown in the figure.

It should be noted that the point spread function considered here is for the 'single look complex' image, which is formed with the full azimuth bandwidth and is kept in complex form. This is in contrast to the 'multilooked' image, in which separate images are formed from subbands in azimuth-frequency, and then added together in magnitude. This is done to provide an incoherent averaging of the image to reduce speckle [40].

The 3dB resolution width of the point spread function in the range and azimuth directions is an important performance criterion. The resolution determines the minimum distance by

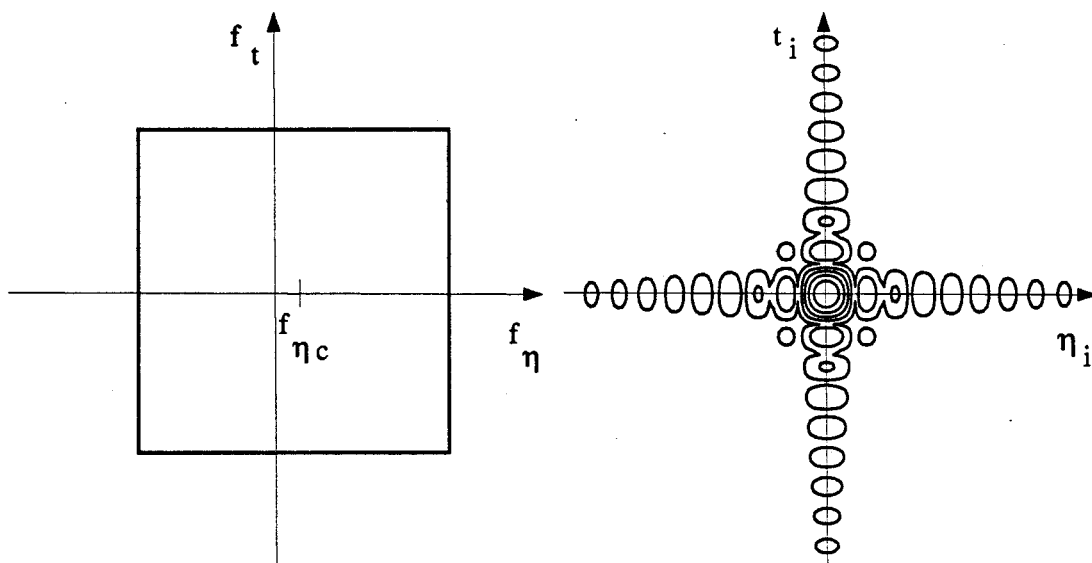


Figure 2.4: Contour plots of two-dimensional amplitude spectrum and point spread function for small squint.

which scatterers need to be separated in order for them to be distinguished in the image, thus indicating the level of detail that can be identified in the scene. As mentioned, the resolution in an accurately processed image is approximately the inverse of the bandwidth in the range and azimuth directions. Letting the transmitted pulse bandwidth be denoted by  $\Delta f_\tau$ , the spatial resolution in the slant range plane is

$$\delta r = \frac{c}{2\Delta f_\tau}. \quad (2.48)$$

In azimuth, the spatial resolution on the surface is

$$\delta x = \frac{v_g L}{2v}, \quad (2.49)$$

which reduces to  $\delta x = L/2$  for a rectilinear geometry. In SAR, the azimuth bandwidth, and hence the theoretical azimuth resolution, is independent of wavelength and (aside from the range dependence of  $v_g$ ) of range.

During processing, an inaccurate matching of the phase of the SAR transfer function causes degradation in the image, which can be characterized by various measurements of the point spread function. First, processing errors can result in a broadening of the 3dB resolution

width of the point spread function in range or azimuth. Another performance criterion is the sidelobe level in the point spread function, which affects the ability to distinguish scatterers in an image when one of the scatterers is particularly strong. In addition, processing errors can cause an error in registration, which refers to the relative position within the image of the point spread function for a scatterer, compared with its expected location. Finally, the phase of the point spread function is very sensitive to inaccuracies in processing. In applications which require the complex image, a variation of the peak phase error with respect to scatterer location leads to measurement errors and creates problems in postprocessing if phase discontinuities are introduced [41]. Thus, applications which require the complex image place very demanding requirements on the accuracy of the processor.

## 2.5 Image Resampling

If an image in spatial ground coordinates is required, then the processed image must be re-sampled. That is, points corresponding to a grid in ground coordinates are interpolated from the image,  $\hat{\sigma}(\eta_i, t_i)$ . In azimuth, the ground coordinate is the distance along the surface in the azimuth direction,  $x = v_g \eta$ . Also, the closest approach range within the image is converted to the distance along the surface in the cross track direction,  $y$ . As a simple example, assume the scatterers lie on a smooth, spherical earth. Then, given a processed image,  $\hat{\sigma}(\eta_i, t_i)$ , the mapping to ground coordinates for a circular orbit geometry is given by

$$\hat{\sigma}_g(x, y) = \hat{\sigma}\left(x/v_g, \frac{2}{c}\sqrt{r_e^2 + H^2 - 2Hr_e \cos\left(\frac{y}{r_e}\right)}\right). \quad (2.50)$$

In addition, the terrain height of a scatterer affects its closest approach range, and this effect can lead to distortions in the image compared to ground truth. Thus, if information about terrain height is available for the scene, then this can be used to obtain a more accurate mapping to ground coordinates [42].

## Chapter 3

### SAR Processing Algorithms

#### 3.1 Introduction

In this chapter, SAR processing algorithms are presented in a common notation in order to compare the approximations they make for computational efficiency. Several SAR processing algorithms are described. The first few algorithms are grouped together as ‘range-Doppler domain’ algorithms, since they perform most of the processing steps in the range-time and azimuth-frequency (Doppler) domain. Next, the polar format algorithm, which is used for spotlight SAR data, is described in order to investigate its squint imaging capability in a strip-mapping context. This is followed by a description of algorithms that have been derived using the wave equation approach which originated in the field of seismic signal processing. Although most of the chapter is review, one contribution that is made is the description of the relationship between the polar format and wave equation algorithms for SAR processing. Finally, the chirp scaling algorithm is described in detail. The notation and concepts for chirp scaling that are presented here form the framework for the extensions to chirp scaling that are derived in later chapters.

#### 3.2 Range-Doppler Domain Algorithms

##### 3.2.1 Mathematical Formulation

Many SAR processing algorithms perform important operations in the range-time and azimuth-frequency domain. This domain allows the coefficients in some processing steps to vary with range, thus accommodating the range-dependence of the SAR transfer function. To provide a

basis for describing these algorithms, it is first necessary to obtain a description of the SAR point scatterer response in the range-time and azimuth-frequency domain. This can be found by an inverse Fourier transformation of the SAR transfer function in the range direction. To facilitate this, it is convenient to express the SAR focussing phase of Equation (2.47) as series expansion in  $f_\tau$  [37, 38, 41]:

$$\Phi(f_\eta, f_\tau; r_0) = \phi_0(f_\eta; r_0) + \phi_1(f_\eta; r_0)f_\tau + \phi_2(f_\eta; r_0)f_\tau^2 + \phi_3(f_\eta; r_0)f_\tau^3 + \dots \quad (3.51)$$

Since higher powers of  $f_\tau$  indicate higher order couplings between the range and azimuth directions in the point scatterer response, the terms of such an expansion can be related to different SAR processing steps. The first term in Equation (3.51) is given by

$$\phi_0(f_\eta; r_0) = \frac{-2\pi f_0 r_0}{c} \left( \sqrt{1 - \frac{c^2 f_\eta^2}{4f_0^2 B(r_0)}} - 1 \right). \quad (3.52)$$

Since this term is independent of  $f_\tau$ , it corresponds to a one dimensional correlation in the azimuth direction, or azimuth compression. To simplify notation, this phase can be combined with the azimuth-frequency amplitude weighting in the SAR transfer function to define the conjugate of the azimuth compression filter:

$$F_{ac}(f_\eta; r_0) = W(f_\eta - f_{\eta c}) \exp[j\phi_0(f_\eta; r_0)]. \quad (3.53)$$

The second term in Equation (3.51) is linear in  $f_\tau$ , thus representing the range migration in the signal relative to the scatterer's location at  $t_0 = 2r_0/c$ , as a function of azimuth-frequency. This coefficient can be expressed as

$$\phi_1(f_\eta; r_0) = -2\pi[\tau_d(f_\eta; r_0) - t_0], \quad (3.54)$$

where  $\tau_d(f_\eta; r_0)$  is the total travel-time delay of the point scatterer response as a function of azimuth-frequency, and this describes the range migration in the azimuth-frequency range-time domain. The expression for the delay has the form

$$\tau_d(f_\eta; r_0) = \frac{2r_0}{c\gamma(f_\eta; r_0)}, \quad (3.55)$$

where  $\gamma(f_\eta; r_0)$  is defined by

$$\gamma(f_\eta; r_0) = \sqrt{1 - \frac{c^2 f_\eta^2}{4f_0^2 B(r_0)}}. \quad (3.56)$$

(For a rectilinear geometry,  $\gamma$  is the cosine of the instantaneous squint angle corresponding to  $f_\eta$ ). The removal of this linear phase term during processing corresponds to aligning the signal energy into a line of constant range, so that azimuth compression can be performed. This step is referred to as range cell migration correction (RCMC). Finally, higher order phase terms in Equation (3.51) represent a range distortion which needs to be compensated by a secondary range compression (SRC) filter [43, 44]. For moderate squint angles, it is sufficient to include only the quadratic term, which is

$$\phi_2(f_\eta; r_0) = \frac{\pi c r_0 f_\eta^2}{2B(r_0) f_0^3 \gamma^3(f_\eta; r_0)}. \quad (3.57)$$

Assuming a linear FM transmitted pulse with frequency rate  $K$ , this phase term can be combined with the phase of the Fourier transform of a linear FM pulse to define a modified frequency rate,  $K_m$ , which is azimuth-frequency and range dependent:

$$\frac{\pi}{K_m(f_\eta; r_0)} = \frac{\pi}{K} + \phi_2(f_\eta; r_0). \quad (3.58)$$

For high squint, the cubic phase term in Equation (3.51) can have a noticeable effect on secondary range compression [45], and is given by:

$$\phi_3(f_\eta; r_0) = \frac{-\pi c r_0 f_\eta^2}{2f_0^4 B(r_0) \gamma^5(f_\eta; r_0)}. \quad (3.59)$$

Using the above definitions, assuming a linear FM pulse and keeping phase terms up to the quadratic, the range-Doppler domain representation of the point scatterer response can be found to be

$$S(f_\eta, \tau; r_0) = F_{ac}(f_\eta; r_0) m \left[ \frac{K_m}{K} (\tau - (\tau_d - t_0)) \right] \exp[-j\pi K_m (\tau - (\tau_d - t_0))^2]. \quad (3.60)$$

In this domain, the signal consists of linear FM pulses of frequency rate  $K_m(f_\eta; r_0)$ , delayed by the range migration trajectory  $(\tau_d(f_\eta; r_0) - t_0)$ , and multiplied by the azimuth compression

term,  $F_{ac}(f_\eta; r_0)$ . Finally, note that the modification of the range frequency rate to  $K_m$  causes a corresponding change in the length of the uncompressed range pulse, in the range-Doppler domain, to:

$$T_m = \frac{K}{K_m} T. \quad (3.61)$$

### 3.2.2 Range-Doppler With SRC

The range-Doppler algorithm was the first algorithm used for digital processing of spaceborne SAR data, and is still the most commonly used SAR processing algorithm [14, 15]. The operations of the range-Doppler algorithm consist of:

1. Range compression of received echoes via a range FFT, matched filter multiply, and range inverse FFT. SRC is incorporated approximately by modifying the frequency rate of the range matched filter to  $K_m(f_{\eta c}; r_{ref})$ , assuming  $K_m$  to be constant. This allows SRC to be performed without an increase in computation.
2. Azimuth FFT. The received SAR data are stored in the format of successive range lines. In this form, it is easier to access data in the range direction, especially if it is stored on disk. Thus, in order to access lines of data in the azimuth direction for the azimuth FFT, the data on disk must be transposed or ‘corner turned’.
3. RCMC by means of extracting data values along the range migration curve and shifting them to the same range bin. This requires an interpolation between range data samples, and the range dependence of RCMC means that the interpolating kernel is range dependent. In addition, the interpolator is truncated for efficiency. Since the resulting interpolation error depends on azimuth-frequency, this can introduce artifacts into the image such as paired echoes of strong scatterers [16].
4. Azimuth compression by an azimuth matched filter multiply.
5. Azimuth inverse FFT.

As mentioned, the range-Doppler algorithm makes the approximation of computing the coefficient of the SRC filter at the Doppler centroid and at a reference range. This provides for adequate focussing for the small squint angles experienced in conventional SAR. However, the azimuth-frequency dependence of SRC begins to cause a degradation in focussing for moderate values of squint [44, 39]. Considering a scatterer at the reference range, the error in matching the quadratic phase of the SAR transfer function is

$$\phi_{err}(f_\eta, f_\tau) = [\phi_2(f_\eta; r_{ref}) - \phi_2(f_{\eta c}; r_{ref})]f_\tau^2. \quad (3.62)$$

This results in a range compression error with the accompanying broadening of the 3dB resolution width, increased sidelobe level, and phase error. The compression error varies with azimuth-frequency, being zero at the Doppler centroid and greatest at the edges of the azimuth-frequency band. Thus, after azimuth compression, the result is an overall range broadening and distortion of the point spread function. The azimuth-frequency dependence of SRC depends on the wavelength. As an example, for an L-band spaceborne SAR such as Seasat, the overall broadening exceeds 10 percent for squint angles above 6 degrees [44].

### 3.2.3 Squint Imaging Mode Algorithm

A modification of the range-Doppler algorithm, called the Squint Imaging Mode (SIM) algorithm, was proposed to overcome the problem of the azimuth-frequency dependence of SRC and provide more accurate focussing for moderate squint angles [24]. In this algorithm, SRC is performed as a separate step after range compression and azimuth FFT so that the SRC filter can be calculated for each azimuth-frequency. Thus, after the azimuth FFT, SRC is performed on each range line by a range FFT, multiply by the SRC filter, and range inverse FFT. The ability to access range lines at this stage in processing requires extra corner turns before and after SRC. The remaining steps of RCMC and azimuth compression proceed as in the original range-Doppler algorithm, so that RCMC still requires a range-variant interpolator.

For the squint angles that can be accommodated by this algorithm, the cubic phase term in Equation (3.51) may become noticeable, and this term can be incorporated into the SRC

filter [45]. The SRC filter is calculated at the reference range, and the phase of the SRC filter in the two-dimensional frequency domain becomes:

$$\phi_{SRC}(f_\eta, f_\tau) = \phi_2(f_\eta; r_{ref})f_\tau^2 + \phi_3(f_\eta; r_{ref})f_\tau^3. \quad (3.63)$$

This algorithm matches the phase of the SAR transfer function for scatterers at the reference range. However, at high squint angles the range dependence of SRC becomes noticeable. Assuming that the cubic phase term is still small enough that its range-dependence can be neglected, the error in matching the phase of the SAR transfer function for a scatterer at  $r_0$  is given by

$$\phi_{err}(f_\eta, f_\tau; r_0) = [\phi_2(f_\eta; r_0) - \phi_2(f_\eta; r_{ref})]f_\tau^2. \quad (3.64)$$

This results in a range compression error at all azimuth-frequencies in the band, which increases for scatterers located further away from the reference range. One way to accommodate this error is to process smaller range blocks so that the range dependent SRC error within a block does not become too large. However, at high squint the range dependence of SRC is severe enough that the range blocks have to be quite small. Also, increasing squint increases the amount of range migration, which increases the amount of throwaway in performing RCMC. Thus, at high squint, block processing in range becomes inefficient.

Accommodation of the azimuth-frequency dependence of SRC requires some processing to take place in the two-dimensional frequency domain, and this introduces the problem of the range variation of the Doppler centroid. Figure 3.5 shows two range migration curves in the range-Doppler domain, indicated by the dotted lines, for scatterers at different ranges. The Doppler centroids at the different ranges are  $f_{\eta c1}$  and  $f_{\eta c2}$ , respectively, and the corresponding locations of signal energies are indicated by the heavy lines. The signals are wrapped around in azimuth-frequency because of sampling by the *PRF*. If the Doppler centroid varies by more than the amount by which the signal is oversampled, then the wraparound causes a single azimuth-frequency bin to contain signals at different ranges whose range migration delays and SRC filters are calculated with different values of  $f_\eta$ . This does not pose a problem for operations

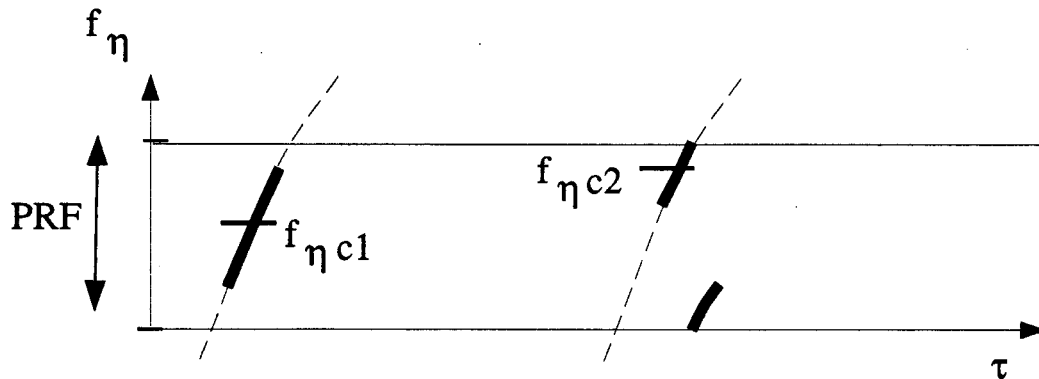


Figure 3.5: Aliased range migration curves with Doppler centroid variation.

that are performed in the range-Doppler domain. However, in the two dimensional frequency domain, this effect prevents accurate SRC from being performed across the entire range swath. For small squint angles, Doppler centroid variation can be accommodated by processing smaller range blocks. However, in squint mode SAR it is generally necessary to control the amount of Doppler centroid variation by proper steering of the yaw and pitch angles of the antenna [24]. This will be discussed further in Chapter 4.

### 3.2.4 Time Domain SRC

Finally, there exists the possibility of a time domain filtering approach to SRC. Assuming the range compression filter is calculated to include SRC at the Doppler centroid and at the reference range, then residual SRC is needed to fully compress the signal at other azimuth-frequencies and ranges. Residual compression of the signal can be performed by a range-variant, range-time domain filter implemented in the range-Doppler domain [46]. This would accommodate the azimuth-frequency and range dependence of SRC, as well as a variation in Doppler centroid. However, such an approach would significantly increase the computational complexity and the difficulty of implementation of the processor.

### 3.3 Polar Format Algorithm

The polar algorithm was first derived for SAR imaging of rotating objects from a fixed or moving platform [20]. It was applied to airborne spotlight SAR, which is a mode of SAR imaging in which the antenna is continuously steered to point at a fixed, small area of the surface, in order to obtain a very high resolution image. The polar algorithm is also related to the tomographic approach to spotlight SAR processing [21, 22, 23]. The idea of polar processing can be described briefly as follows: Consider a small area of scatterer distribution near a reference point in the scene located at  $(\eta_a, t_a)$ , where  $t_a = 2r_a/c$  is the closest-approach range-time. Each azimuth position of the platform, and hence each range line in the data, corresponds to a certain viewing angle to the reference point. Then, the samples of the Fourier transformed, compressed range lines can be arranged on a polar grid, with each range line placed according to its viewing angle. It can be shown that the result is a polar coordinate sampling of the two-dimensional Fourier transform of the scene. Thus, by interpolating points from the polar format onto a rectangular grid, the image can be obtained by a two-dimensional inverse FFT.

Now, consider applying this method to the strip-map SAR data described earlier by Equation (2.38). First, the received pulses are range compressed, and the platform to scatterer distance is normalized by the distance to the reference point. This can be done in the range-frequency domain by the multiplication of range lines by the factor:

$$\exp[j2\pi(f_0 + f_\tau)R(\eta - \eta_a; r_a)/c]. \quad (3.65)$$

The resulting data can be described by (noting that  $r_0 = 2t_0/c$  and  $r_a = 2t_a/c$ ):

$$D_a(\eta, f_\tau) = \iint \sigma'(\eta_0, t_0)M(f_\tau)w(\eta - \eta_0 - \eta_c)e^{-j2\pi\frac{(f_0 + f_\tau)}{c}(R(\eta - \eta_0; r_0) - R(\eta - \eta_a; r_a))}d\eta_0 dt_0. \quad (3.66)$$

The polar algorithm amounts to casting this expression into the form of a two dimensional Fourier transform of the scene. To do this, the phase of the integrand in Equation (3.66) can be considered as a function of scatterer position,  $(\eta_0, t_0)$ , and expanded about the reference point.

Assuming that  $B$  is constant, this gives

$$2\pi \frac{(f_0 + f_\tau)}{c} [R(\eta - \eta_0; r_0) - R(\eta - \eta_a; r_a)] \approx 2\pi f_a(\eta_0 - \eta_a) + 2\pi(f_0 + f_t)(t_0 - t_a) + \phi_{err}, \quad (3.67)$$

where the frequency variables,  $f_a$  and  $f_t$ , result from the change of variables defined by

$$f_a = \frac{-2B(f_0 + f_\tau)(\eta - \eta_a)}{c\sqrt{r_a^2 + B(\eta - \eta_a)^2}} \quad (3.68)$$

and

$$\begin{aligned} (f_0 + f_t) &= \frac{c(f_0 + f_\tau)t_a}{2\sqrt{r_a^2 + B(\eta - \eta_a)^2}} \\ &= \sqrt{(f_0 + f_\tau)^2 - \frac{c^2 f_a^2}{4B}}. \end{aligned} \quad (3.69)$$

By keeping only linear terms in the expansion, and making the change of variables, Equation (3.66) becomes

$$D(f_a, f_t) = \iint \sigma(\eta_0, t_0) M'(f_t) W(f_a - f_{ac}) e^{-j2\pi f_a(\eta_0 - \eta_a) - j2\pi f_t(t_0 - t_a)} d\eta_0 dt_0. \quad (3.70)$$

Thus, a two-dimensional inverse Fourier transform with respect to the frequency variables  $f_a$  and  $f_t$  provides the image. In Equation (3.70), the reflectivity distribution is given by

$$\sigma(\eta_0, t_0) = \sigma'(\eta_0, t_0) \exp[-j2\pi f_0(t_0 - t_a)], \quad (3.71)$$

which includes the range dependent scatterer phase. The amplitude in the new range frequency variable,  $f_t$  is

$$M'(f_t) = M\left(\sqrt{(f_0 + f_t)^2 + \frac{c^2 f_a^2}{4B}} - f_0\right). \quad (3.72)$$

Also, the weighting in the frequency variable,  $f_a$ , is given by

$$W(f_a - f_{ac}(\eta_0)) = w\left(\frac{-c^2 t_a f_a}{4B(f_0 + f_t)} + \eta_a - \eta_0 - \eta_c\right) \quad (3.73)$$

which is centered on the parameter

$$f_{ac}(\eta_0) = \frac{-4B(f_0 + f_t)}{c^2 t_a} (\eta_c + \eta_0 - \eta_a) \quad (3.74)$$

which depends on the scatterer's azimuth position,  $\eta_0$ . The dependence of the azimuth weighting on the scatterer's azimuth position is a consequence of the fact that the viewing angles used to form a polar grid in the frequency domain are assumed to be those associated with the reference point. Thus the  $f_a$  variable only corresponds to true azimuth-frequency,  $f_\eta$ , for the signal received from a scatterer at  $\eta_a$ . For scatterers at other azimuth positions,  $f_a$  is not identical to  $f_\eta$ , with the result that the centroid of signal energy in  $f_a$  depends on  $\eta_0$ . This effect does not occur in spotlight SAR because of the continuous steering of the antenna.

The higher order terms in the expansion in Equation (3.67), indicated by  $\phi_{err}$ , represent an error in the algorithm that increases for scatterers located away from the reference point in either azimuth or range. The phase error term can be expressed as a function of frequency variables and scatterer position as

$$\phi_{err}(f_a, f_t; \eta_0, t_0) = \frac{\pi \frac{c^2}{4} B [\frac{c^2}{4} (f_0 + f_t) (\eta_0 - \eta_a) - \frac{f_a}{B} (t_0 - t_a)]^2}{t_a (f_0 + f_t) [1 + \frac{c^2 f_a^2}{4 (f_0 + f_t)^2 B}]}. \quad (3.75)$$

The greatest effect of this error is a geometric distortion due to the range and azimuth registration errors that vary with both the range and azimuth position of the scatterer [20]. This distortion exists even at zero squint, and for L-band or C-band spaceborne data, the registration error at a point 10 km away from the reference point is greater than 20 cells. Other effects of this approximation are phase errors and small focussing errors that vary with azimuth and range.

A problem which arises in applying the polar algorithm to strip-map SAR data is that the width of the image in azimuth can be several times the aperture. Thus, the interval of viewing angles experienced by all scatterers in the image is several times the interval of viewing angles corresponding to a single scatterer at the reference point. This causes the interval of the  $f_a$  variable in Equation (3.68) to be several times greater than the normal azimuth bandwidth, as indicated by the variation of  $f_{ac}$  with  $\eta_0$ . Thus, several times the number of frequency domain points have to be interpolated, and the size of the inverse FFT is increased.

Converting from the polar format to the rectangular grid according to the change in variables in Equations (3.68) and (3.69) requires interpolation in both directions in the frequency domain.

Such interpolation has to be done very accurately to avoid artifacts in the image, and is thus very computationally expensive [21, 47]. For this reason, more efficient algorithms such as convolution backprojection have been developed for tomographic processing of spotlight SAR data [22]. However, since these algorithms still depend on a polar representation of the data, it is not clear if they can be extended to strip-map SAR efficiently.

Finally, one way to process strip-map data using the polar algorithm is to divide the data into subpatches, each a fraction of an aperture long, and process each subpatch with the polar algorithm. However, this method requires a large amount of processing overhead in the required filtering of each subpatch and in the mosaicing of subpatches to form an image [23].

### 3.4 Wave Equation Algorithms

#### 3.4.1 Stolt Interpolation

An approach to SAR processing has been derived using wave equation techniques taken from the field of seismic migration [32]. In this approach, scatterers distributed in azimuth and closest approach range are assumed to be pulse sources, and the received SAR data are samples of the resulting wavefield in the azimuth and travel-time dimensions. After two-dimensional Fourier transformation of the data, each point in the two-dimensional frequency domain represents the complex amplitude of a monochromatic plane wave with a certain frequency travelling in a certain direction. Given the transformed data, then, each component wave can be back-propagated or ‘downward continued’ to a particular range by the multiplication of each point by a complex exponential [48, 49]. Inverse transformation of the result, evaluated at zero travel-time, gives the wavefield at the desired range when the signal was emitted — that is, the complex reflectivity of the scatterers at that range. Performing this operation for every value of range in the image gives the processed image [50]. This method is general in that it can be used even if the speed of propagation varies with range, as it can in a seismic context. If the speed of propagation is constant, as in the SAR case (neglecting atmospheric effects), then a simpler

procedure can be used. It can be shown that after properly moving data points in the two-dimensional frequency domain — a technique known as Stolt interpolation — the downward continuation of the data to all ranges can be done simply by a two-dimensional inverse Fourier transformation [47].

To understand this technique in the context of SAR processing, begin with the description of the two-dimensional Fourier transform of the SAR data given in Equation (2.42). First, it is convenient to define a reference closest approach range-time,  $t_{ref} = 2r_{ref}/c$ , near midswath. Then, the range-time location of a scatterer can be measured by  $\Delta t = t_0 - t_{ref}$ . The SAR data can be focussed at the reference range by multiplying the transformed data by the conjugate phase of the SAR transfer function at  $r_{ref}$ . This is equivalent to downward continuation of the data to  $r_{ref}$ , and the result is

$$D_{ref}(f_\eta, f_\tau) = \iint \sigma(\eta_0, \Delta t) G A(f_\eta, f_\tau) e^{j(\Phi(f_\eta, f_\tau; r_0) - \Phi(f_\eta, f_\tau; r_{ref}))} e^{-j2\pi f_\tau \Delta t - j2\pi f_\eta \eta_0} d\Delta t d\eta_0, \quad (3.76)$$

where now the range dimension in  $\sigma$  is measured with respect to  $t_{ref}$ . The remaining unmatched phase is due to the range dependence of the SAR transfer function. Referring to the definition of the SAR focussing phase in Equation (2.47),  $\Phi(f_\eta, f_\tau; r_0)$  varies linearly with  $r_0$  if  $B$  is constant. In this case, the phase in Equation (3.76) above can be written as a linear function of  $\Delta t$ :

$$[\Phi(f_\eta, f_\tau; r_0) - \Phi(f_\eta, f_\tau; r_{ref})] = -2\pi \Delta t \left[ \sqrt{(f_0 + f_\tau)^2 - \frac{c^2 f_\eta^2}{4B}} - (f_0 + f_\tau) \right]. \quad (3.77)$$

This linearity in  $\Delta t$  allows the expression in Equation (3.76) to be cast into the form of a two dimensional Fourier transform by making the following change of variables in the range-frequency dimension:

$$f_t = \left( \sqrt{(f_0 + f_\tau)^2 - \frac{c^2 f_\eta^2}{4B}} - f_0 \right). \quad (3.78)$$

This gives:

$$D'_{ref}(f_\eta, f_t) = \iint \sigma(\eta_0, \Delta t) G' A'(f_\eta, f_t) e^{-j2\pi f_t \Delta t - j2\pi f_\eta \eta_0} d\Delta t d\eta_0, \quad (3.79)$$

which is a Fourier transform of a bandlimited estimate of the scene. This is expressed as a function of the frequency variables  $(f_\eta, f_t)$ , which correspond to the image dimensions  $(\eta_0, \Delta t)$ .

The amplitude spectrum which bandlimits the image is  $A'(f_\eta, f_t) = A(f_\eta, f_\tau)$ , and the nearly constant factor  $G'$  is given by

$$G' = G_p \sqrt{\frac{cr_0}{2B(f_0 + f_\tau)}} [(f_0 + f_\tau)^2 + \frac{c^2 f_\eta^2}{4B}]^{-1/4}. \quad (3.80)$$

Thus, the Stolt interpolation technique consists of interpolating points in the two-dimensional transform of the data, and moving them to a grid in the frequency variables which correspond to the two-dimensional Fourier transform of the image.

The comparison of the polar format and wave equation algorithms revealed a relationship between them that has not been previously understood. Both algorithms involve a change of variables in the frequency domain, with the objective of matching the range dependent SAR transfer function in order to focus the data. In both cases, the linear component of the range dependence of the SAR transfer function phase is matched by taking advantage of the definition of the Fourier transform. In fact, as a function of the azimuth frequency variable used in each case, it can be seen by comparing Equations (3.78) and (3.69) that the range-frequency interpolations in both algorithms are equivalent. The difference between the algorithms is in the definition of the azimuth-frequency variable. In the polar algorithm, it is assumed that all scatterers are relatively close together so that the relationship between azimuth-time and azimuth-frequency for all scatterers is assumed to be the same as that for the scatterer at the reference point. The interpolation in azimuth in the polar algorithm does an approximate conversion from azimuth-time to azimuth-frequency, and then the interpolation in range-frequency provides the focussing. In the Stolt method, the requirement that the scatterers be close together is removed by taking the azimuth Fourier transform of the data. Interpolation is then done in only the range-frequency dimension to provide focussing.

### 3.4.2 Approximations

Interpolation of data in the frequency domain results in artifacts such as shading in the image unless the interpolation is done very accurately [47]. Thus, the Stolt interpolation method is very computationally expensive if implemented directly. For this reason, a wave equation

algorithm for SAR processing has been derived which makes approximations in order to simplify the Stolt method [32]. By approximating the change of variables in Equation (3.78) by

$$f_t = f_r - f_0 \left(1 - \sqrt{1 - \frac{c^2 f_r^2}{4 f_0^2 B}}\right), \quad (3.81)$$

the interpolation reduces to a simple range-frequency shift. This can be implemented in the range-Doppler domain by multiplying the data by the azimuth-frequency dependent complex exponential:

$$\exp[-j2\pi \Delta t f_0 \left(1 - \sqrt{1 - \frac{c^2 f_r^2}{4 f_0^2 B}}\right)]. \quad (3.82)$$

Considered in the azimuth direction in the range-Doppler domain, this operation is equivalent to a residual azimuth compression that depends on range. In addition, the range-Doppler domain allows any range dependence of  $B(r_0)$  to be included in this residual azimuth compression.

Thus, this algorithm consists of first applying a two-dimensional frequency domain multiply which downward continues the data to a reference range. This is equivalent to performing a bulk range-invariant azimuth compression, RCMC, and SRC in the two-dimensional frequency domain. This is followed by a residual azimuth compression in the range-Doppler domain. However, because of the approximation to the change of variables that is made in this algorithm, RCMC and SRC are performed accurately only at the reference range. Neglecting the range dependence of RCMC allows it to be performed without an interpolator. However, the uncorrected residual range migration can cause a noticeable error for moderate squint angles [39].

### 3.5 Chirp Scaling Algorithm

Approximations to SAR processing to eliminate the need for an interpolator, as in the approximations to the wave equation approach, have left the range dependence of RCMC unaccommodated. Recently, the chirp scaling algorithm has been developed as a means to provide accurate SAR processing without implementing an interpolator [17, 18, 19]. The chirp scaling algorithm takes advantage of the properties of uncompressed, linear FM pulses in order to remove the range dependence of RCMC. This is done by the multiplication of uncompressed range lines in

the azimuth-frequency range-time domain by a chirp scaling phase function. Then, bulk RCMC and SRC are performed in the two-dimensional frequency domain, and SRC is allowed to vary with azimuth-frequency. Finally, azimuth compression is performed in the range-Doppler domain. In this algorithm, all operations are performed with either multiply or FFT operations. Also, as in the squint imaging mode algorithm, extra corner turns are required to access range lines after the azimuth FFT, and to access azimuth lines before azimuth compression.

The chirp scaling technique is a way of removing the range dependence of RCMC. The idea is to scale the range-time axis at each azimuth-frequency, using the property of linear FM pulses, so that the range migration trajectories of scatterers at all ranges have the same shape as the trajectory at a reference range. Once this is done, the remaining bulk RCMC is range-invariant and can be done in the two-dimensional frequency domain. To develop a mathematical representation of the chirp scaling algorithm, refer to the formulation of the point scatterer response in the range-Doppler domain given in Equation (3.60). Also, let the point scatterer response include the delay to the scatterer's position, so that the representation of the signal becomes

$$S(f_\eta, \tau; r_0) = F_{ac}(f_\eta; r_0) m\left[\frac{K_m}{K}(\tau - \tau_d)\right] \exp[-j\pi K_m(\tau - \tau_d)^2]. \quad (3.83)$$

For a scatterer at range  $r_0$ , the range migration trajectory is denoted by  $\tau_d(f_\eta; r_0)$ , as shown in Figure 3.6. To simplify notation, define  $\tau_{ref}(f_\eta)$  to be the trajectory at the reference range, so that  $\tau_{ref}(f_\eta) = \tau_d(f_\eta; r_{ref})$ . The objective of chirp scaling is to change the scatterer trajectory at  $r_0$  to a desired trajectory,  $\tau_s(f_\eta; r_0)$ , which has the same shape as the reference trajectory, as shown in the figure. The desired trajectory intersects the original scatterer trajectory at a reference azimuth-frequency,  $f_{\eta r}$ . This reference azimuth-frequency is the point along the scatterer trajectory that is chosen for the final range-time location of the scatterer in the image [37, 51, 52]. For small squint angles  $f_{\eta r}$  can be zero, so that the scatterer is registered to  $t_0$ . However, for high squint angles the Doppler centroid is large enough that the delay due to range migration can be on the order of the pulse length, causing problems for chirp scaling. Thus, the reference azimuth-frequency should be in the vicinity of the Doppler centroid. Once

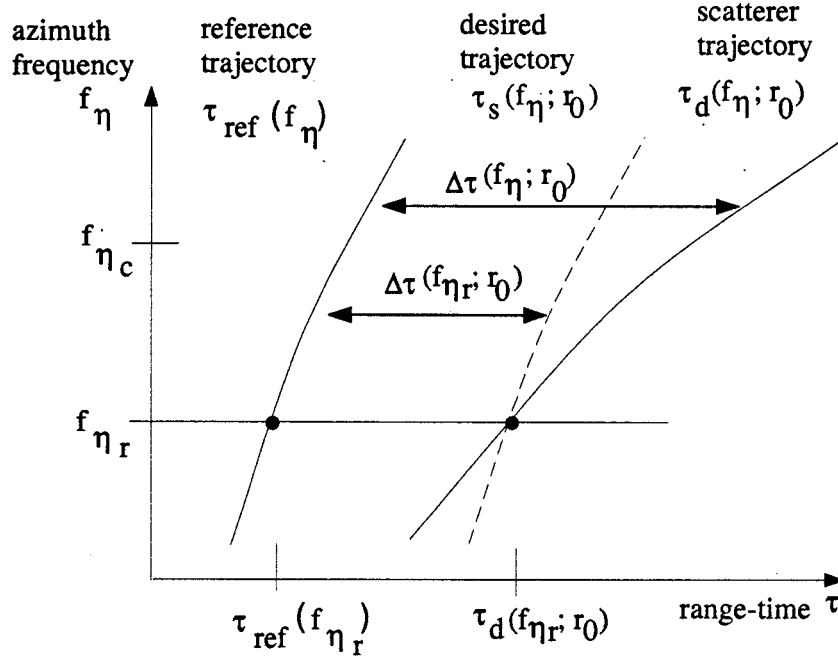


Figure 3.6: Range migration trajectories in chirp scaling.

the trajectory has been scaled to  $\tau_s(f_\eta; r_0)$ , the bulk RCMC is the same as the range migration of the reference trajectory about the point at  $f_{\eta r}$ . In this sense, the desired scaled trajectory for the scatterer at  $r_0$  can be expressed as

$$\tau_s(f_\eta; r_0) = \tau_d(f_{\eta r}; r_0) + [\tau_{ref}(f_\eta) - \tau_{ref}(f_{\eta r})], \quad (3.84)$$

where  $\tau_d(f_{\eta r}; r_0)$  is the scatterer position in the coordinate system determined by  $f_{\eta r}$ , and  $[\tau_{ref}(f_\eta) - \tau_{ref}(f_{\eta r})]$  is the range-invariant bulk RCMC.

At each azimuth frequency, it is convenient to measure range-time from the reference trajectory. Let  $\Delta\tau(f_\eta; r_0)$  be the delay from the reference trajectory to the scatterer trajectory at  $r_0$ , as shown in Figure 3.6, so that

$$\tau_d(f_\eta; r_0) = \tau_{ref}(f_\eta) + \Delta\tau(f_\eta; r_0). \quad (3.85)$$

The purpose of scaling is to achieve the desired trajectory whose delay from the reference trajectory is constant in azimuth-frequency, being equal to the delay at  $f_{\eta r}$ . Thus, the desired

trajectory for a scatterer at  $r_0$  can be written as

$$\tau_s(f_\eta; r_0) = \tau_{ref}(f_\eta) + \Delta\tau(f_{\eta r}; r_0). \quad (3.86)$$

Comparing this to the original scatterer trajectory in Equation (3.85), it can be seen that the objective of the scaling operation is to change  $\Delta\tau(f_\eta; r_0)$  to  $\Delta\tau(f_{\eta r}; r_0)$  for scatterers at all ranges. From the definition of the range migration trajectory in Equation (3.55), the reference trajectory is given by

$$\tau_{ref}(f_\eta) = \frac{2r_{ref}}{c\gamma(f_\eta; r_{ref})}. \quad (3.87)$$

Now, by assuming that the  $B$  parameter is constant and equal to the value at the reference range, that is  $B(r_0) \approx B(r_{ref})$ , the original scatterer trajectory can be approximated by

$$\tau_d(f_\eta; r_0) \approx \frac{2r_0}{c\gamma(f_\eta; r_{ref})}. \quad (3.88)$$

By making this approximation, it is assumed that the delay to the range migration curve at a particular azimuth-frequency varies linearly with  $r_0$ . Thus,  $\Delta\tau(f_\eta; r_0)$  and  $\Delta\tau(f_{\eta r}; r_0)$  are both assumed linear in  $(r_0 - r_{ref})$ , and are related by

$$\Delta\tau(f_{\eta r}; r_0) = \Delta\tau(f_\eta; r_0)/\alpha(f_\eta), \quad (3.89)$$

where  $\alpha(f_\eta)$  is an azimuth-frequency dependent scale factor:

$$\alpha(f_\eta) = \frac{\gamma(f_{\eta r}; r_{ref})}{\gamma(f_\eta; r_{ref})}. \quad (3.90)$$

Thus, given the assumption of a constant  $B$ , the desired trajectory is

$$\tau_s(f_\eta; r_0) \approx \tau_{ref}(f_\eta) + \frac{\Delta\tau(f_\eta; r_0)}{\alpha(f_\eta)}. \quad (3.91)$$

In this case, a linear scaling of each range-time axis, with respect to the reference trajectory, is sufficient to remove the range dependence of RCMC.

Such a scaling can be achieved by taking advantage of the properties of linear FM pulses. This is illustrated in Figure 3.7, which is a frequency-time diagram of a range line, at a particular azimuth-frequency, containing two scatterers. One of the scatterers is at the reference range,

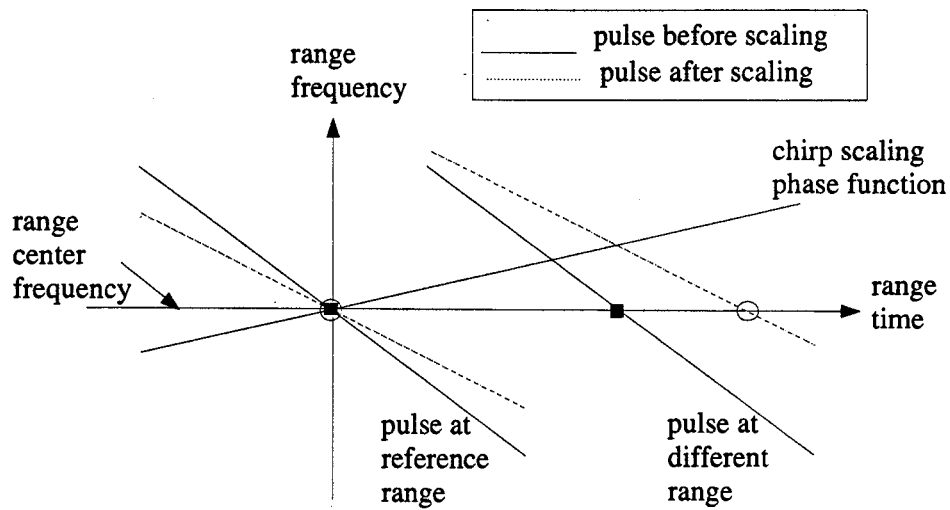


Figure 3.7: Frequency-time diagram of range line with linear FM pulses.

the other is located away from the reference range. A frequency-time curve of a pulse is a plot of instantaneous frequency versus time, which for a linear FM pulse is a straight line. In the figure, the solid frequency-time curves correspond to the two pulses before scaling. Pulses compress to the point where the frequency-time curve intersects the center frequency of the range matched filter, shown by the solid squares for the pulses before scaling. Also shown in the figure is the curve for the chirp scaling phase function. Multiplying the range line by the chirp scaling phase function has the effect of shifting the frequency-time curves of the pulses, and the curves after scaling are shown by the dotted lines. This shifting of the curves affects the location of the compressed pulses after scaling, indicated in the figure by the open circles. The shift in the location of the compressed pulses is range dependent, being zero for scatterers at the reference range and increasing away from the reference range. This range-dependent shift accomplishes the scaling effect.

If a linear scaling is required, as in the case of a constant  $B$ , and assuming that the frequency rate in the range signal is range-invariant so that  $K_m(f_\eta; r_0) \approx K_m(f_\eta; r_{ref})$ , then the chirp scaling phase function for a given range line is a quadratic phase function centered on the

reference trajectory. Given the range-Doppler representation of the signal,  $S(f_\eta, \tau; r_0)$ , and letting  $S_\alpha(f_\eta, \tau; r_0)$  be the chirp scaled signal, the scaling operation can be expressed as

$$S_\alpha(f_\eta, \tau; r_0) = S(f_\eta, \tau; r_0) \exp[-j\pi q_2(f_\eta)(\tau - \tau_{ref})^2], \quad (3.92)$$

where  $q_2(f_\eta)$  is the coefficient of the chirp scaling phase function.

After multiplying  $S(f_\eta, \tau; r_0)$  by the chirp scaling phase function,  $S_\alpha(f_\eta, \tau; r_0)$  is Fourier transformed with respect to  $\tau$  to give the SAR transfer function of the chirp scaled signal. As in Equation (3.51), the phase of the transfer function can be expanded in  $f_\tau$  to give terms that correspond to processing steps. To derive the required value of  $q_2(f_\eta)$ , consider the phase term corresponding to RCMC. To simplify notation, let the range frequency rate, which is assumed range-invariant and equal to the value at the reference range, be denoted by  $K_{mref}(f_\eta)$ . In the chirp scaled signal, the resulting scaled trajectory for a scatterer at  $r_0$  can be shown to be

$$\hat{\tau}_s(f_\eta; r_0) = \tau_{ref}(f_\eta) + \frac{K_{mref}(f_\eta)}{K_{mref}(f_\eta) + q_2(f_\eta)} \Delta\tau(f_\eta; r_0). \quad (3.93)$$

By comparing this with the approximation to the desired trajectory in Equation (3.91), it can be seen that  $q_2(f_\eta)$  can be chosen to give the required linear scale factor,  $\alpha(f_\eta)$ , as follows:

$$q_2(f_\eta) = K_{mref}(f_\eta)[\alpha(f_\eta) - 1]. \quad (3.94)$$

With the chirp scaling phase function thus defined, the chirp scaling algorithm can be described in detail. A block diagram is shown in Figure 3.8. First, the data is Fourier transformed in the azimuth direction to get to the range-Doppler domain. Then range lines are multiplied by the chirp scaling phase function. Next, a range FFT takes the chirp scaled data to the two-dimensional frequency domain. Using the signal representation given by Equations (3.83) and (3.92), the SAR transfer function of the chirp scaled signal becomes

$$\begin{aligned} S_{2\alpha}(f_\eta, f_\tau; r_0) &= M\left(\frac{f_\tau - \delta f_\tau}{\alpha}\right) \exp[-j2\pi\tau_d(f_\eta; r_0)f_\tau] \\ &\quad \exp[-j2\pi(\tau_{ref}(f_\eta) - \tau_{ref}(f_\eta))f_\tau] \exp\left[j\pi\frac{f_\tau^2}{\alpha K_{mref}}\right] \\ &\quad F_{ac}(f_\eta; r_0) \exp[j\phi_\Delta(f_\eta; r_0)]. \end{aligned} \quad (3.95)$$

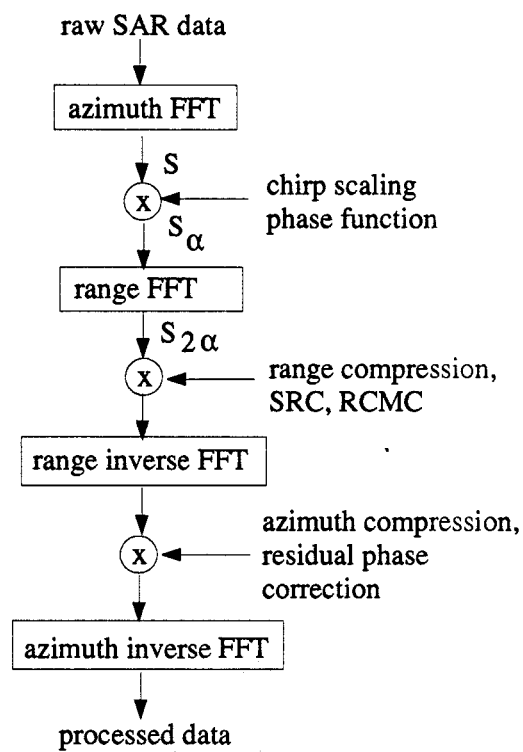


Figure 3.8: Block diagram of chirp scaling algorithm.

The factors of this expression correspond to processing steps and properties of the range pulse. The first factor is the amplitude spectrum of the range compressed pulse,  $M[(f_\tau - \delta f_\tau)/\alpha]$ , in which the range bandwidth is scaled by  $\alpha$ . At this point it is also shifted by an amount  $\delta f_\tau = -q_2 \Delta\tau(f_\eta; r_0)$ , because of the chirp scaling phase function multiply. Following the amplitude spectrum is an exponential factor with a linear phase in  $f_\tau$  that gives the scatterer's range position in the image,  $\tau_d(f_{\eta r}; r_0)$ . The next factor in Equation (3.95) has a linear phase in  $f_\tau$  whose coefficient depends on azimuth-frequency, but not on range. This is the bulk RCMC that can be removed by multiplying the signal by the conjugate of this phase term in the two-dimensional frequency domain. Following this is an exponential with a phase that is quadratic in  $f_\tau$ , which gives the range compression filter including azimuth-frequency dependent SRC. In this filter the frequency rate has been multiplied by  $\alpha$ . Assuming the frequency rate is range invariant, range compression is performed by removing this phase term by a conjugate multiply in the two-dimensional frequency domain. Finally, the azimuth compression filter is indicated by  $F_{ac}(f_\eta; r_0)$ , and this is augmented by a phase correction,  $\phi_\Delta(f_\eta; r_0)$ . The correction is necessary to remove a range dependent phase that is introduced into the data by the chirp scaling phase function multiply. It is given by

$$\phi_\Delta(f_\eta; r_0) = -\pi K_{mref} \left(1 - \frac{1}{\alpha}\right) \Delta\tau(f_\eta; r_0)^2. \quad (3.96)$$

The range dependence of azimuth compression and the phase correction can be accommodated by performing these steps after a range inverse transform has taken the data to the range-Doppler domain. Finally, an azimuth inverse FFT provides the processed image.

## Chapter 4

### Considerations for High Squint

#### 4.1 Introduction

The effects of a squint mode imaging geometry on SAR signal properties have not been thoroughly understood. This chapter examines the effects of high squint on the signal properties, signal modelling, and image properties in spaceborne SAR. Contributions of the chapter include the following: First, a derivation of squint angle as a function of yaw, pitch, and elevation is presented for the general case of large squint angles. Then a method for calculating the yaw and pitch angles which minimize Doppler centroid variation with range and terrain height is derived, and results are shown for residual variation which include the effect of antenna pointing errors. Next the concept of squinted beamwidth is introduced. This is used to show the importance of proper yaw and pitch angles for preserving desirable SAR signal properties and for satisfying SAR imaging constraints. In addition to these contributions, other aspects of high squint are investigated to provide a thorough understanding of squint mode SAR imaging. These include the stop-start assumption, the representation of the platform to scatterer distance, the two-dimensional data spectrum and image spectrum, and the point spread function.

#### 4.2 Doppler Centroid Variation

##### 4.2.1 Squint Angle Derivation

Squint is achieved with yaw and pitch rotations of the antenna from the broadside position, where the yaw angle includes the contributions from both antenna pointing and the equivalent yaw due to earth rotation [25]. The resulting squint angle also depends on the elevation angle

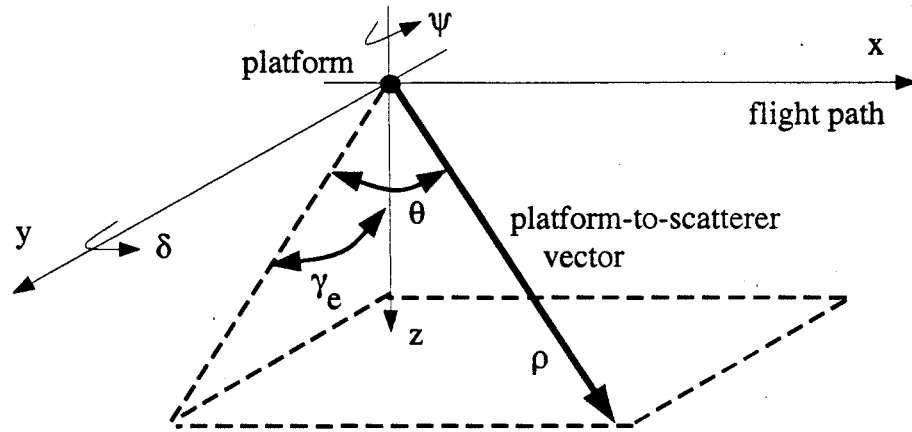


Figure 4.9: Coordinate system showing elevation and squint of vector pointing from antenna to scatterer.

to the scatterer within the beam. This elevation angle in turn is related to the closest approach range and the height of the scatterer. Thus, the Doppler centroid, which is proportional to the sine of the squint angle, varies with closest approach range and terrain height [53]. Variation of the Doppler centroid with range causes problems for SAR processing in the two dimensional frequency domain, as was noted in the previous chapter. In addition, Doppler centroid variation with terrain height can lead to undersampling of the azimuth signal and azimuth ambiguities.

The characterization of Doppler centroid variations requires an expression for the squint angle as a function of yaw, pitch, and elevation. Previous derivations of the squint angle have used small angle approximations appropriate for the small yaw and pitch angles encountered in conventional SAR [54, 55]. However, for squint mode, a general expression for the squint angle is required. To find this, first define a coordinate system for describing the vector which points from the antenna to a scatterer, as shown in Figure 4.9. In this figure, let the  $x$  axis be parallel to the flight vector, the  $z$  axis point to nadir, and the  $y$  axis point in the orthogonal cross track direction. Then the elevation angle,  $\gamma_e$ , and the squint angle,  $\theta$ , form two coordinates of a spherical coordinate system, the third coordinate being  $\rho$ , the vector length. The conversion

between this coordinate system and the rectangular one is given by the equations:

$$\begin{aligned}
 x &= \rho \sin(\theta) \\
 y &= \rho \cos(\theta) \sin(\gamma_e) \\
 z &= \rho \cos(\theta) \cos(\gamma_e) \\
 \rho &= \sqrt{x^2 + y^2 + z^2} \\
 \theta &= \arcsin\left(\frac{x}{\sqrt{x^2 + y^2 + z^2}}\right) \\
 \gamma_e &= \arctan\left(\frac{y}{z}\right).
 \end{aligned} \tag{4.97}$$

Since squint can at most be ninety degrees forward or backward,  $\theta$  satisfies the condition:

$$-\pi/2 < \theta < \pi/2, \tag{4.98}$$

and since the elevation angle is between nadir and horizontal,  $\gamma_e$  satisfies:

$$0 < \gamma_e < \pi/2. \tag{4.99}$$

Yaw refers to a rotation about the  $z$  axis, and pitch is a rotation about the  $y$  axis. To find the squint angle resulting from a yaw and pitch of the antenna, start with a vector pointing broadside, so that  $\theta = 0$ , at an initial elevation angle of  $\gamma_i$ . The initial coordinates in the rectangular system are:

$$\mathbf{x}_0 = \begin{bmatrix} x_0 \\ y_0 \\ z_0 \end{bmatrix} = \begin{bmatrix} 0 \\ \rho \sin(\gamma_i) \\ \rho \cos(\gamma_i) \end{bmatrix}. \tag{4.100}$$

Then, the effect of yaw or pitch can be found by multiplying the initial vector by the appropriate rotation matrix. Letting  $\psi$  donate the yaw angle, the yaw rotation matrix is

$$A_y = \begin{bmatrix} \cos(\psi) & \sin(\psi) & 0 \\ -\sin(\psi) & \cos(\psi) & 0 \\ 0 & 0 & 1 \end{bmatrix}, \tag{4.101}$$

and letting  $\delta$  donate the pitch angle, the pitch rotation matrix is

$$A_p = \begin{bmatrix} \cos(\delta) & 0 & \sin(\delta) \\ 0 & 1 & 0 \\ -\sin(\delta) & 0 & \cos(\delta) \end{bmatrix}. \quad (4.102)$$

Also, the yaw and pitch angles satisfy the conditions:

$$-\pi/2 < \psi < \pi/2, \quad (4.103)$$

and

$$-\pi/2 < \delta < \pi/2. \quad (4.104)$$

Assuming the yaw rotation is performed first and then the pitch, the resulting vector is given by

$$\mathbf{x}_{yp} = A_p A_y \mathbf{x}_\theta. \quad (4.105)$$

Then, by substituting for  $\mathbf{x}_\theta$  from Equation (4.100), and expressing  $\mathbf{x}_{yp}$  in the spherical coordinates defined in Equation (4.97), the squint angle can be expressed in terms of the yaw, pitch, and initial elevation angles as

$$\sin(\theta) = \sin(\gamma_i) \sin(\psi) \cos(\delta) + \cos(\gamma_i) \sin(\delta). \quad (4.106)$$

Also, the final elevation angle of the resulting vector is given by

$$\tan(\gamma_e) = \frac{\tan(\gamma_i) \cos(\psi)}{\cos(\delta) - \tan(\gamma_i) \sin(\psi) \sin(\delta)}. \quad (4.107)$$

Note that for a given yaw and pitch, there is a relationship between the initial and final elevation angles. The initial elevation can be expressed as a function of the final elevation by

$$\tan(\gamma_i) = \frac{\tan(\gamma_e) \cos(\delta)}{\cos(\psi) + \tan(\gamma_e) \sin(\psi) \sin(\delta)}. \quad (4.108)$$

### 4.2.2 Minimization of Doppler Centroid Variation

Given the above formulation for the squint angle, the procedure for steering the antenna to a desired squint angle at a desired elevation angle can be summarized as follows: in the broadside position, tilt the antenna to the initial elevation angle, then apply the yaw rotation, followed by the pitch rotation. From Equation (4.106) it can be seen that the same value of squint can be achieved with many different combinations of yaw and pitch. Because of the problems caused by Doppler centroid variation with range and terrain height, it is desirable to find those values of yaw and pitch which minimize the variation of squint angle. The idea of properly choosing the yaw and pitch angles to minimize the Doppler centroid variation with range was introduced in [24], in which the angles were derived using the slope of the desired iso-Doppler line on a flat surface. However, a more general approach can be taken which involves minimizing the variation of squint with respect to the final elevation angle within the beam. This includes minimization of the Doppler centroid variation with both range and terrain height, and will be shown later to have other beneficial effects on the SAR signal properties in squint mode.

In general, the squint variation is minimized at a particular elevation angle by setting

$$\frac{\partial \sin(\theta)}{\partial \gamma_e} = 0, \quad (4.109)$$

where  $\sin(\theta)$  is defined in Equation (4.106), and the condition on  $\theta$  in Equation (4.98) has been assumed. By making use of the relationship between  $\gamma_e$  and  $\gamma_i$ , and noting that  $\partial \gamma_i / \partial \gamma_e$  is nonzero and finite for the conditions given in Equations (4.103) and (4.104), it can be shown that to minimize squint variation with elevation it is sufficient to satisfy:

$$\frac{\partial \sin(\theta)}{\partial \gamma_i} = 0. \quad (4.110)$$

Then, evaluating Equation (4.110) gives the following relationship between yaw, pitch, and initial elevation for minimizing the variation of squint angle with final elevation:

$$\sin(\psi) = \tan(\gamma_i) \tan(\delta). \quad (4.111)$$

Given a desired squint angle and a desired final elevation angle, the yaw, pitch, and initial elevation angles represent three unknowns in the three Equations of (4.106), (4.107), and (4.111). To simplify the solution, Equation (4.111) can be used to eliminate  $\psi$  from the equations, giving the following two equations in the unknowns of  $\delta$  and  $\gamma_i$ :

$$\sin(\theta) = \frac{\sin(\delta)}{\cos(\gamma_i)} \quad (4.112)$$

$$\tan(\gamma_e) = \frac{\tan(\gamma_i)}{\cos(\delta)\sqrt{1 - \tan^2(\gamma_i)\tan^2(\delta)}} \quad (4.113)$$

These two equations can be solved by Newton's method for solving sets of nonlinear equations [56]. Only a few iterations are required, given a starting guess for the initial elevation angle equal to the desired elevation, and a starting guess for the pitch angle equal to half the desired squint angle. After finding the pitch and initial elevation angles, the required yaw angle is found from Equation (4.111). Finally, assuming the yaw and pitch angles are chosen to satisfy Equation (4.111), an expression for the squint angle which is independent of elevation angle can be found. Substituting for  $\gamma_i$  from Equation (4.111) into the expression for squint in Equation (4.106), and rearranging, gives

$$\cos(\theta) = \cos(\psi)\cos(\delta). \quad (4.114)$$

In the derivation of the optimum yaw and pitch angles to minimize Doppler centroid variation, the derivative of the squint angle was set to zero only at a particular value of elevation angle, corresponding to the middle of the swath and a nominal terrain height. Thus, there is a residual Doppler centroid variation at other elevation angles, leading to a Doppler centroid error at the edges of the range swath and at different terrain heights. In addition, the optimum yaw and pitch angles may not be achieved due to antenna pointing errors, which may increase the residual Doppler centroid errors. To investigate these effects, a relationship between final elevation angle to the scatterer, closest approach range, and terrain height needs to be determined. For a rectilinear geometry, this relationship is simple and depends only on the altitude of the platform. For an orbital geometry and spherical earth, refer to Figure 4.10, where  $H$  is

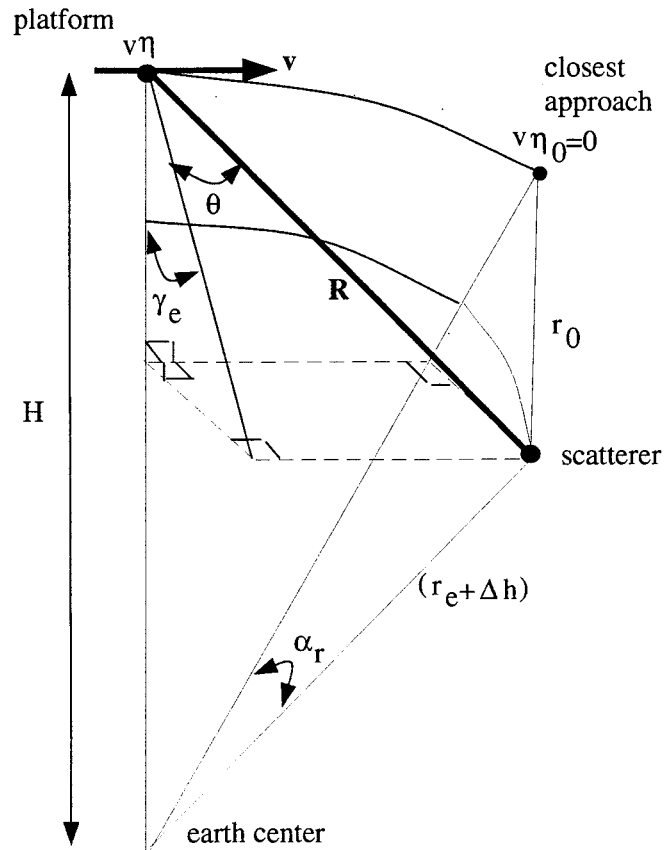


Figure 4.10: Orbital geometry.

the distance of the platform from earth center, and  $\mathbf{v}$  is the velocity of the platform relative to the scatterer. The angle  $\alpha_r$  to the scatterer is measured from the plane containing  $\mathbf{v}$  and earth center. The radius to the scatterer is given by  $(r_e + \Delta h)$  where  $r_e$  is the nominal earth radius and  $\Delta h$  is the terrain height. The final elevation angle to the scatterer within the antenna beam,  $\gamma_e$ , is measured from nadir at the platform location. The closest approach range to the scatterer is measured at the closest approach position. The squint angle to the scatterer is assumed to be measured at the beam center, and  $R(\eta_c; r_0)$  is the distance to the scatterer. The geometry of the figure can be used to find the the following relationship between  $\gamma_e$ ,  $r_0$ ,  $\Delta h$  and  $\theta$  in an orbital geometry:

$$\sin(\gamma_e) = \frac{(r_e + \Delta h) \sin(\alpha_r(r_0, \Delta h))}{R(\eta_c; r_0) \cos(\theta)}. \quad (4.115)$$

parameter	value
altitude	800 <i>km</i>
earth radius	6378 <i>km</i>
platform velocity	7600 <i>m/s</i>
antenna length	10.5 <i>m</i>
pulse length	34 $\mu$ <i>s</i>
pulse bandwidth	20 <i>MHz</i>
wavelength	0.235 <i>m</i> (L-band) 0.056 <i>m</i> (C-band)
oversampling rate	1.2

Table 4.2: Spaceborne SAR parameters.

In this expression, the definition of the angle  $\alpha_r$  is modified from the definition in Equation (2.17) to include the height of the scatterer as follows:

$$\alpha_r(r_0, \Delta h) = \arccos\left[\frac{(r_e + \Delta h)^2 + H^2 - r_0^2}{2(r_e + \Delta h)H}\right]. \quad (4.116)$$

To find the residual Doppler centroid variation for various desired squint angles, the yaw and pitch angles were calculated for an elevation angle at midswath and nominal terrain height, and antenna pointing errors were added. Then, assuming a circular orbit geometry and using Equation (4.115), the elevation angle was calculated at the edges of a 40 *km* swath, and with a terrain height change of  $\Delta h = 1000$  *m*. This was used to find the difference in squint angle from the desired squint angle, which in turn was used to find the residual Doppler centroid error. The parameters used in the calculations are shown in Table 4.2, and were chosen to be representative of spaceborne platforms such as Seasat and ERS-1, with wavelengths corresponding to L-band and C-band, respectively. In addition, to determine how the results are affected by the elevation angle to midswath, cases of near and far incidence are investigated. In the near incidence case, the desired elevation angle is 21°, and for far incidence the desired elevation angle is 40°. Figures 4.11 and 4.12 show the Doppler centroid error, in Hertz, versus squint angle for a spaceborne platform at near and at far incidence. Results are also given for different values of maximum antenna pointing error: zero degree error,  $\pm 0.5$  degree error, and  $\pm 1$  degree error.

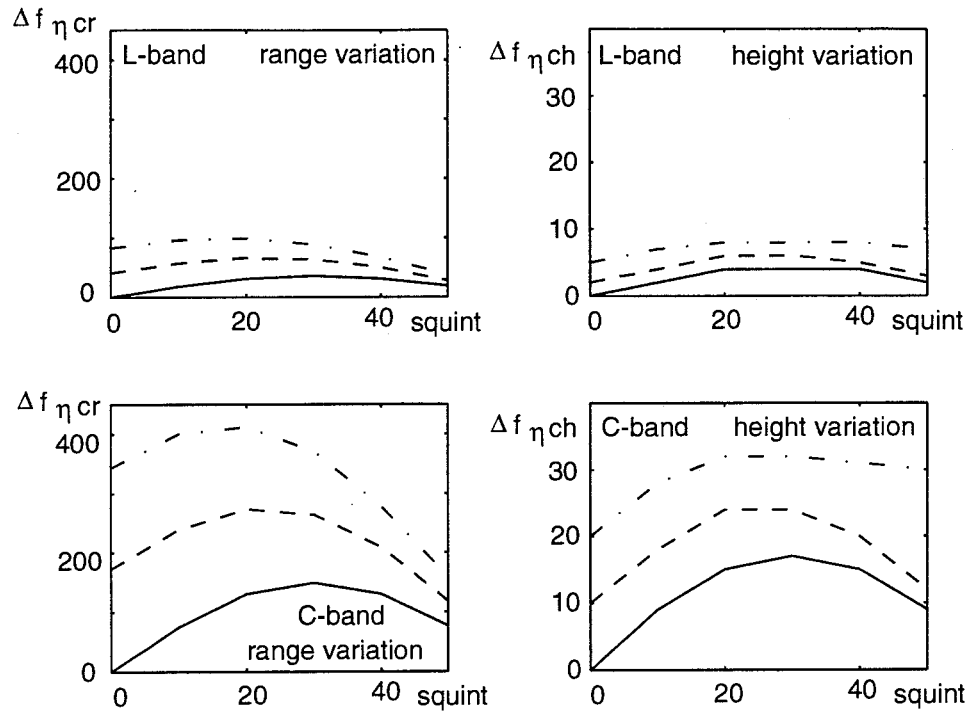


Figure 4.11: Doppler centroid error versus squint, due to range variation and height variation, at near incidence. Solid curve indicates zero degree antenna pointing error, dashed curve indicates  $\pm 0.5$  degree error, and dot-dash curve indicates  $\pm 1$  degree error.

For a given maximum antenna pointing error, the worst case Doppler centroid error is presented.

As can be seen, the proper use of yaw and pitch rotations achieve acceptable Doppler centroid errors. The figures show the Doppler centroid error increasing as the wavelength decreases and as the elevation angle decreases. The effect of an antenna pointing error is to significantly increase the Doppler centroid error, even at zero squint. Variations in Doppler centroid should be small compared to the  $PRF$ , which is typically at least  $1000\text{ Hz}$ . In all cases the effect of terrain height variation on the Doppler centroid is quite small compared to the  $PRF$ , less than 5 percent even with a  $\pm 1$  degree antenna pointing error. At the edge of the

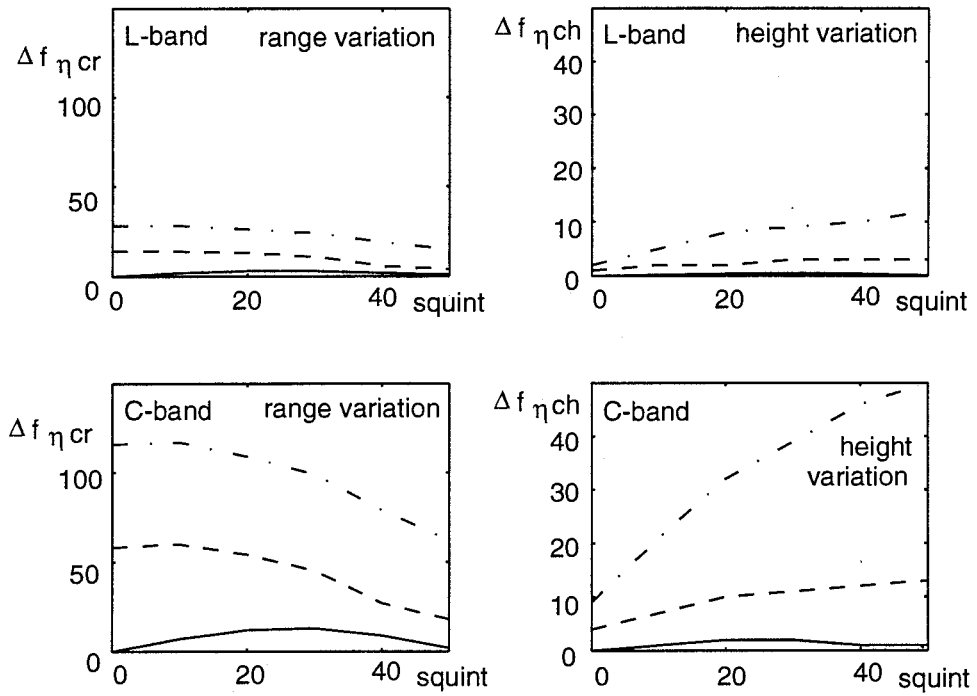


Figure 4.12: Doppler centroid error versus squint, due to range variation and height variation, at far incidence. Solid curve indicates zero degree antenna pointing error, dashed curve indicates  $\pm 0.5$  degree error, and dot-dash curve indicates  $\pm 1$  degree error.

range swath, the Doppler centroid error due to range variation is less than 10 percent of the  $PRF$  in almost all cases, allowing the Doppler centroid variation with range to be neglected in SAR processing. The exception is the case of C-band at near incidence, in which case some accommodation of the range variation of the Doppler centroid would be required in processing. It is interesting to note that for squint angles above about thirty degrees, the sensitivity of the squint angle to elevation angle begins to decrease, resulting in smaller Doppler centroid errors for these values of squint. Finally, it should be noted that because of the dependence on wavelength, the Doppler centroid errors for smaller wavelengths, such as X-band, would be quite large. Thus, processing squint mode SAR data with such wavelengths would be particularly difficult. In addition, for the satellite platforms considered here, the effect of terrain height is small. However, the errors due to terrain height variation would be greater for a spaceborne platform of lower altitude such as a space shuttle.

### 4.3 Signal Properties

#### 4.3.1 Squinted Beamwidth

Signal properties such as azimuth bandwidth and exposure time depend on the change in instantaneous squint angle,  $\theta_s$ , to a scatterer as it passes through the antenna footprint. This change in  $\theta_s$  experienced by a scatterer will be referred to as the squinted beamwidth. At low squint, this is simply the azimuth beamwidth of the antenna in the slant range plane,  $\lambda/L$ . However, at high squint the squinted beamwidth depends on the orientation of the antenna footprint with respect to the platform motion, which in turn depends on the yaw and pitch angles used to achieve the squint.

Given a scatterer at closest approach range  $r_0$ , let the instantaneous squint angle experienced by the scatterer at the leading and trailing edges of the beam be denoted by  $\theta_+$  and  $\theta_-$ , respectively, so the squinted beamwidth is  $\Delta\theta = (\theta_+ - \theta_-)$ . The leading and trailing edges of the beam are determined by pitch and yaw rotations of the zero squint vector, where a yaw rotation of  $\psi + \frac{\Delta\psi}{2}$  produces the leading edge and  $\psi - \frac{\Delta\psi}{2}$  produces the trailing edge. The yaw

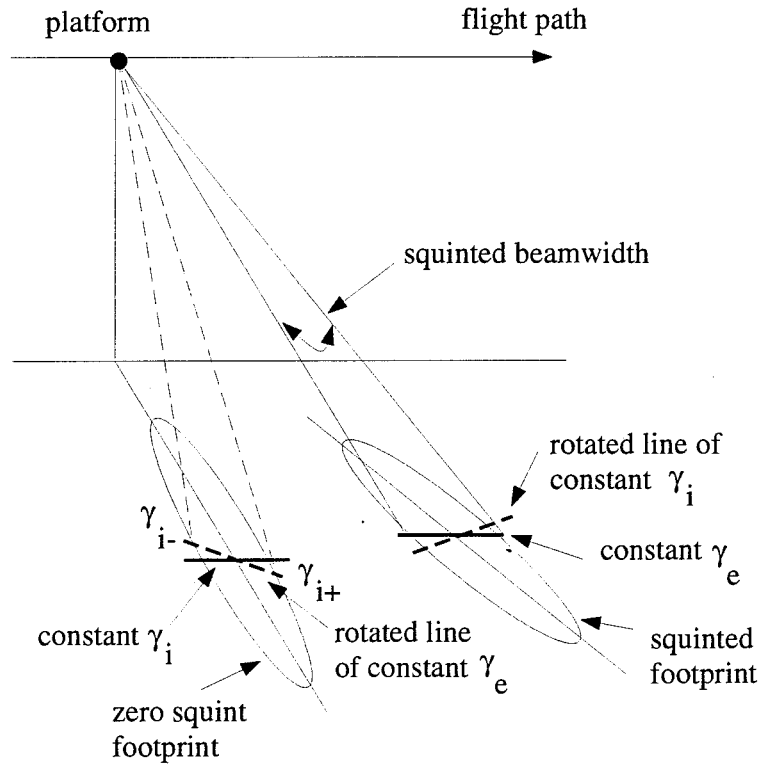


Figure 4.13: Squinted beamwidth. Illustration of elevation angles at beam edges before and after squinting.

interval corresponding to the antenna beamwidth at the initial elevation angle  $\gamma_i$  is given by:

$$\Delta\psi = \frac{\lambda}{L \sin(\gamma_i)}. \quad (4.117)$$

First, consider the rectilinear geometry shown in Figure 4.13. For a scatterer at a fixed closest approach range, the elevation angle remains constant as the scatterer passes through the footprint. Compare the lines of constant elevation through the footprint before and after squinting. The line of constant  $\gamma_i$  shown by the solid line in the zero squint footprint gets rotated to the dashed line in the squinted footprint. Similarly, a line of constant  $\gamma_e$  experienced by the scatterer in the squinted footprint corresponds to the rotated dashed line shown in the zero squint footprint. Thus, the leading and trailing edges of the squinted footprint along the line of constant  $\gamma_e$  correspond to yaw angles of  $\psi \pm \frac{\Delta\psi}{2}$ , and the initial elevation angles of  $\gamma_{i+}$  and  $\gamma_{i-}$  shown in the figure. For a given pitch and yaw rotation, final elevation angle, and yaw

interval,  $\gamma_{i+}$  and  $\gamma_{i-}$  can be found from Equation (4.108) as follows:

$$\tan(\gamma_{i\pm}) = \frac{\tan(\gamma_e) \cos(\delta)}{\cos(\psi \pm \frac{\Delta\psi}{2}) + \tan(\gamma_e) \sin(\psi \pm \frac{\Delta\psi}{2}) \sin(\delta)}. \quad (4.118)$$

From this result, the instantaneous squint angles at the beam edges can be found from

$$\sin(\theta_{\pm}) = \sin(\gamma_{i\pm}) \sin(\psi \pm \frac{\Delta\psi}{2}) \cos(\delta) + \cos(\gamma_{i\pm}) \sin(\delta). \quad (4.119)$$

Since  $\Delta\theta$  is small, an expansion of  $\sin(\theta)$  gives:

$$\Delta\theta = \frac{\sin(\theta_+) - \sin(\theta_-)}{\cos(\theta)}. \quad (4.120)$$

Then, substituting the definition of  $\sin(\theta_{\pm})$  into this equation, and expanding  $\sin(\psi \pm \frac{\Delta\psi}{2})$ , gives

$$\begin{aligned} \Delta\theta &= \frac{(\sin(\gamma_{i+}) - \sin(\gamma_{i-})) \sin(\psi) \cos(\delta) + (\cos(\gamma_{i+}) - \cos(\gamma_{i-})) \sin(\delta)}{\cos(\theta)} \\ &+ \frac{\lambda \cos(\psi) \cos(\delta)}{L \cos(\theta)}. \end{aligned} \quad (4.121)$$

Next, since  $(\gamma_{i+} - \gamma_{i-})$  is small, the above expression for squinted beamwidth can be rearranged to be

$$\Delta\theta = \frac{\partial\theta}{\partial\gamma_i} (\gamma_{i+} - \gamma_{i-}) + \frac{\lambda \cos(\psi) \cos(\delta)}{L \cos(\theta)}. \quad (4.122)$$

If the yaw and pitch angles are chosen to minimize the variation of squint with elevation angle, then the first term in Equation (4.122) is negligible, and from the relationship in Equation (4.114) the expression for squinted beamwidth reduces to

$$\Delta\theta = \frac{\lambda}{L}. \quad (4.123)$$

Thus, if yaw and pitch angles are optimized to minimize the variation of squint with elevation, the squinted beamwidth remains at its zero squint value, independent of squint and elevation angle. From the definition of the azimuth bandwidth of the data in Equation (2.12), the bandwidth for high squint is related to the squinted beamwidth by

$$\Delta f_{\eta} = \frac{2v\Delta\theta \cos(\theta)}{\lambda}. \quad (4.124)$$

By maintaining a constant squinted beamwidth of  $\lambda/L$ , the bandwidth becomes

$$\Delta f_{\eta} = \frac{2v \cos(\theta)}{L}, \quad (4.125)$$

which is independent of range and decreases as the cosine of the squint angle. Thus, proper selection of yaw and pitch angles to align the antenna footprint along an iso-Doppler line not only minimizes Doppler centroid variation, but also preserves the property of SAR imaging that the azimuth bandwidth is independent of range. Also, the dependence of azimuth bandwidth on  $\cos(\theta)$  will prove useful with respect to SAR imaging constraints in the next section.

In an orbital geometry, as seen from Equation (4.115), the relationship between elevation angle and closest approach range depends on the instantaneous squint angle. For this reason, a scatterer at a fixed closest approach range will have slightly different final elevation angles at the leading and trailing edges of the beam, denoted by  $\gamma_{e+}$  and  $\gamma_{e-}$ . However, the same method of determining the squinted beamwidth described above can be used, where  $\gamma_{e+}$  and  $\gamma_{e-}$  are used to calculate  $\gamma_{i+}$  and  $\gamma_{i-}$ , respectively. The only complication is that, since  $\gamma_{e+}$  and  $\gamma_{e-}$  depend on the instantaneous squint angles at the beam edges, an initial guess for  $\Delta\theta$  is required that is refined by iteration. Nevertheless, when these calculations were performed with the yaw and pitch angles chosen to minimize the squint variation with elevation, the value of squinted beamwidth was still found to be equal to  $\lambda/L$ , so that the effect of an orbital geometry on the squinted beamwidth in this case is negligible.

To illustrate the effect of the use of optimal yaw and pitch angles on the azimuth bandwidth, Table 4.3 shows the azimuth bandwidth as a function of squint angle for various cases. First, the bandwidth was calculated by assuming that only a yaw rotation was assumed to achieve the squint. Results are given for near and far incidence cases, corresponding to different ranges for the same platform altitude, and the parameters of Table 4.2 were used in the calculations. As can be seen, for the same squint angle the difference in bandwidth between near and far incidence cases is significant. In contrast, the table also shows the bandwidth when yaw and pitch angles are optimized to minimize the variation of squint with elevation. In this case, the results for the near and far incidence cases were the same, and agreed with the expression for

squint (degrees)	azimuth bandwidth (Hz)		
	yaw only		yaw and pitch
	near incidence	far incidence	
0	1448	1448	1448
10	1559	1450	1426
20	1791	1443	1360
30	1969	1407	1254
40	1958	1248	1109
50	1640	934	931

Table 4.3: Azimuth bandwidth versus squint: Yaw rotation only; and with optimal yaw and pitch.

bandwidth in Equation (4.125).

Finally, the squinted beamwidth determines the exposure time of the scatterer. To find a relationship between squinted beamwidth and exposure time, first use the definition of instantaneous azimuth-frequency with Equation (2.12) to determine a relationship between instantaneous squint angle and azimuth-time:

$$\sin(\theta_s(\eta)) = \frac{-1}{v} R'(\eta). \quad (4.126)$$

At the beam center, this equation gives the relationship between squint angle and beam center offset time. For narrow beams, the relationship between instantaneous squint angle and azimuth-time at the beam edges can be found by expanding both sides of Equation (4.126). Rearranging the result gives the relationship between exposure time and squinted beamwidth:

$$\Delta\eta = \frac{v \cos(\theta) \Delta\theta}{|R''(\eta_c)|}. \quad (4.127)$$

### 4.3.2 SAR Signal Constraints

A fundamental constraint in SAR concerns the relationship between the range swath and the azimuth sampling rate [12, 13]. This is illustrated in Figure 4.14, which shows how a received echo which must fit into the time between the transmission of adjacent pulses. In this figure,  $2\Delta R/c$  is the difference between the largest and smallest possible travel times to scatterers

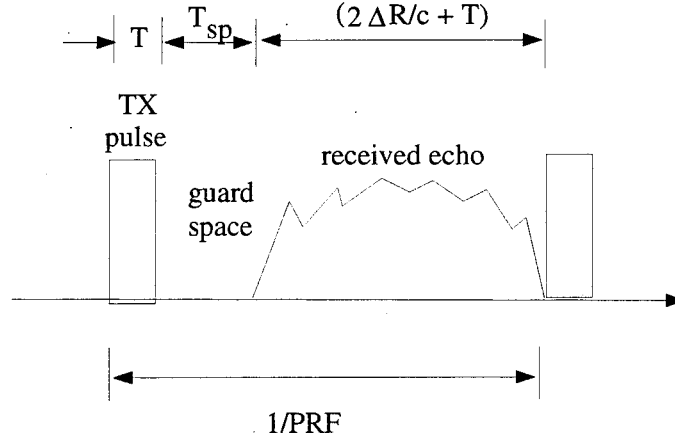


Figure 4.14: Transmitted pulses and received echo.

within the beam. At a given azimuth-time, assuming a forward squint angle, the largest distance corresponds to a scatterer at far range and at the leading edge of the beam, while the smallest distance corresponds to a scatterer at near range at the trailing edge of the beam. For example, let  $r_{ref}$  be the closest approach range at midswath so that  $r_{ref} + \Delta r/2$  and  $r_{ref} - \Delta r/2$  are the closest approach ranges at the near and far ends of the swath. Then, the interval of possible distances to scatterers is

$$\Delta R = R(\eta_c + \Delta\eta/2; r_{ref} + \Delta r/2) - R(\eta_c - \Delta\eta/2; r_{ref} - \Delta r/2). \quad (4.128)$$

After convolution of the scatterers in the swath with the transmitted pulse, the length of the received echo is  $(2\Delta R/c + T)$  as shown in the figure. In addition, a guard space,  $T_{sp}$ , is included to allow for variations in the range delay of the signal and to allow some flexibility in choosing the  $PRF$ . From the figure, it can then be seen that the constraint that must be satisfied by the received signal and the  $PRF$  is:

$$\frac{2\Delta R}{c} + 2T + T_{sp} < \frac{1}{PRF}, \quad (4.129)$$

where the  $PRF$  is equal to the azimuth bandwidth multiplied by the oversampling rate,  $o_s$ . In general, since the  $PRF$  decreases with antenna length, and the range swath decreases with antenna width, this constraint leads to a minimum size for the antenna [12].

The effect of a high squint angle on this constraint should be investigated. In general, for a given closest approach range swath,  $\Delta r$ , the length of the received echo increases with squint. This is due to the fact that when the swath is viewed at an angle other than perpendicular to the flight path, the perceived distance between the near and far ends of the swath increases. In addition, increasing the squint angle increases the amount of range migration. However, if yaw and pitch angles are chosen such that the azimuth bandwidth is given by Equation (4.125), then the *PRF* can be allowed to decrease as the cosine of the squint angle, allowing a greater time between pulses. To describe the effect of squint on the condition in Equation (4.129), consider a rectilinear geometry. In this case,  $\Delta R$  can be expressed approximately as

$$\Delta R \approx \frac{\Delta r}{\cos(\theta)} + \frac{\lambda r_{ref} \tan(\theta)}{L \cos(\theta)}, \quad (4.130)$$

where the first term is due to the viewing angle and the second term is due to range migration. Substituting this expression into Equation (4.129) and using the expression for azimuth bandwidth in Equation (4.125), the maximum closest approach range swath that can be imaged for a given squint angle can be derived:

$$\begin{aligned} \Delta r < & \left[ \frac{cL}{4v\sigma_s} - \frac{c}{2}(2T + T_{sp}) \right] \\ & + \left[ \frac{c}{2}(2T + T_{sp})(1 - \cos(\theta)) - \frac{\lambda r_{ref}}{L} \tan(\theta) \right]. \end{aligned} \quad (4.131)$$

In this expression the first term gives the constraint at zero squint, and the second term shows how it changes as squint increases.

For an orbital geometry, the appropriate distance equation  $R(\eta; r_0)$  can be used in the calculation of  $\Delta R$  in Equation (4.128). Then, for a given squint angle, the maximum value of closest approach range swath,  $\Delta r$ , for which the condition in Equation (4.129) is satisfied can be found. The results are shown in Figure 4.15, for L-band and C-band, and for near and far incidence, where the parameters of Table 4.2 were used in the calculations. The value of the guard space,  $T_{sp}$ , was near that of Seasat,  $T_{sp} = 200\mu s$ . Also, results are shown for antenna lengths of 10.5 m and 12 m in order to indicate the effect of antenna length on the constraint. Given a desired swath width, it can be seen from the figures that the SAR imaging

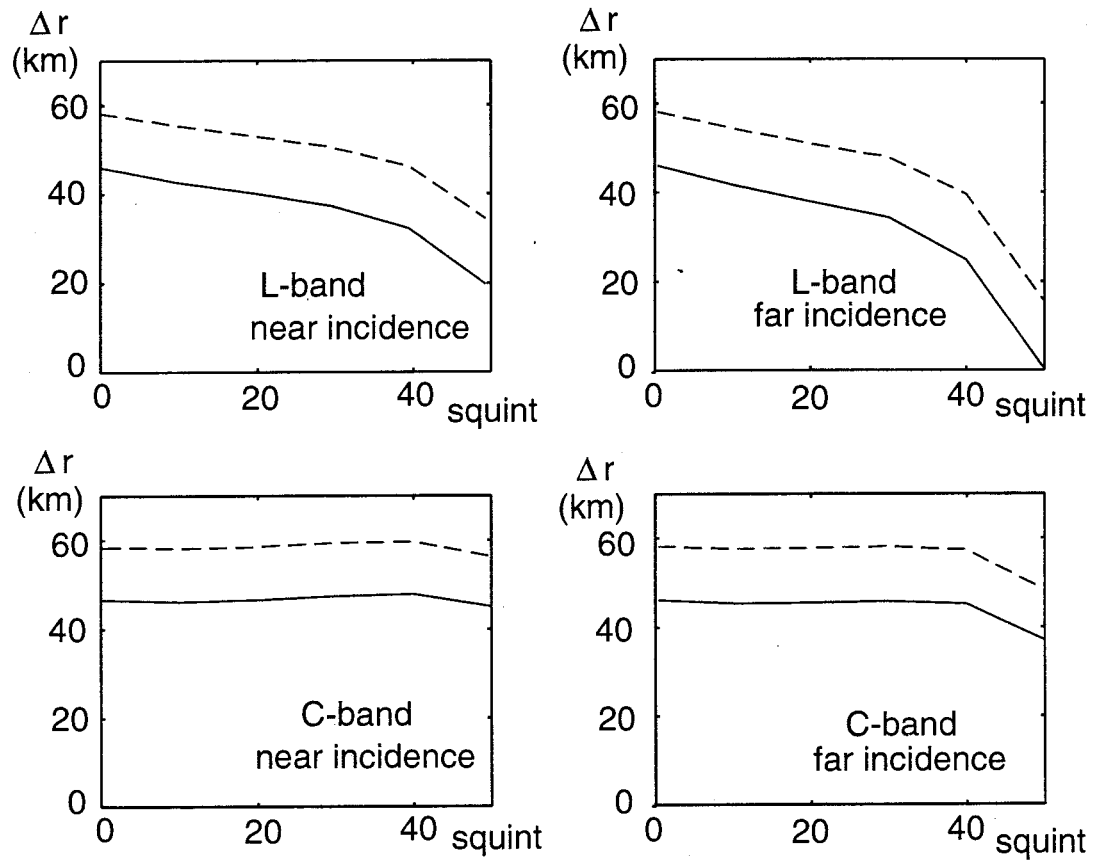


Figure 4.15: Closest approach range swath versus squint for L-band and C-band and for near and far incidence.  $T_{sp} = 200\mu s$ . Solid lines: antenna length  $L = 10.5m$ . Dashed lines: antenna length  $L = 12m$ .

constraint forms fundamental limitation on the squint angle for the given wavelength. A larger wavelength increases the aperture, thus allowing more range migration, making the constraint in Equation (4.128) more difficult to satisfy for the same range swath. For L-band the range swath decreases rapidly for squint angles above 35 degrees, whereas for C-band the swath begins to drop after about 50 degrees of squint.

#### 4.4 Stop-Start Assumption

In modelling the SAR signal, it is assumed that the platform is stationary while a pulse is transmitted and received. This assumption ignores the distance travelled by the platform between the transmission and reception of the pulse, and the fact that the platform is moving during the transmission and reception of the pulse. These approximations have a negligible effect on the signal for small squint angles, but may become noticeable at high squint [16, 57]. Thus, in squint mode SAR, it is necessary to know the effects of the stop-start assumption on the signal, so that they can be correctly accounted for during processing.

First, consider the distance travelled by the platform between the transmission and reception of the leading edge of the pulse. This effectively changes the length of the path travelled by a pulse, so that it is no longer simply twice the distance from the platform to the scatterer at one particular azimuth time. Figure 4.16 illustrates the actual path of the pulse between transmission and reception. Assume that the position of the platform at azimuth time  $\eta$  corresponds to the position at the leading edge of the transmitted pulse. Then the distance to the scatterer on the transmit path is the same as the platform to scatterer distance used above,  $R(\eta, r_0)$ . Let the distance from the scatterer to the receive position be denoted by  $R_R$ . Also, the figure shows the part of the flight path between the transmission and reception of the pulse, where the platform has travelled a distance of  $v(R(\eta; r_0) + R_R)/c$ . Since this distance is relatively small, assume that the flight path follows a straight line in the direction of the velocity vector at azimuth time  $\eta$ . Finally, the angle from broadside to the scatterer is the instantaneous squint angle,  $\theta_s(\eta)$ . With these definitions, the geometry of the figure can be used to show that the

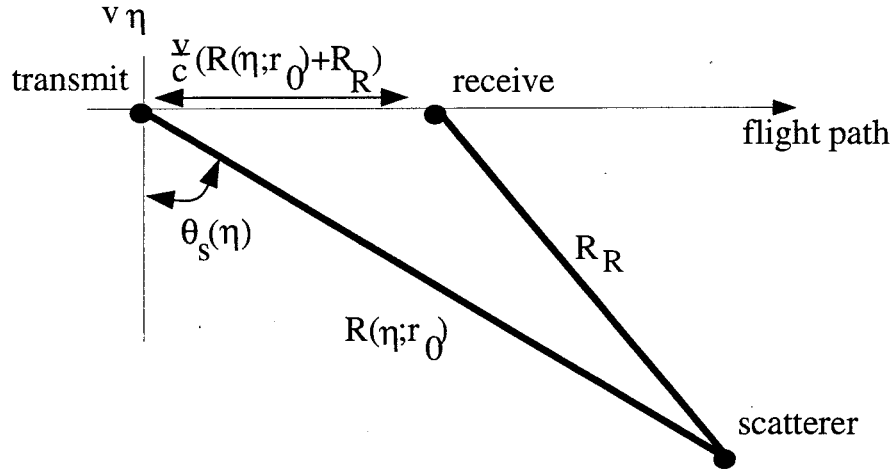


Figure 4.16: Path travelled by pulse without stop-start assumption.

length of the path travelled by the pulse,  $2R_p = (R + R_R)$ , is

$$2R_p(\eta; r_0) = 2R(\eta; r_0) \left[ \frac{1 - \frac{v}{c} \sin(\theta_s(\eta))}{1 - \left(\frac{v}{c}\right)^2} \right]. \quad (4.132)$$

Note that  $R_p(\eta; r_0)$  can be considered as a modified platform to scatterer distance, that can be used when modelling the SAR point scatterer response as a function of azimuth-time.

Recall from Equation (2.11) that the Doppler centroid of the point scatterer response was found by taking the derivative of the azimuth phase of the signal, when the scatterer was at the beam center. Since the azimuth phase is proportional to the path length, an accurate representation of the Doppler centroid as a function of squint angle should use the path length in Equation (4.132). Neglecting the very small factor of  $\left(\frac{v}{c}\right)^2$ , and assuming a circular orbit geometry, this gives a Doppler centroid of

$$f_{\eta c} = \frac{2v \sin(\theta)}{\lambda} - \frac{2v^2 \sqrt{r_c^2 \cos^2(\alpha_r) - R^2 \sin^2(\theta)}}{c\lambda H}. \quad (4.133)$$

The second term in this expression gives the change in Doppler centroid due to platform motion. However, even for small wavelengths this term is at most a few Hertz, which is negligible.

Now consider the effect of the platform motion within the duration of the pulse itself. Let  $\tau$  be the 'fast-time' time within the pulse, starting at the leading of the pulse when it is

transmitted at azimuth-time  $\eta$ . To find the effect of platform motion during transmission and reception of the pulse, it is necessary to represent the instantaneous distance from the platform to the scatterer as a function of  $\tau$ . To do this, the above derivation of the path length can be applied to a point within the transmitted pulse, delayed from the leading edge by an amount  $\tau$ . Then, the instantaneous platform to scatterer distance can be modelled as  $R_p(\eta + \tau; r_0)$ . This can be used in the expression for the received echo from a point scatterer:

$$p\left(\tau - \frac{2R_p(\eta + \tau)}{c}\right) \exp\left[\frac{-j4\pi f_0 R_p(\eta + \tau)}{c}\right]. \quad (4.134)$$

Thus, the effect of the platform motion is a time dependent delay in the complex envelope of the pulse,  $p(\tau)$ , and in the phase of the carrier. This is the same problem that has been investigated for nonimaging radar with respect to the returns from moving targets [11]. To investigate the effect on the signal, the time dependent distance can be expanded in a series:

$$R_p(\eta + \tau; r_0) = R_p(\eta; r_0) + R'_p(\eta; r_0)\tau + R''_p(\eta; r_0)\tau^2, \quad (4.135)$$

with terms corresponding to the instantaneous range (constant delay), range rate (linear in  $\tau$ ), and range acceleration (quadratic in  $\tau$ ). The effect of the range rate and higher terms on the complex envelope,  $p(\tau)$ , is negligible. For example, for spaceborne SAR parameters and high squint angles, including the range rate term in the argument of  $p(\tau)$  results in a change in the frequency rate of a linear FM pulse of less than 0.01 percent. Furthermore, considering the effect of the time dependent delay on the carrier phase, the change in frequency rate due to the range acceleration term is very small compared to the frequency rate of the pulse. Thus, the only noticeable effect of platform motion during pulse transmission and reception is the range rate term in the carrier phase, which is simply a Doppler shift of the individual pulse.

The ability of a matched filter radar to measure the Doppler shift of a single pulse depends on the length of the transmitted pulse [11]. In general, the Doppler resolution of a pulse is roughly equal to the inverse of the pulse length, so for the pulses used in spaceborne SAR the Doppler resolution of a pulse is about  $30 \text{ kHz}$ . Thus, Doppler shifts that are much less than this will not significantly affect the received SAR signal. By substituting the range rate term

into the carrier phase, the Doppler shift of a pulse can be shown to be  $2R'_p(\eta; r_0)/\lambda$ . Note that this is the same as the expression for the instantaneous azimuth-frequency corresponding to the azimuth-time  $\eta$ . That is, the values of Doppler shifts of pulses received from different points across the aperture span the interval of azimuth-frequencies in the SAR signal. For low squint, the Doppler shifts are much smaller than the Doppler resolution of a pulse, and the Doppler shifts can be neglected. For high squint, where the Doppler centroid can be on the order of  $100 \text{ kHz}$ , the effect of the Doppler shifts is noticeable. However, if the received signal is frequency-shifted in range to remove the Doppler shift corresponding to the center of the beam, then only the variation of Doppler shifts across the aperture is important. This is equal to the azimuth bandwidth, which is much less than the Doppler resolution of a single pulse. Also, if the variation of the Doppler centroid with range is minimized, then the Doppler shifts of received pulse will not vary significantly with the closest approach range of the scatterers. Thus, the effect of high squint on individual pulses can be accommodated by a constant, range-frequency shift of the received signals.

#### 4.5 Signal Model for SAR Processing

As mentioned in Chapter 2, satellite orbit information is used to determine an equation for the platform to scatterer distance,  $R(\eta; r_0)$ . (If the platform motion between pulse transmission and reception is taken into account, the modified distance equation that was described in the previous section,  $R_p(\eta; r_0)$ , is used.) Also, it is desirable to have a relatively simple model for the distance equation in the point scatterer response. In this section, an approach for using the hyperbolic model of the distance equation for the case of high squint is discussed.

First, it should be noted that while an equation for  $R(\eta; r_0)$  is available as a function of  $\eta$  and  $r_0$ , it is still necessary to determine the values of closest approach range and beam center offset time,  $\eta_c$ , that correspond to each range bin in the data. Given the range gate delay to the first sample the received echo, and the number of samples to a given range bin, the travel time along the beam center to the scatterer in that range bin can be found. Let this value be

denoted by  $\tau_{\eta_c}$ , which is equal to  $2R(\eta_c; r_0)/c$ . Also, the Doppler centroid can be related to the derivative of  $R(\eta; r_0)$ , as shown in Equation (2.11). Now, treating  $r_0$  and  $\eta_c$  as variables, the measured values of  $\tau_{\eta_c}$  and  $f_{\eta_c}$  can be used in the equations:

$$\begin{aligned}\frac{c\tau_{\eta_c}}{2} &= R(\eta_c; r_0) \\ \frac{-\lambda f_{\eta_c}}{2} &= R'(\eta_c; r_0)\end{aligned}\quad (4.136)$$

to solve for closest approach range and beam center time for the given range bin [58].

The approach to modelling  $R(\eta; r_0)$  that was described in Chapter 2 involved fitting a hyperbolic function to the distance equation at the closest approach azimuth time. This gives a very good approximation to the distance equation for small to moderate squint angles where the equation is evaluated near the closest approach azimuth-time. However, at high squint the hyperbolic equation that is fit at the closet approach time diverges from the actual distance equation, as shown in Figure 4.17. The difference between the hyperbolic and the actual equations over the aperture results in significant errors in phase, registration, range migration correction, and focussing [33].

However, a hyperbolic model of the distance equation is particularly convenient to work with. It provides an understanding of the imaging process by analogy with the wave-equation methods. Also, it results in a convenient derivation of the chirp scaling algorithm. To use a hyperbolic model of the distance equation at high squint, it has been proposed in [33] that a hyperbolic equation can be fit to the distance equation at the beam center time, as shown in Figure 4.17. That is, the distance equation is approximated over the aperture by

$$R(\eta - \eta_0; r_0) \approx \sqrt{r_h^2 + B(\eta - \eta_0 - \eta_h)^2}, \quad (4.137)$$

where  $r_h$ ,  $B$ , and  $\eta_h$  are range dependent parameters that are determined from the actual distance equation as follows: Let

$$\mathcal{R}(\eta - \eta_0; r_0) = R^2(\eta - \eta_0; r_0) \quad (4.138)$$

denote the square of the actual distance equation. The parameters are then found by equating  $\mathcal{R}$  and its first and second derivatives, evaluated at the beam center time, to the corresponding

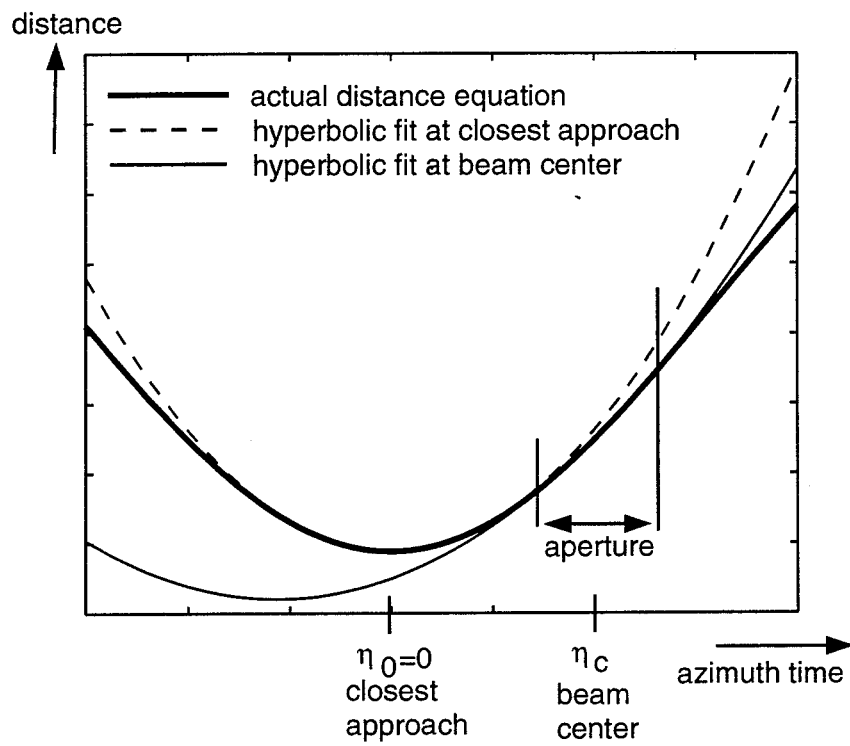


Figure 4.17: Illustration of actual distance equation, hyperbolic fit at closest approach time, and hyperbolic fit at beam center.

values for  $(r_h^2 + B(\eta - \eta_h - \eta_0)^2)$ . This gives the following expressions:

$$\begin{aligned} r_h &= \sqrt{\mathcal{R}(\eta_c; r_0) - \frac{(\mathcal{R}'(\eta_c; r_0))^2}{2\mathcal{R}''(\eta_c; r_0)}} \\ \eta_h &= \eta_c - \frac{\mathcal{R}'(\eta_c; r_0)}{\mathcal{R}''(\eta_c; r_0)} \\ B &= \mathcal{R}''(\eta_c; r_0)/2. \end{aligned} \quad (4.139)$$

Note that in representing the distance equation by Equation (4.137),  $r_h$  and  $(\eta_0 + \eta_h)$  become the effective ‘closest approach range’ and ‘closest approach azimuth time’, respectively, of the hyperbola. The point scatterer response can then be written with  $r_h$  as the closest approach range variable and  $(\eta_0 + \eta_h)$  as the azimuth position. The Doppler centroid of the signal is unchanged in the model since the slope of the distance equation is matched by the model at the beam center. Processing then proceeds with the hyperbolic model, as described in Chapter 3. For example, if the chirp scaling algorithm is used, the range position of the point spread function after processing is

$$\tau_d(f_{\eta r}; r_h(r_0)) = \frac{2r_h}{c\gamma(f_{\eta r}; r_h)}. \quad (4.140)$$

The correction of the point spread function’s azimuth position from  $(\eta_0 + \eta_h)$  to  $\eta_0$  can be done by including an appropriate linear phase term in azimuth frequency, during the azimuth compression step in the range-Doppler domain. In the range direction, the fact that the point spread function is registered in the  $r_h$  variable can be taken into account, along with the dependence of the registration on  $f_{\eta r}$ , during image resampling to ground coordinates. To determine the accuracy of the hyperbolic fit to the distance equation over the aperture, Table 4.4 gives the resulting maximum azimuth phase error at the edge of the aperture as a function of squint angle. Near and far incidence cases are presented with results for L-band and C-band. As can be seen, the fit to the distance equation is sufficiently accurate for L-band up to about 40 degrees of squint, and for C-band up to 50 degrees.

squint	phase error (degrees)			
	near incidence		far incidence	
	L-band	C-band	L-band	C-band
0	0.0	0.0	0.0	0.0
10	0.5	0.0	1.0	0.1
20	1.3	0.1	2.7	0.2
30	3.5	0.2	6.2	0.4
40	12.3	0.7	30.7	1.8
50	79.7	4.6	340.0	19.8

Table 4.4: Maximum azimuth phase error at the edge of the aperture for hyperbolic fit to distance equation at beam center time.

## 4.6 Spectrum and Point Spread Function

In Chapter 2, the amplitude spectrum and the point spread function of the processed image were briefly described for small squint. For all but small squint angles, however, a description of the spectrum requires a distinction between the data spectrum and the image spectrum. This distinction is made explicitly in the wave equation approach to SAR processing, discussed in Chapter 3. The dimensions of the raw SAR data are azimuth position and pulse travel time, while in the processed image, the dimensions are azimuth position and range position. After matching the phase of the SAR transfer function at a reference range, the Stolt algorithm processes data by interpolating from the data frequency variables to those of the image. Thus, it is the range variance of processing that maps the data spectrum to the image spectrum.

### 4.6.1 Data Spectrum

At high squint, the two dimensional region of support of the data spectrum poses an interesting problem, which arises from the dependence of the Doppler centroid on range frequency,  $f_r$ . To see this, note that the Doppler centroid in Equation (2.13) was defined at the carrier frequency. In the two dimensional frequency domain, however, the Doppler centroid can be determined

for each range-frequency component as [30]

$$f_{\eta c} = \frac{2v(f_0 + f_r) \sin(\theta)}{c}. \quad (4.141)$$

This results in a skewed region of support of the data spectrum, as shown in Figure 4.18. Also, because of the sampling of the azimuth signal, this skew can cause parts of the spectrum to cross into the adjacent *PRF* band. Note that since all the repeated spectra are skewed the same way, there is no actual aliasing of signal energy at this point. However, after range cell migration correction and inverse transformation to the range-Doppler domain, the signal energy from the repeated spectra are all aligned in the same range bin, and the corrected trajectories interfere with each other. This results in aliasing in azimuth-frequency, and prevents the application of the azimuth compression filter over all the azimuth frequencies in the signal. Finally, the *PRF* cannot generally be increased enough to alleviate this problem, because of the SAR imaging constraints discussed earlier. Thus, while the SAR data can be collected with an azimuth sampling rate that decreases with squint angle, the processing of the data into an image requires extra azimuth bandwidth to avoid aliasing. Note that this problem occurs for any SAR processing algorithm, since the potential for aliasing is inherent in the signal.

This problem can be accommodated during processing by replicating the parts of the spectrum that overlap, as illustrated in Figure 4.19. This produces a two dimensional spectrum without overlap, removing the potential for aliasing during processing. Essentially, the azimuth bandwidth is expanded to accommodate the nature of the squinted SAR signal. Also, this replication of range lines can be done in the range-Doppler domain, before the range Fourier transform. This allows all processing steps that depend on azimuth-frequency, such as chirp scaling, to be performed correctly for all azimuth-frequencies in the signal. Then, the unwanted pieces of duplicated spectrum, shown in the figure, can be removed in the two dimensional frequency domain by applying a window.

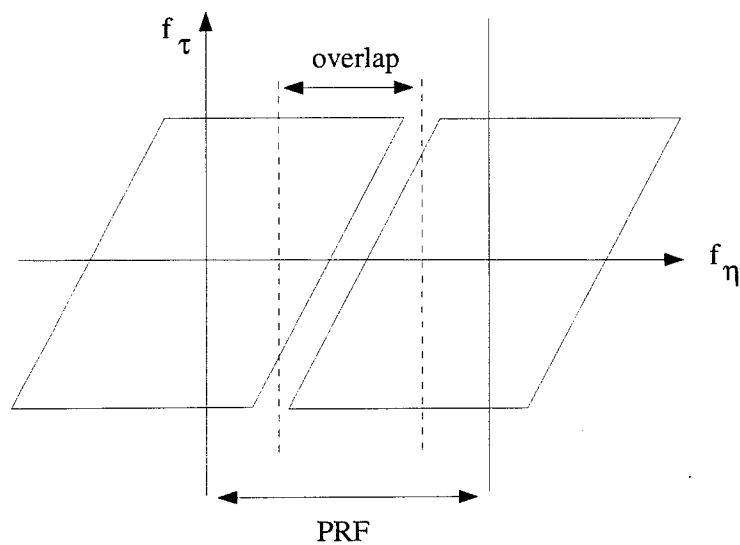


Figure 4.18: Skewed region of support of data spectrum.

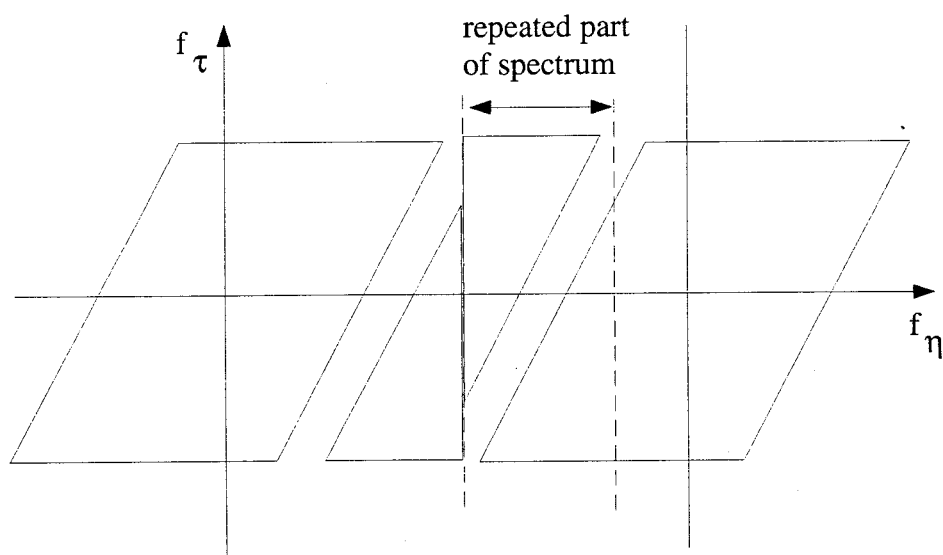


Figure 4.19: Replication of parts of spectrum to expand azimuth bandwidth.

### 4.6.2 Image Spectrum

As mentioned, range variant processing maps the data spectrum to the image spectrum, as indicated by the Stolt change of frequency variables in Equation (3.78). To give an illustration of the image spectrum, consider the spectrum for a portion of the image that is small enough that the  $B$  parameter can be considered constant in range, so that the change of frequency variables in Equation (3.78) applies. The region of support of the image spectrum can then be derived by combining the  $f_\tau$  dependence of the Doppler centroid with the change of frequency variables. First, in the two dimensional frequency domain, azimuth-frequency can be related to instantaneous squint angle as follows:

$$f_\eta = \frac{2v(f_0 + f_\tau) \sin(\theta_s)}{c}. \quad (4.142)$$

Then, by substituting this expression for  $f_\eta$ , the Stolt change of frequency variables can be expressed as

$$(f_0 + f_t) = (f_0 + f_\tau) \sqrt{1 - \frac{v^2}{B} \sin^2(\theta_s)}. \quad (4.143)$$

This gives the mapping from the data spectrum to the image spectrum, as a function of  $\theta_s$ , as illustrated in Figure 4.20. Since the pulse bandwidth and the beamwidth do not change with squint, the image spectrum for a high squint angle can be obtained from the zero squint spectrum by rotating it along the arc shown in the figure. This representation of the image spectrum agrees with the polar representation derived using the tomographic approach to spotlight SAR imaging [21, 22, 59].

Thus, the effect of squint is a rotation of the system end-to-end transfer function (from scene to image) in the two dimensional frequency domain. Accordingly, the point spread function for high squint is the rotated *sinc* function shown in Figure 4.20. This means that the range and azimuth resolution widths are approximately the same as for zero squint, but are measured along different directions in the image than in the zero squint case.

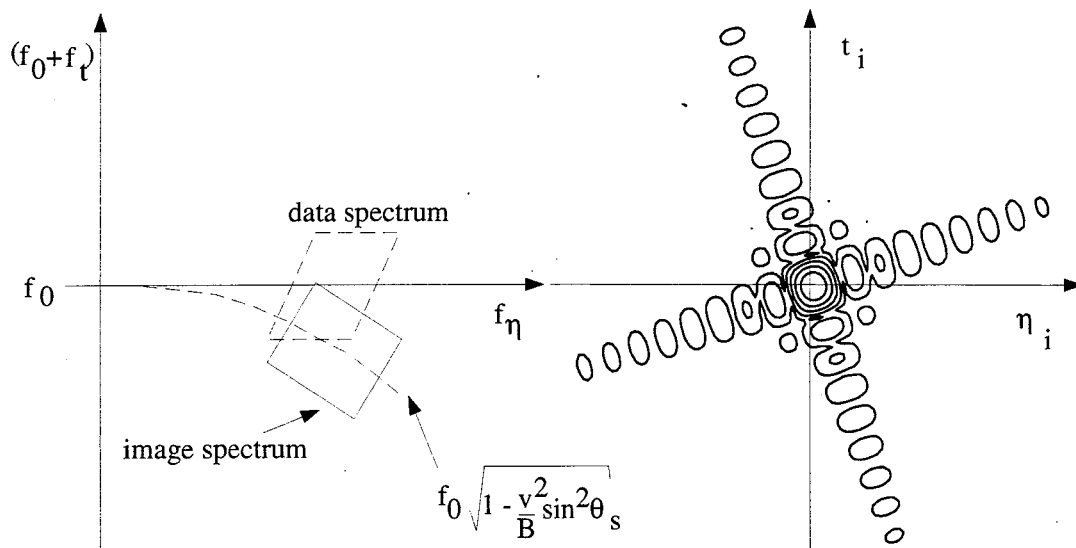


Figure 4.20: Contour plots of image spectrum and point spread function after range variant processing.

## Chapter 5

### Investigation of Chirp Scaling

#### 5.1 Introduction

Chirp scaling is a relatively new algorithm for SAR processing, and several aspects of the algorithm need to be investigated and more fully understood. This includes the image quality that is achieved with the algorithm relative to conventional SAR processors. To this end, a chirp scaling SAR processor was implemented in 'C' on a Sun workstation, and was used to process Seasat data, creating the first images produced with the chirp scaling algorithm. In addition to implementing the algorithm, the assumptions and approximations used in the derivation of the chirp scaling algorithm are investigated, especially for increasing squint angles. Contributions of this chapter include the derivation of the side-effects of the chirp scaling phase function multiply, and the processing errors due to the range dependence of the  $B$  parameter in the signal model and the range dependence of secondary range compression. In addition, the processing error due to a general pulse phase modulation error is derived, in order to determine the effect of such pulse phase errors on chirp scaling.

#### 5.2 Comparison with Range-Doppler

##### 5.2.1 Image Quality At Low Squint

SAR data from the Seasat satellite was processed with the chirp scaling processor, and with a commercial range-Doppler processor called GSAR built by MacDonald Dettwiler. For a given data set, the processing parameters for the chirp scaling processor were obtained from the GSAR run on the same data. Thus, the outputs of the two processors could be compared in

order to determine the image quality performance of the chirp scaling algorithm, relative to that of the range-Doppler algorithm. Data from the Goldstone scene, a mountainous region in California, was processed. The data are conventional SAR data at L-band, and the squint angle is only about one degree, so that the SRC approximations made by the range-Doppler algorithm are not significant. Figures 5.21 and 5.22 show images, 512 samples wide in each direction, of a part of the Goldstone scene, formed with the range-Doppler and chirp scaling algorithms, respectively. The images show the magnitude of the complex reflectivity, averaged by a factor of four in the azimuth direction in order to provide the effect of ‘multilooking’, which is commonly used to reduce speckle [40]. This scene contains an array of corner reflectors, as can be seen on the right side of the images. The corner reflectors provide point scatterers which can be used to analyze the point spread functions corresponding to the different processors. Also present in the scene is a very strong reflector, at the top of the image, which caused some saturation of the SAR system. Visual inspection of the images show no noticeable differences between them, except for the strong scatterer which produces artifacts in the range-Doppler image due to the interpolator used in range migration correction.

Next, portions of the ‘single-look’ complex images around the corner reflectors were extracted in order to examine the point spread functions of the processors. The image portion centered on a particular corner reflector was input to a MATLAB point scatterer analysis program. This program first performed a two-dimensional interpolation to locate the peak of the point spread function and measure the peak phase. Then slices through the peak were taken in the range and azimuth directions, and these were used to measure the 3dB resolution width and the sidelobe level of the point spread function in each direction. As an example, Figures 5.23 to 5.26 show the plots of a point spread function in range and azimuth for the range-Doppler and chirp scaling algorithms, respectively. The results of analyzing six point scatterers in each image are presented in Table 5.5. This gives the average resolution and integrated sidelobe ratio (ISLR) in the range and azimuth directions for the GSAR and chirp scaling processors. ISLR is the ratio of the total power in the sidelobes to the power in the main lobe of the slice of the

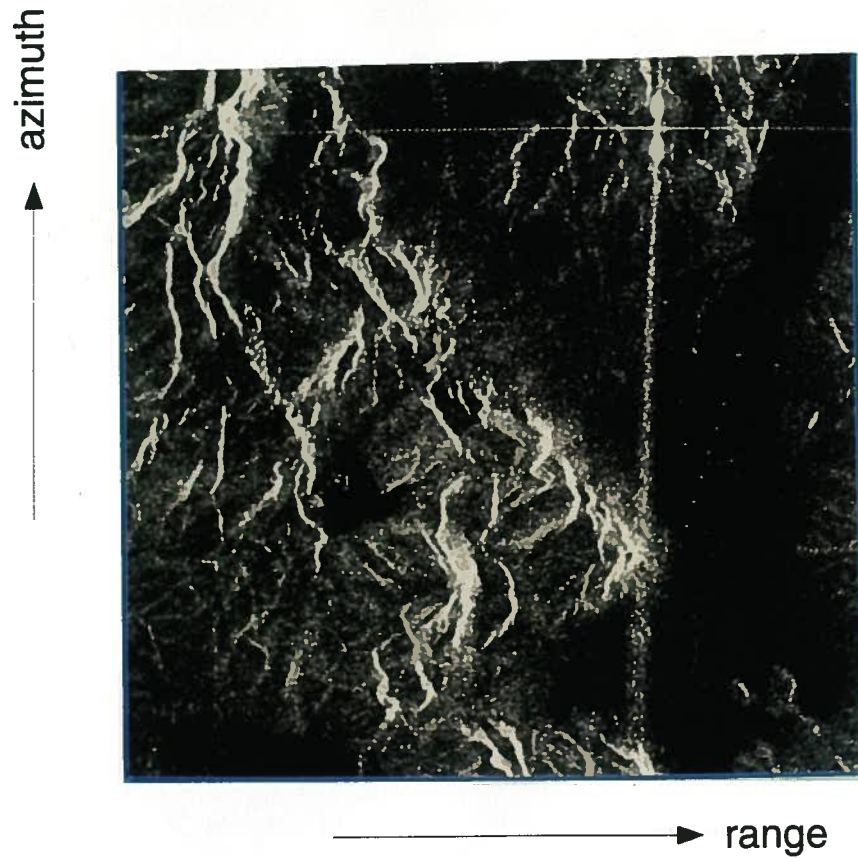


Figure 5.21: Seasat Goldstone scene processed with range-Doppler algorithm.

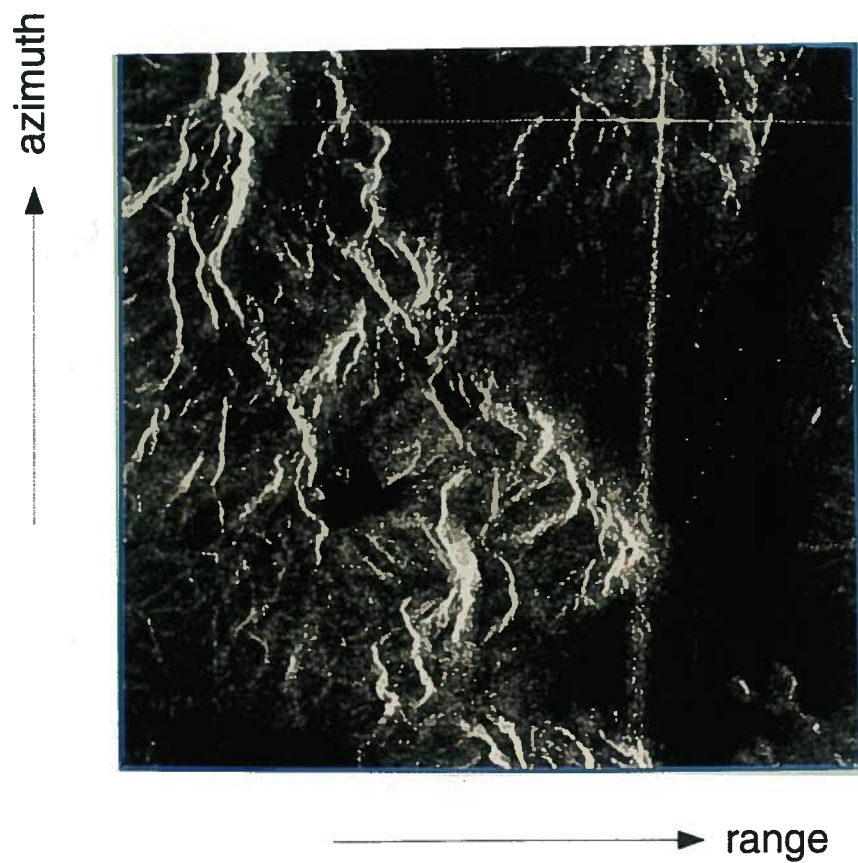


Figure 5.22: Seasat Goldstone scene processed with chirp scaling algorithm.

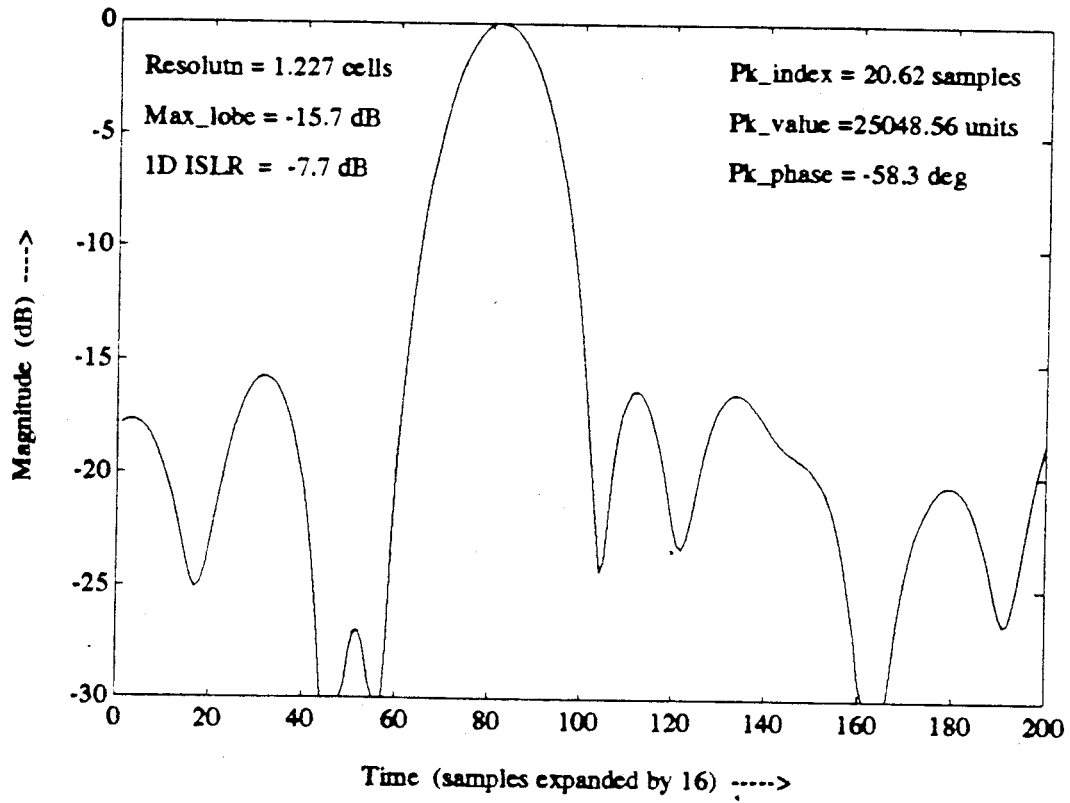


Figure 5.23: Range slice of point spread function for range-Doppler algorithm.

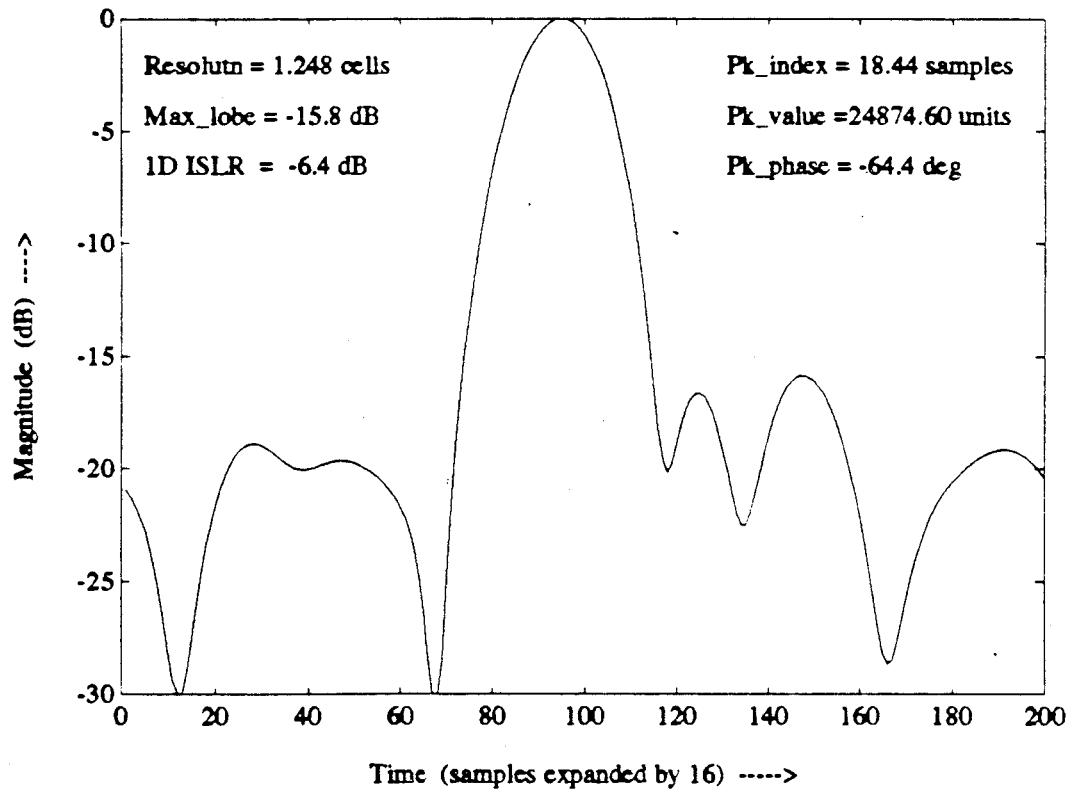


Figure 5.24: Azimuth slice of point spread function for range-Doppler algorithm.

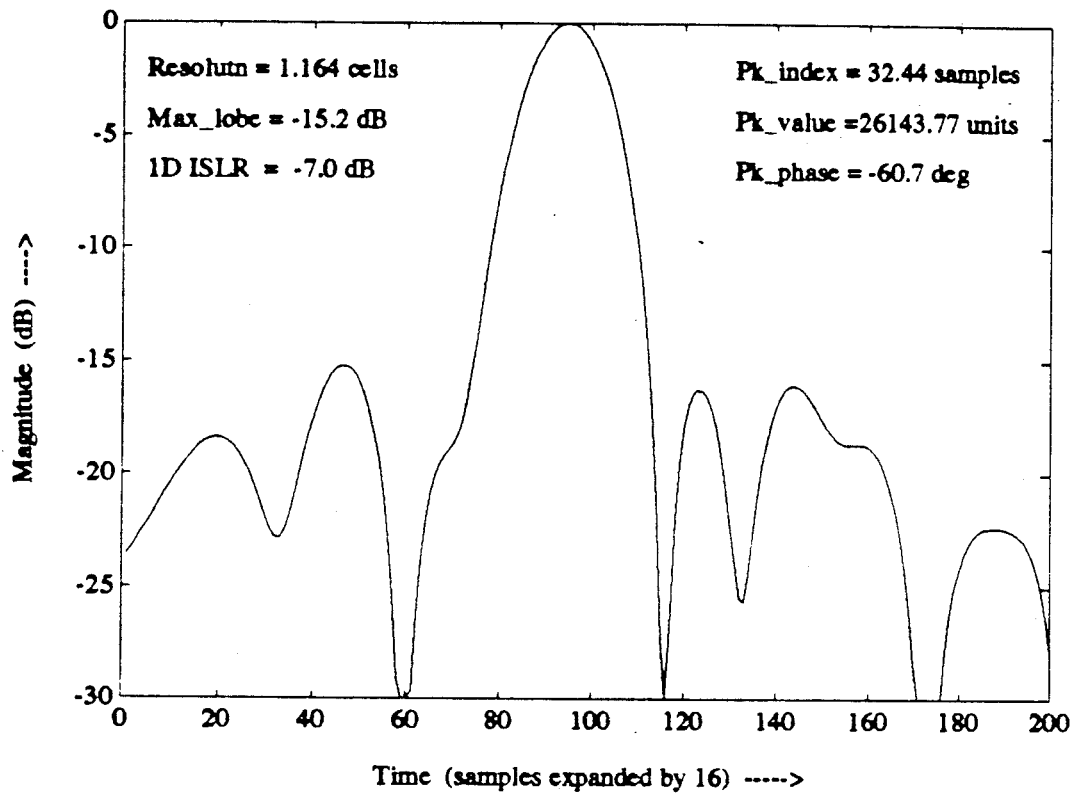


Figure 5.25: Range slice of point spread function for chirp scaling algorithm.

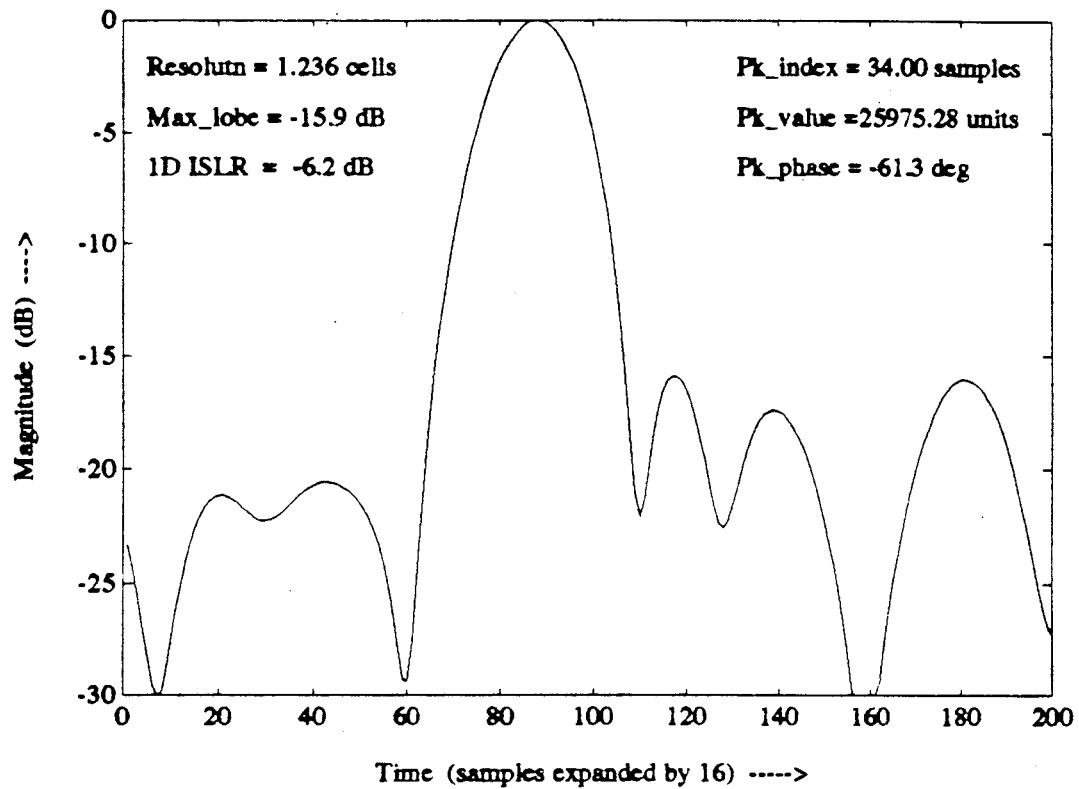


Figure 5.26: Azimuth slice of point spread function for chirp scaling algorithm.

algorithm	range		azimuth		phase (degrees) mean/std.dev.
	resolution	ISLR	resolution	ISLR	
GSAR	1.259	-9.7	1.332	-11.1	3.4/10.0
chirp scaling	1.206	-9.6	1.289	-11.3	

Table 5.5: Average resolution and integrated sidelobe ratio for range-Doppler and chirp scaling processors, and mean and standard deviation of difference in peak phase.

point spread function in one direction. The difference in sidelobe level between the processors is negligible, while the chirp scaling algorithm improves resolution by about four percent in range and three percent in azimuth. The difference in range resolution is due to the interpolator in the range-Doppler algorithm, since a truncated interpolating kernel has the effect of reducing the range bandwidth for the given range sampling rate. It should be mentioned that the GSAR processor that was used employed a four point interpolator. Increasing the interpolator length to eight points reduces the artifacts and the loss of range bandwidth, at the cost of greater complexity. Also shown in the table is the mean and standard deviation of the difference in peak phase between the two processors, which is within the measurement error of the point scatterer analysis program.

### 5.2.2 Azimuth Frequency Dependence of SRC

As discussed in Chapter 3, the chirp scaling algorithm differs from the range-Doppler algorithm in terms of matching the phase of the SAR transfer function. In range-Doppler, the coefficient of the SRC filter is calculated at the Doppler centroid, and kept constant in azimuth-frequency, while the chirp scaling algorithm allows the SRC filter to vary with azimuth-frequency. For small squint angles, this approximation to SRC in the range-Doppler algorithm does not introduce a significant degradation in the image. As the squint angle increases, the mismatch in SRC causes a range compression error in the range-Doppler domain. In the range direction, as mentioned in Chapter 3, this causes an overall broadening and an increase in sidelobes in the point spread

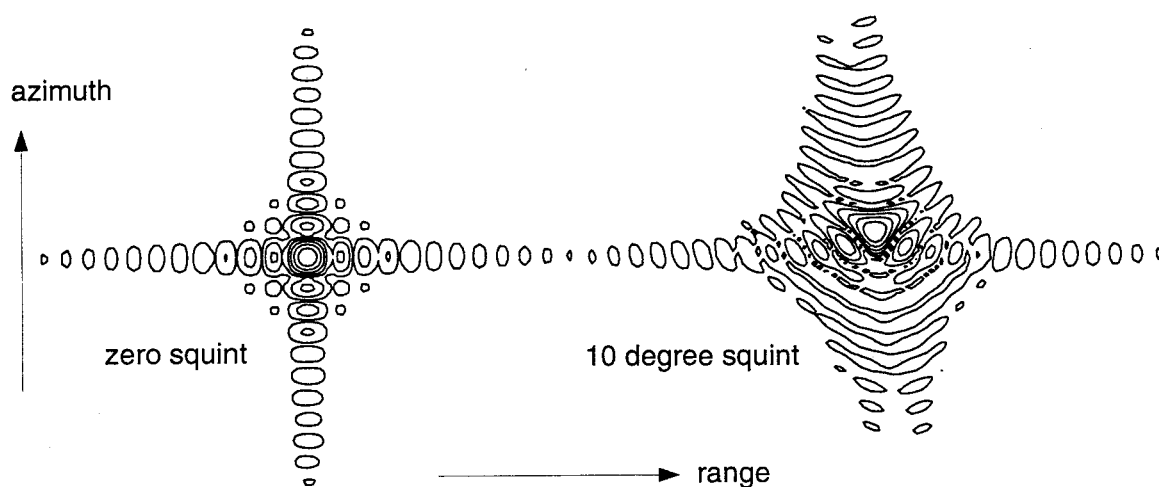


Figure 5.27: Contour plot of point spread function for range-Doppler algorithm, spaceborne L-band parameters, zero and 10 degree squint.

function. In addition, the variation of the compression error with azimuth-frequency results in a degradation of the point spread function in the azimuth direction as well. One effect is that the peak phase error in the range compressed pulses varies with azimuth-frequency. At small squint angles, this results in a linear phase error term in azimuth-frequency which causes a small azimuth shift in the point spread function. In addition, the compression error reduces the magnitude of the range compressed pulses towards the edges of the azimuth-frequency band. This introduces an amplitude weighting of the azimuth spectrum that increases the azimuth resolution width of the point spread function. For larger squint angles, the combination of the range broadening, range sidelobes, and azimuth phase error results in a severe distortion of the point spread function. This is illustrated in Figure 5.27, which shows two contour plots of point spread functions for the range-Doppler algorithm, corresponding to zero and ten degrees squint. The algorithm was used to process simulated point scatterer data corresponding to a L-band, spaceborne SAR.

Finally, to compare the performance of the range-Doppler and chirp scaling algorithms, both algorithms were used to process simulated point scatterer data for different squint angles. Spaceborne SAR parameters representative of Seasat and ERS-1 were used in the simulation,

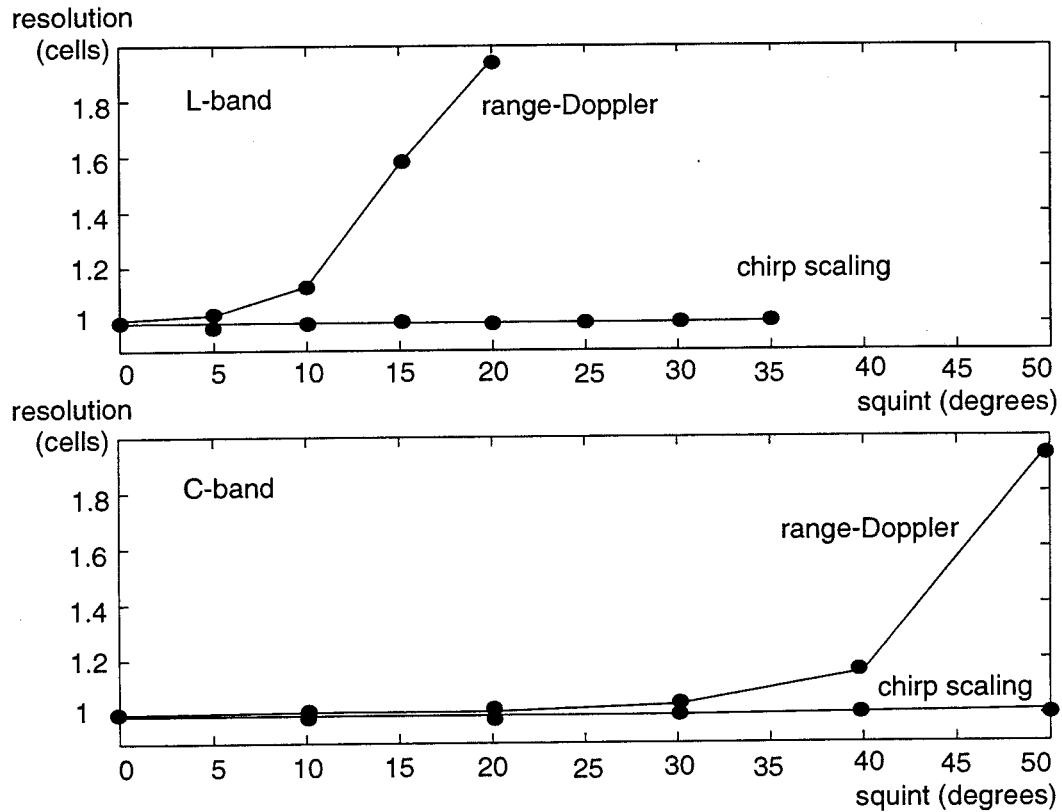


Figure 5.28: Range resolution versus squint for range-Doppler and chirp scaling algorithms. Scatterer at reference range. Top: L-band. Bottom: C-band.

with the scatterer placed at the reference range. The range resolution width of the point spread function was measured to indicate processing performance. Resolution is measured in cells, where one range cell is the theoretical 3dB resolution width of a *sinc* function. Figure 5.28 shows plots of the range resolution versus squint angle, for range-Doppler and chirp scaling algorithms used to process L-band and C-band data. For the L-band case, the approximation to SRC in the range-Doppler algorithm begins to degrade the range resolution at squint angles above five degrees. For C-band, the degradation becomes noticeable at squint angles above thirty degrees.

### 5.3 Side-Effects of Chirp Scaling

As discussed in Chapter 3, the chirp scaling algorithm accommodates the range dependence of RCMC without an interpolating filter. However, as indicated in the SAR transfer function of the chirp scaled signal in Equation (3.95), the multiplication by the chirp scaling phase function introduces some side-effects into the range spectrum of the signal in the two-dimensional frequency domain. These should be investigated to determine how significant they become at high squint.

Side-effects of chirp scaling include a change in the range bandwidth by the scale factor,  $\alpha(f_\eta)$ , defined in Equation (3.90), and a range-frequency shift,  $\delta f_\tau = -q_2(f_\eta)\Delta\tau(f_\eta; r)$ . Here  $q_2$  is the coefficient of the chirp scaling phase function and  $\Delta\tau(f_\eta; r)$  is the range-time delay from the reference trajectory, where  $r$  is the closest approach range variable in the signal model. Both these effects increase with wavelength and with squint angle. To ensure that the Nyquist criterion is satisfied, the scale factor  $\alpha$  should not increase the range bandwidth by more than the oversampling rate of the signal, which is typically about twenty percent. The range-frequency shift is range dependent, since a quadratic or higher order phase function causes a frequency shift in the received pulse that varies with its delay from the reference trajectory. The shift is zero at the reference trajectory and increases toward the edge of the range swath. Because of the range dependence of the frequency shift, it cannot be compensated during range processing in the frequency domain. Thus the shift must be small enough to keep the range-frequency components of the signal below the Nyquist rate, in order to avoid a loss of range bandwidth when processing with the range matched filter. Also, if frequency domain weighting to reduce sidelobes is applied to the chirp scaled signal, the window must be wide enough to account for this frequency shift.

Using the definition for  $q_2(f_\eta)$  in Equation (3.94), an expression for the frequency shift is

$$\delta f_\tau = -[\alpha(f_\eta) - 1]K_{mref}(f_\eta)\Delta\tau(f_\eta; r). \quad (5.144)$$

As a fraction of the range bandwidth, this frequency shift is equal to the ratio of the trajectory

shift to the pulse length. The azimuth-frequency dependence of the frequency shift is given mostly by the  $[\alpha(f_\eta) - 1]$  term, since  $\alpha$  is close to one. By using approximations in the definition of  $\alpha$ , this term can be shown to be

$$[\alpha(f_\eta) - 1] \approx \frac{c^2 f_{\eta r}}{4 f_0^2 B} (f_\eta - f_{\eta r}). \quad (5.145)$$

Thus, the change in range bandwidth and the range frequency shift increase with the difference between the azimuth-frequencies in the signal band and the reference azimuth-frequency,  $f_{\eta r}$ . Intuitively, this can be seen from Figure 3.6 since the required amount of scaling increases with azimuth-frequency difference from  $f_{\eta r}$ .

If the reference azimuth-frequency is set equal to the Doppler centroid, then the effects of chirp scaling are minimized for the given squint and wavelength. In this case, for the worst case squint angles and wavelengths that were investigated, the change in range bandwidth and the frequency shift were both less than two percent, which is negligible. In a later chapter, however, it will be advantageous to choose a value of  $f_{\eta r}$  outside of the azimuth-frequency band of the signal. This increases the change in range bandwidth and the range frequency shift, and the resulting constraint on the squint angle will be investigated in Chapter 7.

Finally, recall that after processing in the two dimensional frequency domain, a phase correction is applied in the range-Doppler domain. This removes a range dependent phase,  $\phi_\Delta(f_\eta; r)$  that is left in the signal after chirp scaling. The phase correction term is given in Equation (3.96) as a function of the range-time delay from the reference trajectory,  $\Delta\tau(f_\eta; r)$ . The removal of this phase requires a multiplication of the data by the conjugate phase term, and since the phase is range dependent, this introduces a range-frequency shift in the data. This multiplication is done in the range-Doppler domain, where the range-time to a scatterer is measured by  $\Delta\tau(f_{\eta r}; r)$ . Thus, to find the range-frequency shift implied by the phase correction,  $-\phi_\Delta$  can be expressed as a function of  $\Delta\tau(f_{\eta r}; r)$  by using the relationship between  $\Delta\tau(f_\eta; r)$  and  $\Delta\tau(f_{\eta r}; r)$  in Equation (3.89):

$$-\phi_\Delta(f_\eta; r) = \pi K_{mref} [\alpha - 1] \alpha \Delta\tau^2(f_{\eta r}; r). \quad (5.146)$$

Then, taking the derivative with respect to  $\Delta\tau(f_{\eta r}; r)$ , the range-frequency shift of the data that results from removing the phase correction term can be shown to be

$$\frac{-\phi'_{\Delta}}{2\pi} = [\alpha - 1]K_{mref}\Delta\tau(f_{\eta}; r), \quad (5.147)$$

which is equal to  $-\delta f_{\tau}$ . Thus, although the range-frequency shift in the two dimensional frequency domain must be kept small enough to avoid a loss of range bandwidth in range compression, this shift is later corrected so that the range-frequency content of the processed image is at the proper location.

#### 5.4 Approximations in Chirp Scaling

In removing the range dependence of RCMC, the chirp scaling algorithm makes several approximations to the representation of the signal in the range-Doppler domain. First, an approximation to the desired trajectory is made by assuming a constant value for the  $B$  parameter, which affects the accuracy of range cell migration correction. Also, the modified range frequency rate,  $K_m$ , is assumed to be range invariant when computing the secondary range compression filter and the chirp scaling phase function. Errors in range compression result in broadening and increased sidelobes at ranges away from the reference range. Also, approximations in the chirp scaling function result in errors in range cell migration correction that may become significant at high squint angles. Errors in RCMC leave some signal energy dispersed in the range direction, resulting in range registration errors and range broadening. Finally, at high squint angles, the cubic term in the expansion of the SAR focussing phase in Equation (3.51) may be significant. In the range-Doppler domain, this becomes a nonlinear FM component in the received pulses which may affect the assumption of linear FM in the chirp scaling algorithm.

##### 5.4.1 Constant $B$ Assumption

In this section, the RCMC error due to the constant  $B$  assumption in chirp scaling is quantified. This error is the difference between the desired trajectory, and its approximation used in deriving

the chirp scaling phase function. From Equations (3.86) and (3.91), this can be shown to be

$$\tau_{Berr}(f_\eta; r) = \tau_d(f_{\eta r}; r) \left[ \frac{\gamma(f_\eta; r_{ref})\gamma(f_{\eta r}; r)}{\gamma(f_{\eta r}; r_{ref})\gamma(f_\eta; r)} - 1 \right]. \quad (5.148)$$

The error increases with the difference in range from the reference range, and with the difference in azimuth-frequency from the reference azimuth-frequency. The error described by Equation (5.148) can be thought of consisting of a registration error, which is the error at the Doppler centroid, and an error in RCMC over the azimuth-frequency band, which affects the range resolution of the point spread function. If the reference azimuth-frequency is set equal to the Doppler centroid, then the only error is the RCMC error within the signal band. If the reference azimuth-frequency is placed outside of the signal band, then a registration error is introduced, while the variation of RCMC error within the signal band changes only slightly. In general, to avoid a noticeable range broadening of the point spread function, the in-band RCMC error should be less than about a quarter of a cell [37].

To evaluate this error using spaceborne SAR parameters, the  $B$  parameter in the model for the distance equation, as described in Chapter 4, was calculated for different squint angles and ranges. A circular orbit geometry was used for this calculation, although it should be noted that for deviations from a circular orbit, the rate of change of  $B$  with range can increase significantly. The parameters of Table 4.2 were used in the calculations. The results are shown in Table 5.6, for L-band and C-band, with the scatterer placed at the edge of the range swath where  $(r - r_{ref}) = 20 \text{ km}$ . Also, the reference azimuth-frequency is placed outside the signal band as will be described in Chapter 7. This indicates the in-band RCMC error that occurs in the chirp scaling algorithm, while also showing the registration error that is introduced by choosing  $f_{\eta r}$  as in Chapter 7. The registration and in-band RCMC errors are given relative to a range resolution cell. In general, the error increases with squint and with wavelength. The constant  $B$  approximation begins to cause noticeable broadening due to in-band RCMC when the squint angle is about fifteen degrees for L-band, and about thirty degrees for C-band.

squint (degrees)	Error (in cells) due to $B$ variation			
	L-band		C-band	
	regist.	in-band RCMC	regist.	in-band RCMC
10	0.24	0.13	0.06	0.03
20	1.02	0.36	0.28	0.09
30	3.92	0.97	1.12	0.23
40	18.6	3.42	5.9	0.83
50			64.6	5.93

Table 5.6: Registration and in-band RCMC errors (in range cells) due to constant  $B$  approximation in the desired trajectory in the chirp scaling algorithm.

#### 5.4.2 Constant Range Frequency Rate Assumption

To investigate the effect of approximating the range frequency rate by a constant, assume that the modified frequency rate at range  $r$  can be written as a linear function of range-time in the range-Doppler domain:

$$K_m(f_\eta; r) = K_{mref}(f_\eta) + K_s(f_\eta)\Delta\tau(f_\eta; r), \quad (5.149)$$

where  $K_s$  is the slope of the of the frequency rate with respect to range-time.  $K_s$  can be found by taking the derivative of  $K_m(f_\eta; r)$  with respect to range-time,  $\tau_d$ , and evaluating at the reference range. Also, the range dependence of  $B$  modifies the slope of the range frequency rate slightly. To express this, let  $B$  be modelled as a linear function of closest approach range,

$$B = B_r + B_s(r - r_{ref}), \quad (5.150)$$

where  $B_r$  is the value at the reference range, and  $B_s$  is the slope. This gives the following expression for  $K_s$ :

$$K_s(f_\eta) = K_{s0}(f_\eta)\left[1 - \frac{r_{ref}B_s}{B_r\gamma^2(f_\eta; r_{ref}) - 0.5r_{ref}B_s(1 - \gamma^2(f_\eta; r_{ref}))}\right], \quad (5.151)$$

where  $K_{s0}$  is the slope for the case of a constant  $B$  (as in a rectilinear geometry), given by

$$K_{s0}(f_\eta) = -\frac{K_{mref}^2(f_\eta)(1 - \gamma^2(f_\eta; r_{ref}))}{f_0\gamma^2(f_\eta; r_{ref})}. \quad (5.152)$$

Using  $K_s$ , the point scatterer response in the range-Doppler domain, as given in Equation (3.83), can be modified to include the range dependence of  $K_m$  as follows:

$$S(f_\eta, \tau; r) = F_{ac}(f_\eta; r) m \left[ \frac{K_{mref}}{K} (\tau - \tau_d) \right] \exp[-j\pi K_{mref} (\tau - \tau_d)^2 - j\pi K_s \Delta\tau (\tau - \tau_d)^2]. \quad (5.153)$$

Applying the chirp scaling phase function to this signal and then taking the range Fourier transform gives the SAR transfer function of the chirp scaled signal, as in Equation 3.95. By including  $K_s$  in the derivation, extra terms are introduced in the phase of the SAR transfer function that are not accommodated in the processing. These terms correspond to errors in RCMC and SRC.

The RCMC error is given by

$$\tau_{K_s}(f_\eta; r) = \frac{-K_s}{K_{mref}} \left[ 1 - \frac{1}{\alpha} \right] \Delta\tau^2(f_\eta; r), \quad (5.154)$$

which increases with the difference in range from  $r_{ref}$ , and with the difference in azimuth-frequency from  $f_{\eta r}$ . This error is investigated in Table 5.7, which shows the registration error and in-band RCMC error, in range cells, as a function of squint angle for L-band and C-band cases. The same parameters were used as in the investigation of the constant  $B$  assumption described above. Also, the scatterer is assumed to be at the edge of the range swath, where  $(r - r_{ref}) = 20 \text{ km}$ , and  $f_{\eta r}$  is placed outside of the azimuth-frequency band. As can be seen, the effect on RCMC of the constant frequency rate assumption in chirp scaling is less than the effect of the constant  $B$  assumption described above. However, registration and in-band RCMC errors become noticeable between twenty and thirty degrees squint for L-band, and at about forty degrees for C-band.

Given the range frequency rate error due to  $K_s$ , the SRC error term in the SAR transfer function of the chirp scaled signal is given by

$$\phi_{err}(f_\eta, f_\tau; r) = \frac{\pi K_s \Delta\tau(f_\eta; r)}{\alpha^2 K_{mref}^2} f_\tau^2. \quad (5.155)$$

This is a range quadratic phase error that occurs at all azimuth-frequencies, and increases with the difference in the scatterer's range from the reference range. Thus, the effect on the processed

squint	Error (in cells) due to $K_m$ variation			
	L-band		C-band	
	regist.	in-band RCMC	regist.	in-band RCMC
10	0.03	0.02	0.002	0.001
20	0.31	0.13	0.026	0.01
30	1.52	0.40	0.18	0.04
40	5.7	1.05	0.98	0.14
50			6.8	0.62

Table 5.7: Registration and in-band RCMC errors (in range cells) in the chirp scaling due to range dependence of  $K_m$ .

image is a range compression error that increases towards the edges of the swath. The effect of a compression error was described in Chapter 2, as a function of the maximum quadratic phase error at the edge of the range-frequency band. For the range compression error due to the range dependence of SRC, the maximum quadratic phase error is shown in Table 5.8 for different squint angles. Results are presented for L-band and C-band, assuming a scatterer placed at the edge of the range swath,  $(r - r_{ref}) = 20 \text{ km}$ . To keep the range broadening to within about five percent, this quadratic phase error should be less than about 90 degrees [44]. Beyond this, the broadening increases very rapidly. For an L-band SAR, as the squint angle increases beyond about 10 degrees, the quadratic phase errors shown in the table result in range impulse response widths of several cells. For C-band radars, the problem is slightly less severe, and a significant focussing error occurs for squint angles greater than about 20 degrees.

### 5.4.3 Linear FM Assumption

At high squint angles, the cubic term in the expansion of the phase of the SAR transfer function should be included. To investigate the effect of the cubic term,  $\phi_3(f_\eta; r)f_\tau^3$ , on chirp scaling, a range-Doppler representation of the signal such as Equation (3.83) needs to be derived. From the SAR transfer function, the range-Doppler domain representation is obtained by an inverse

	maximum quadratic phase error (degrees)	
squint	L-band	C-band
10	82	18
20	350	82
30	982	236
40	2461	645
50		2234

Table 5.8: Maximum quadratic phase error in SRC due to its range-dependence.

range Fourier transform:

$$S(f_\eta, \tau; r) = F_{ac}(f_\eta; r) \int M(f_\tau) \exp[j2\pi(\tau - \tau_d)f_\tau + j\pi \frac{f_\tau^2}{K_m} + j\phi_3 f_\tau^3] df_\tau. \quad (5.156)$$

Since the cubic term is relatively small, an approximation to the method of stationary phase for evaluating this integral can be found, as shown in Appendix A. In the result, phase terms up to the cubic in range-time are kept, giving the following range-Doppler representation of the signal:

$$S(f_\eta, \tau; r) = F_{ac}(f_\eta; r) m \left[ \frac{K_m}{K} (\tau - \tau_d) \right] \exp \left[ -j\pi K_m (\tau - \tau_d)^2 - \frac{j2\pi \Delta C_m}{3} (\tau - \tau_d)^3 \right], \quad (5.157)$$

where the cubic coefficient,  $\Delta C_m$ , is defined as

$$\Delta C_m(f_\eta; r) = K_m^3(f_\eta; r) \frac{3\phi_3(f_\eta; r)}{2\pi}. \quad (5.158)$$

Also, the effect of the cubic term on the amplitude has been ignored. Next, the chirp scaling phase function is applied to the range-Doppler domain signal, and then the range Fourier transform is taken to get the SAR transfer function of the chirp scaled signal:

$$S_{2\alpha}(f_\eta, f_\tau; r) = F_{ac}(f_\eta; r) \int m \left[ \frac{K_m}{K} (\tau - \tau_d) \right] e^{-j\pi K_m (\tau - \tau_d)^2 - j\frac{2\pi \Delta C_m}{3} (\tau - \tau_d)^3 - j\pi q_2 (\tau - \tau_{ref})^2 - j2\pi f_\tau \tau} d\tau. \quad (5.159)$$

Again, since the cubic term is small, an approximation to the method of stationary phase is used to evaluate the integral. Appendix B describes the method of approximation for the general

case of small higher order phase terms and a more general chirp scaling phase function. In the case described here, however, a quadratic phase chirp scaling phase function is used, and for the purposes of investigating the effect of  $\Delta C_m$  on the SAR transfer function only the phase terms up to the cubic are kept in the solution. Compared to the SAR transfer function without the cubic phase term shown in Equation (3.95),  $\Delta C_m$  introduces the following extra phase terms to the SAR transfer function, which are not accommodated in processing:

$$\begin{aligned} \phi_{err} = & \frac{2\pi\Delta C_m f_\tau^3}{3\alpha^3 K_m^3} \\ & + \frac{2\pi\Delta C_m(\alpha-1)\Delta\tau(f_\eta; r)f_\tau^2}{\alpha^3 K_m^2} \\ & + \frac{2\pi\Delta C_m(\alpha-1)^2\Delta\tau^2(f_\eta; r)f_\tau}{\alpha^3 K_m} \\ & + \frac{2\pi\Delta C_m(\alpha-1)^3\Delta\tau^3(f_\eta; r)}{3\alpha^3}. \end{aligned} \quad (5.160)$$

The first term corresponds to a cubic phase term that needs to be included in the range compression filter, and arises from the  $\phi_3$  term in the SAR transfer function. This is not greatly affected by chirp scaling, and is only slightly range dependent. Thus it does not pose a problem in processing. The second term is a quadratic phase error in range compression that arises from the interaction of chirp scaling with the cubic phase term. Also, it depends on range as  $\Delta\tau(f_\eta; r)$ , and so cannot be accommodated in processing. Similarly, the third term is an error in RCMC that results from the interaction of chirp scaling with the cubic phase term. It depends on range as  $\Delta\tau^2(f_\eta; r)$ , and so cannot be accommodated by the chirp scaling phase function. Finally, the last term is a range dependent phase error, and can be accommodated in the range-Doppler domain.

To determine the significance of these errors, Tables 5.9 and 5.10 show the results of calculating these errors using spaceborne SAR parameters for L-band and C-band, respectively. The left half of each table investigates the effect of the cubic phase term on range compression. The first column in the table shows the total cubic phase error that would result if the cubic phase term were not included in the range matched filter. The next column shows the difference in cubic phase error between the edge of the swath and the reference range, which is the error that

	L-band			
	max. cubic phase error		effects of chirp scaling	
squint (degrees)	total phase error (degrees)	difference from $r_{ref}$ (degrees)	quadratic phase error (degrees)	maximum RCMC error (cells)
10	29	0.2	2	0.0
20	142	0.2	12	0.01
30	500	9.0	48	0.08
40	1898	64.7	170	0.35

Table 5.9: Errors due to cubic phase term in SAR transfer function, L-band.

would occur if the cubic phase term in the range matched filter were calculated at the reference range. This is calculated for  $(r - r_{ref}) = 20 \text{ km}$ . As seen in the tables, the cubic phase term should be included in the secondary range compression filter for squint angles greater than 20 degrees for L-band, and about 40 degrees for C-band. However, even in the worst case, the range dependence of the cubic term in SRC can be neglected. Next, the right half of the tables investigates the effects of the cubic phase term with chirp scaling. Shown are the maximum range quadratic phase error and maximum error in RCMC (including registration and in-band RCMC) at the edge of the swath. The reference azimuth-frequency was set outside of the azimuth-frequency band. Of these errors, the quadratic phase error is the largest, and does not become significant until about 30 degrees squint for L-band, and is negligible for C-band.

#### 5.4.4 Simulations

To investigate the approximations in chirp scaling, point scatterer data was simulated for different squint angles, and with the scatterer placed at different distances from the reference range. Spaceborne SAR parameters representative of Seasat (L-band) and ERS-1 (C-band) were used in the simulation. The point scatterer response was generated using the signal model for high squint, spaceborne SAR described in Chapter 4. In this model, a circular orbit was assumed in calculating the  $B$  parameter and the rate of change of  $B$  with range. The simulated data was processed with the chirp scaling algorithm, with the reference azimuth frequency set equal

C-band				
	max. cubic phase error		effects of chirp scaling	
squint (degrees)	total phase error (degrees)	difference from $r_{ref}$ (degrees)	quadratic phase error (degrees)	maximum RCMC error (cells)
10	2	0.03	0.02	0.00
20	8	0.1	0.2	0.00
30	27	0.2	1.1	0.00
40	103	0.97	5.6	0.00
50	596	20.0	38.1	0.11

Table 5.10: Errors due to cubic phase term in SAR transfer function, C-band.

to the Doppler centroid. Also, to obtain the best possible results, the cubic phase term of the SAR transfer function, calculated at the reference range, was included in the secondary range compression filter. The measured range resolution, in cells, is plotted versus squint angle for each case in Figure 5.29. In addition, the maximum sidelobe level in the range direction is given for the different cases in Table 5.11. The azimuth resolution and sidelobe level were not significantly affected by approximations in the chirp scaling algorithm. At the reference range, the chirp scaling algorithm correctly matches the phase of the SAR transfer function, and the theoretical resolution of one cell is achieved independently of squint. When the scatterer is located away from the reference range, the range dependence of SRC degrades the resolution as squint increases. For L-band, the resolution width increases rapidly for squint angles above 15 degrees for a scatterer at 10 km from the reference range, and above 10 degrees for a scatterer at  $(r - r_{ref}) = 20$  km. Similarly, for squint angles above 10 degrees, the sidelobe level increases compared to the  $-13.2$  dB level of the *sinc* function. For C-band, resolution degrades for squint angles above thirty degrees with  $(r - r_{ref}) = 10$  km, and for  $(r - r_{ref}) = 20$  km the resolution width increases rapidly for squints above 20 degrees. The sidelobe level increases for squint angles above 20 degrees.

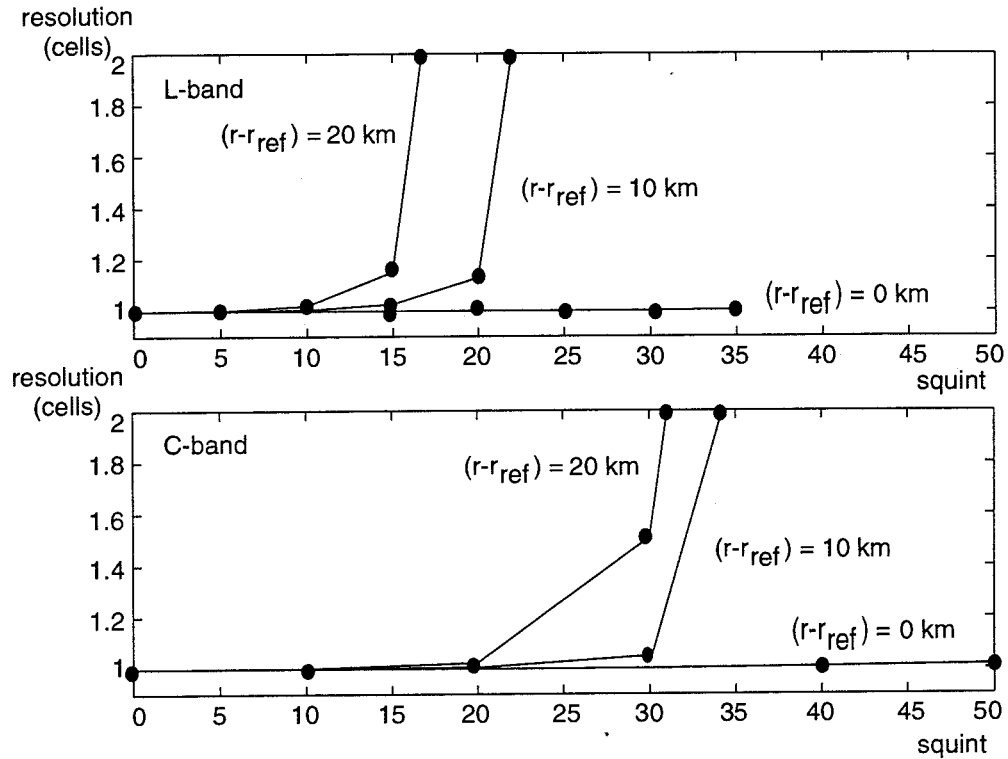


Figure 5.29: Simulation results of measured range resolution versus squint for chirp scaling algorithm with scatterer at different distances from the reference range. Top: L-band. Bottom: C-band.

		Maximum sidelobe level in range (dB)			
		L-band		C-band	
squint		$r - r_{ref} = 10km$	$r - r_{ref} = 20km$	$r - r_{ref} = 10km$	$r - r_{ref} = 20km$
0		-13.2	-13.2	-13.2	-13.2
10		-12.8	-11.7	-13.2	-13.1
20		-7.0	-0.3	-12.7	-11.3
30		-	-	-9.7	-3.5
40		-	-	-0.8	-

Table 5.11: Simulation results of maximum sidelobe level in the range direction for the chirp scaling algorithm with scatterer at different distances from the reference range.

### 5.5 Effect of Pulse Phase Errors

The chirp scaling algorithm depends on properties of the transmitted pulse to achieve accurate processing. In particular, a linear FM pulse of a specific frequency rate is assumed. Generally, the pulse is generated with sufficient accuracy so that the broadening after pulse compression is within specifications. However, the effect of pulse phase errors on the ability of chirp scaling to perform accurate processing should be investigated.

Consider a transmitted pulse of the form

$$p(\tau) = m(\tau) \exp[-j\pi K\tau^2 - j2\pi\varepsilon(\tau)], \quad (5.161)$$

where  $\varepsilon(\tau)$  represents the error and is assumed to be much smaller than the total pulse phase. To determine the effect of the error on chirp scaling, the SAR transfer function of the chirp scaled signal is derived for this case. The Fourier transform of the transmitted pulse is obtained by an approximation to the method of stationary phase for a general pulse phase error, shown in Appendix C. To first order in  $\varepsilon(\tau)$ , the Fourier transform of the pulse is given by

$$P(f_\tau) = M(f_\tau) \exp\left[\frac{j\pi f_\tau^2}{K} - j2\pi\varepsilon\left(\frac{-f_\tau}{K}\right)\right], \quad (5.162)$$

where constants and the effect of  $\varepsilon$  on the amplitude have been ignored. Then, substituting for  $P(f_\tau)$  in the form of the SAR transfer function in Equation (2.43), a range inverse transform gives the range-Doppler representation of the signal. Again, using the approximation shown in Appendix C, the range-Doppler domain signal is, to first order:

$$S(f_\eta, \tau; r) = F_{ac}(f_\eta; r) m\left(\frac{K_m}{K}(\tau - \tau_d)\right) \exp\left[-j\pi K_m(\tau - \tau_d)^2 - j2\pi\varepsilon\left(\frac{K_m}{K}(\tau - \tau_d)\right)\right]. \quad (5.163)$$

Finally,  $S(f_\eta, \tau; r)$  is multiplied by the chirp scaling phase function, and the range Fourier transform of the result is obtained as shown in Appendix C. This gives the SAR transfer function of the chirp scaled signal. Compared to the expression for the SAR transfer function in Equation (3.95), the pulse phase error introduces an extra phase term given by

$$\phi_{err} = -2\pi\varepsilon\left[\frac{-f_\tau}{\alpha K} - \frac{K_m}{K}\left(1 - \frac{1}{\alpha}\right)\Delta\tau\right]. \quad (5.164)$$

This expression can be used to find the effect on the processing accuracy due to the interaction of the pulse phase error and chirp scaling. Note that even without chirp scaling, a processing error exists due to the pulse phase error. In Equation (5.164), in the absence of chirp scaling,  $\alpha$  is equal to one, and the phase error of the SAR transfer function reduces to that of the Fourier transform of the pulse,  $-2\pi\varepsilon(\frac{-f_\tau}{K})$ . To see the effect of chirp scaling, then, what is important is the difference between  $\phi_{err}$  in Equation (5.164) and  $-2\pi\varepsilon(\frac{-f_\tau}{K})$ .

Given the form of  $\phi_{err}$  compared to the processing error without chirp scaling, the effects of chirp scaling on certain types of pulse phase errors can be deduced. Note that in Equation (5.164), an effect of chirp scaling is a shift of the processing error as a function of range-frequency. Thus, if the pulse phase error  $\varepsilon(\tau)$  is distributed more or less uniformly across the pulse, as in a cyclic error, then the type of processing error that results is not changed by chirp scaling. On the other hand, if  $\varepsilon(\tau)$  has the form of a polynomial across the pulse, such as a quadratic or cubic, then chirp scaling introduces lower order phase error terms in range frequency, giving rise to errors in RCMC and SRC.

First, consider an error in frequency rate,  $\Delta K$ , which results in a quadratic pulse phase error given by

$$\varepsilon(\tau) = \frac{\Delta K \tau^2}{2}. \quad (5.165)$$

Using this expression for  $\varepsilon(\tau)$  to evaluate  $\phi_{err}$  gives

$$\begin{aligned} \phi_{err} &= -\frac{\pi \Delta K f_\tau^2}{\alpha^2 K^2} \\ &\quad -\frac{2\pi \Delta K_m}{\alpha K^2} \left(1 - \frac{1}{\alpha}\right) \Delta \tau f_\tau \\ &\quad -\frac{\pi \Delta K_m^2}{K^2} \left(1 - \frac{1}{\alpha}\right)^2 \Delta \tau^2. \end{aligned} \quad (5.166)$$

In the first term, which affects the range compression error due to  $\Delta K$ , the only effect of chirp scaling is to modify the frequency rate error slightly. Also, the phase error represented by the last term is very small. The second term, which is linear in  $f_\tau$ , represents a range dependent error in RCMC. Thus, this term shows how the ability of chirp scaling to remove the range dependence of RCMC is affected by a quadratic pulse phase error. To investigate this error,

Error due to quadratic pulse phase error				
	L-band		C-band	
squint (degrees)	regist. (cells)	in-band RCMC (cells)	regist. (cells)	in-band RCMC (cells)
10	0.01	0.006	0.003	0.002
20	0.02	0.01	0.007	0.003
30	0.03	0.01	0.014	0.005
40	0.04	0.01	0.026	0.006
50			0.046	0.006

Table 5.12: Registration and RCMC errors (in cells) due to chirp scaling with quadratic phase error in pulse. L-band and C-band spaceborne SAR parameters, with  $(r - r_{ref}) = 20km$

assume the frequency rate of the pulse is known to within 0.1 percent, giving a maximum quadratic phase error in the pulse of about thirty degrees. Also, for purposes of investigating the pulse phase error, the error due to the range dependence of  $K_m$  is ignored. Table 5.12 shows the registration and in-band RCMC errors as a function of squint angle, assuming the reference azimuth-frequency is placed outside of the band. Results are shown for L-band and C-band, for a scatterer at the edge of the swath where  $(r - r_{ref}) = 20 km$ . In all cases the errors are too small to be noticeable.

Next, consider a small deviation from linear FM in the transmitted pulse, represented by a cubic phase term:

$$\varepsilon(\tau) = \frac{\Delta C \tau^3}{3}. \quad (5.167)$$

For purposes of investigating the effect of this term on chirp scaling, the cubic term of the SAR focussing phase discussed earlier is ignored. Evaluating  $\phi_{err}$  with this form of  $\varepsilon(\tau)$  gives

$$\phi_{err} = \frac{2\pi\Delta C}{3} \left( \frac{f_\tau}{\alpha K} + \frac{K_m}{K} \left(1 - \frac{1}{\alpha}\right) \Delta\tau \right)^3. \quad (5.168)$$

This expression for  $\phi_{err}$  is the same as the one in Equation (5.160), except that the coefficient  $\Delta C$  is used instead of  $\Delta C_m$ .

To determine the effect of a typical cubic pulse phase error on the accuracy of chirp scaling, assume that  $\Delta C$  gives a cubic phase error in the transmitted pulse of  $10^\circ rms$ , or a maximum

cubic phase error at the pulse edge of 25 degrees [60]. The phase error terms in the SAR transfer function of the chirp scaled signal can be computed from Equation (5.168). However, the effect of  $\Delta C$  is very small. Of the phase terms that arise from the interaction of the cubic term with chirp scaling, the quadratic phase error due to  $\Delta C$  is less than ten degrees for the worst case wavelength and squint angle, and the RCMC error is less than 0.003 cells.

In general, the quadratic and cubic phase errors that are present in the transmitted pulse are too small to affect the accuracy of chirp scaling. Thus, chirp scaling is robust to phase errors in the transmitted pulse.

## Chapter 6

### Extensions to Chirp Scaling for RCMC

#### 6.1 Introduction

In the derivation of the chirp scaling algorithm shown in Chapter 3, certain approximations were made in removing the range dependence of RCMC. In particular, the equation for the desired trajectory assumes that the  $B$  parameter is constant in range and equal to its value at the reference range. Also, the chirp scaling phase function is found by assuming the frequency rate,  $K_m$  is independent of range. These approximations do not introduce any noticeable degradation for small squint angles. However, for the high squint angles investigated in Chapter 5, it was seen that the effects of these approximations can become noticeable. Thus, for accurate processing at high squint, the chirp scaling algorithm should be extended so as to remove these approximations in its derivation. It has been shown numerically in [61] that a higher order term in the chirp scaling phase function can achieve a nonlinear scaling of range lines, in order to accommodate higher order range dependence RCMC. In this chapter, mathematical representation of the higher order term in the chirp scaling phase function is derived. This is done by finding a more accurate representation of the desired trajectory, and including the range dependence of  $K_m$  in the signal model. With this extension to the chirp scaling phase function, the SAR transfer function of the chirp scaled signal is derived to show the effects on the processed signal.

#### 6.2 Representation of Desired Trajectory

For a spaceborne geometry, the ability to process squint mode SAR data accurately requires an accommodation of the range dependent  $B$  parameter in RCMC. As discussed in Chapter 3, the objective in chirp scaling is to change the delay from the reference trajectory to the scatterer

trajectory,  $\Delta\tau(f_\eta; r)$ , to a constant delay equal to  $\Delta\tau(f_{\eta r}; r)$ . This provides the desired trajectory, given by Equation (3.86), for scatterers at all ranges so that bulk RCMC can be performed in the two-dimensional frequency domain. In the chirp scaling algorithm, the relationship between  $\Delta\tau(f_\eta; r)$  and  $\Delta\tau(f_{\eta r}; r)$  was approximated by the expression in Equation (3.91), by assuming that  $B(r) \approx B(r_{ref})$ , which resulted in a linear scaling of range lines. In order to achieve the desired trajectory more accurately for higher squint angles, and thus achieve more accurate RCMC, the relationship between  $\Delta\tau(f_\eta; r)$  and  $\Delta\tau(f_{\eta r}; r)$  needs to incorporate the range dependence of  $B(r)$ .

To do this, first represent  $B(r)$  by the following quadratic function in range, with respect to the reference range:

$$B(r) \approx B_r + B_s(r - r_{ref}) + B_a(r - r_{ref})^2. \quad (6.169)$$

Then, since the effect of  $B(r)$  on the range variance of RCMC is small compared to the linear variation, it is sufficient to look for a higher order term in the relationship between  $\Delta\tau(f_\eta; r)$  and  $\Delta\tau(f_{\eta r}; r)$  which can be added to the approximation in Equation (3.91). This can be found by expanding  $\Delta\tau(f_\eta; r)$  and  $\Delta\tau(f_{\eta r}; r)$  in  $r$  about  $r_{ref}$ , keeping terms up to the quadratic:

$$\begin{aligned} \Delta\tau(f_\eta; r) &\approx a(f_\eta)(r - r_{ref}) + b(f_\eta)(r - r_{ref})^2 \\ \Delta\tau(f_{\eta r}; r) &\approx a(f_{\eta r})(r - r_{ref}) + b(f_{\eta r})(r - r_{ref})^2, \end{aligned} \quad (6.170)$$

The coefficients  $a(f_\eta)$  and  $b(f_\eta)$  are given by

$$\begin{aligned} a(f_\eta) &= \frac{2}{c\gamma(f_\eta; r_{ref})} \left[ 1 - \frac{r_{ref}(1 - \gamma^2(f_\eta; r_{ref}))B_s}{2\gamma^2(f_\eta; r_{ref})B_r} \right] \\ b(f_\eta) &= \frac{-(1 - \gamma^2(f_\eta; r_{ref}))}{c\gamma^3(f_\eta; r_{ref})} \left[ \frac{B_s}{B_r} + \frac{r_{ref}B_a}{B_r} - \frac{r_{ref}B_s^2}{B_r^2} \left( 1 + \frac{3(1 - \gamma^2(f_\eta; r_{ref}))}{4\gamma^2(f_\eta; r_{ref})} \right) \right], \end{aligned} \quad (6.171)$$

and depend on the reference range and on the coefficients of the  $B(r)$  variation.

The equations in (6.170) can be used to find a relationship between  $\Delta\tau(f_\eta; r)$  and  $\Delta\tau(f_{\eta r}; r)$  as follows. The first of the equations is used to find an approximate solution for  $(r - r_{ref})$  in terms of  $\Delta\tau(f_\eta; r)$ , by assuming that  $b(f_\eta) \ll a(f_\eta)$ . Then, by substituting this solution into

the second equation, and keeping terms up to the quadratic, the follow relationship between  $\Delta\tau(f_\eta; r)$  and  $\Delta\tau(f_{\eta r}; r)$  is obtained:

$$\Delta\tau(f_{\eta r}; r) \approx \frac{\Delta\tau(f_\eta; r)}{\alpha_B(f_\eta)} + \beta(f_\eta)\Delta\tau^2(f_\eta; r). \quad (6.172)$$

This expression is an extension of the linear relationship that was assumed in Equation (3.91), and the scaling factors  $\alpha_B(f_\eta)$  and  $\beta(f_\eta)$  can be shown to be:

$$\begin{aligned} \alpha_B(f_\eta) &= \frac{a(f_\eta)}{a(f_{\eta r})} \\ \beta(f_\eta) &= \frac{1}{a^2(f_\eta)} \left[ b(f_{\eta r}) - \frac{a(f_{\eta r})}{a(f_\eta)} b(f_\eta) \right]. \end{aligned} \quad (6.173)$$

Here  $\alpha_B(f_\eta)$  represents a linear scaling, although it has been modified slightly from the scale factor  $\alpha(f_\eta)$  used in Chapter 3, in order to provide a first order correction for a range dependent  $B$ . The quadratic factor,  $\beta(f_\eta)$ , represents a higher order nonlinear scaling to account for the nonlinear relationship between  $\Delta\tau(f_\eta; r)$  and  $\Delta\tau(f_{\eta r}; r)$ , which occurs in an orbital geometry at high squint angles. Note that when  $B$  is constant so that  $B_s = 0$  and  $B_a = 0$ , the scaling factors reduce to  $\alpha_B(f_\eta) = \alpha(f_\eta)$  and  $\beta(f_\eta) = 0$ . Thus, a more accurate representation of the desired trajectory is

$$\tau_s(f_\eta; r) \approx \tau_{ref}(f_\eta) + \frac{\Delta\tau(f_\eta; r)}{\alpha_B(f_\eta)} + \beta(f_\eta)\Delta\tau^2(f_\eta; r), \quad (6.174)$$

which will be used later in the derivation of the higher order chirp scaling function.

As in the investigation of the constant  $B$  approximation in Chapter 5, the error in RCMC due to the approximations in accommodating the range dependence of  $B(r)$  should be determined. This error is the difference between the desired trajectory, defined in Equation (3.86), and its approximation in Equation (6.174). In addition, the relative importance of each of the terms in the approximation can be determined, by calculating the error when only a linear scaling is used (with the modified scaling factor  $\alpha_B$ ), and the error when both the linear and quadratic scaling factors are used. Table 6.13 shows the maximum RCMC error (the sum of both registration and in-band RCMC error) for both types of approximation to the desired trajectory. The parameters

squint (degrees)	Error (in cells) due to $B$ variation			
	L-band		C-band	
	linear scaling	quadratic scaling	linear scaling	quadratic scaling
10	0.01	0.000	0.002	0.000
20	0.03	0.000	0.008	0.000
30	0.11	0.000	0.03	0.000
40	0.52	0.001	0.16	0.000
50			1.88	0.005

Table 6.13: Maximum RCMC error (in range cells) due to the approximation to desired trajectory when using only modified linear scaling, and when using both linear and quadratic scaling.

used in the calculations were the same as those in the investigation of the constant  $B$  assumption in Table 5.6. The results are presented for L-band and C-band, with the scatterer at the edge of the swath where  $(r - r_{ref}) = 20 \text{ km}$ , and the reference azimuth-frequency is placed outside of the signal band. By comparing the results in Table 6.13 to those for the constant  $B$  assumption in Chapter 5, it can be seen that accounting for the range dependence of the  $B$  parameter in RCMC can lead to a significant improvement in processing. By using a linear scaling with the modified scaling factor,  $\alpha_B$ , the maximum RCMC error does not become noticeable until about thirty degrees squint for L-band and about forty degrees squint for C-band. Furthermore, by including the quadratic scaling factor, the maximum RCMC error is negligible for even the largest values of squint.

### 6.3 Higher Order Chirp Scaling

Another approximation that was made in the derivation of the chirp scaling phase function was that the modified frequency rate,  $K_m$ , was assumed constant in range and equal to its value at the reference range,  $K_{mref}$ . The error in RCMC which results is described in Equation (5.154). Since this error varies as the square of the range-time from the reference trajectory, it cannot be accommodated by a modification to the linear scale factor in chirp scaling. To derive a higher

order chirp scaling phase function which can accommodate the range dependence of  $K_m$ , start with the range-Doppler representation of the point scatterer response in Equation (5.153). This expression for  $S(f_\eta, \tau; r)$  includes the slope of the frequency rate in range-time,  $K_s$ , to model the point scatterer response more accurately. Then, let the chirp scaling phase function have a quadratic and a cubic term, with coefficients of  $q_2(f_\eta)$  and  $q_3(f_\eta)$ , respectively. The range-Doppler representation of the chirp scaled signal is then

$$S_\alpha(f_\eta, \tau; r) = S(f_\eta, \tau; r) \exp[-j\pi q_2(\tau - \tau_{ref})^2 - j\frac{2\pi}{3}q_3(\tau - \tau_{ref})^3]. \quad (6.175)$$

Now, the coefficients of the chirp scaling phase function which achieve the desired trajectory are determined in the same way as  $q_2(f_\eta)$  was found in Equation (3.94). The chirp scaled signal is first Fourier transformed in range. The evaluation of the transform using the method of stationary phase is approximated by assuming that the cubic phase term in the integrand is small, as shown in Appendix B. In the resulting SAR transfer function of the chirp scaled signal, the phase term corresponding to RCMC is used to find the scaled trajectory:

$$\begin{aligned} \hat{\tau}_s(f_\eta; r) = & \tau_{ref}(f_\eta) + \frac{K_{mref}}{K_{mref} + q_2} \Delta\tau(f_\eta; r) \\ & + \left[ \frac{K_s}{(K_{mref} + q_2)} - \frac{K_s K_{mref}}{(K_{mref} + q_2)^2} - \frac{q_3 K_{mref}^2}{(K_{mref} + q_2)^3} \right] \Delta\tau^2(f_\eta; r). \end{aligned} \quad (6.176)$$

The use of  $K_s$  in the signal model, along with the higher order term in the chirp scaling phase function, have introduced a higher order term in  $\Delta\tau(f_\eta; r)$  in the representation of the scaled trajectory. It is desired that this scaled trajectory match the desired trajectory in Equation (6.174) as closely as possible. Thus, Equations (6.176) and (6.174) can be compared and the terms equated. This gives two equations for the coefficients of the chirp scaling phase function,  $q_2$  and  $q_3$ , which can be solved to give:

$$\begin{aligned} q_2(f_\eta) &= K_{mref}(f_\eta)[\alpha_B(f_\eta) - 1] \\ q_3(f_\eta) &= K_s(f_\eta)\alpha_B(f_\eta)[\alpha_B(f_\eta) - 1] - \alpha_B^3(f_\eta)K_{mref}(f_\eta)\beta(f_\eta). \end{aligned} \quad (6.177)$$

These coefficients can be used in higher order chirp scaling to provide more accurate RCMC.

With the above definitions of the chirp scaling coefficients, the range dependence of RCMC is removed, and the SAR transfer function of the chirp scaled signal can be written as:

$$\begin{aligned}
S_{2\alpha}(f_\eta, f_\tau; r_0) = & M\left(\frac{f_\tau - \delta f_\tau}{\alpha_B}\right) \exp[-j2\pi\tau_d(f_{\eta r}; r_0)f_\tau] \\
& \exp[-j2\pi(\tau_{ref}(f_\eta) - \tau_{ref}(f_{\eta r}))f_\tau] \\
& \exp\left[\frac{j\pi f_\tau^2}{\alpha_B K_{mref}} + \frac{j2\pi q_3 f_\tau^3}{3\alpha_B^3 K_{mref}^3}\right] \\
& \exp\left[-j\pi\left(\frac{K_s}{\alpha_B^2 K_{mref}^2} + \frac{2q_3}{\alpha_B^3 K_{mref}^2}\right)\Delta\tau(f_\eta; r)f_\tau^2\right] \\
& F_{ac}(f_\eta; r_0) \exp[j\phi_\Delta(f_\eta; r_0)]. \tag{6.178}
\end{aligned}$$

As in the transfer function in Equation (3.95), the factors of this expression correspond to processing steps and properties of the compressed pulse. The first three factors are the range amplitude spectrum of the compressed pulse, a linear phase factor which gives the scatterer position, and a linear phase factor representing the bulk RCMC. These are similar to the corresponding factors in Equation (3.95). The next exponential corresponds to bulk range compression, including SRC. This contains both a quadratic phase term and a cubic phase term. The quadratic term corresponds to the linear FM pulse with its frequency rate modified by  $\alpha_B$ , while the cubic phase term has been introduced by the higher order term in the chirp scaling phase function. Following the range compression factor is an exponential whose phase is quadratic in  $f_\tau$  and varies linearly with the range-time from reference trajectory,  $\Delta\tau(f_\eta; r)$ . Because of this range dependence, this factor cannot be accommodated in the two-dimensional frequency domain and thus represents a processing error. The first term of this quadratic phase error is due to the range dependence of SRC, and has been investigated in Chapter 5. The second term of the error arises from the higher order term in chirp scaling. Thus, the use of higher order chirp scaling to improve RCMC has an effect on the range dependent quadratic phase error. However, this extra error term is very small compared to the range dependence of SRC. Finally, the last factor in Equation (6.178) represents azimuth compression, which is augmented by the phase correction factor. This is the same as in Equation (3.95), except that

the phase correction is modified by the higher order chirp scaling as follows:

$$\begin{aligned} \phi_{\Delta}(f_{\eta}; r) = & -\pi K_{mref} \left(1 - \frac{1}{\alpha_B}\right) \Delta\tau(f_{\eta}; r)^2 \\ & - \left[ \pi K_{mref} \left(1 - \frac{1}{\alpha_B}\right) \left(1 - \frac{1}{3\alpha_B}\right) - \frac{2\pi}{3} K_{mref} \beta \right] \Delta\tau(f_{\eta}; r)^3. \end{aligned} \quad (6.179)$$

The use of higher order chirp scaling provides accurate RCMC at high squint. However, the phase of the SAR transfer function still contains quadratic phase error terms that correspond to the range dependence of SRC and the effect of the higher order chirp scaling phase function.

## Chapter 7

### Nonlinear FM Chirp Scaling for Range-Variant SRC

#### 7.1 Introduction

The processing errors of the chirp scaling algorithm for high squint SAR were investigated in Chapter 5. It was found that the approximation with the greatest effect on the quality of the point spread function was the assumption of a range-invariant frequency rate in SRC. At a given distance from the reference range, the resulting quadratic phase error in the SAR transfer function causes a rapid degradation of range resolution for large enough squint angles. Thus, the accurate focussing of squint mode SAR data requires the accommodation of the range dependence of SRC.

In the chirp scaling algorithm, the coefficients of the chirp scaling phase function were chosen to remove the range dependence of RCMC. To accommodate the range dependence of SRC, an extra degree of freedom is required in determining the phase of the SAR transfer function of the chirp scaled signal. This chapter describes a solution to this problem in which a small nonlinear FM component is incorporated into the received range signal. It is shown that the interaction of the nonlinear FM with the chirp scaling operation introduces range dependent quadratic phase term, corresponding to a range dependent change in frequency rate.

This is illustrated in Figure 7.30. As in Figure 3.7 in the description of the chirp scaling algorithm, this figure shows a frequency-time diagram of a range line containing two scatterers. In this case, the pulses are dominantly linear FM but also have a nonlinear FM component, which gives a curvature to the frequency-time curves of the pulses. As before, pulses before scaling are indicated by solid curves and pulses after scaling are shown by dotted curves. Also, pulses compress to the point where the frequency-time curve intersects the center frequency

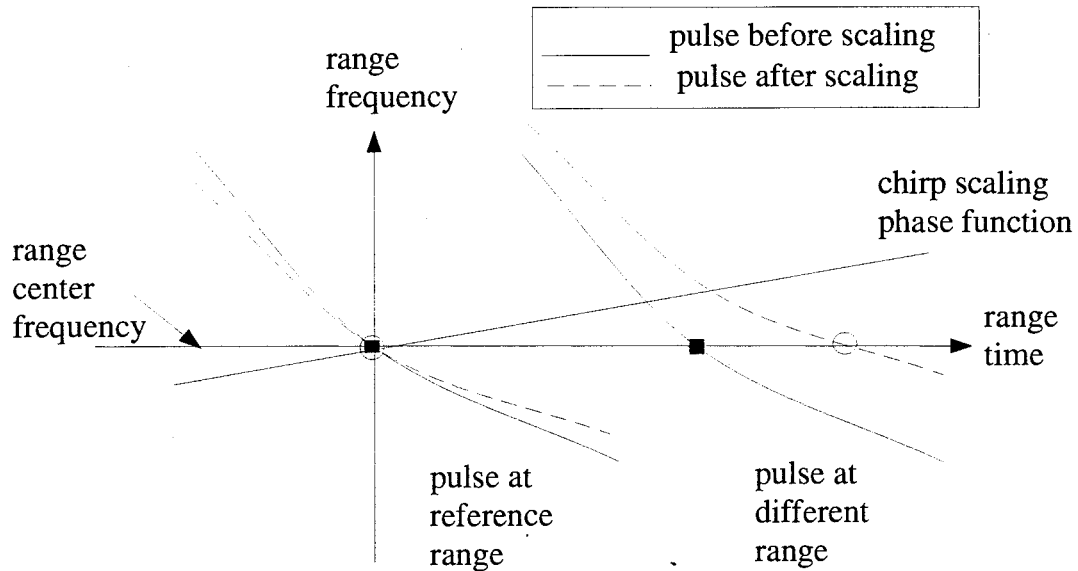


Figure 7.30: Frequency-time diagram of range line with nonlinear FM pulses.

of the range matched filter. In addition, for compression, the frequency rate of the dominant linear FM component of the pulses is determined by the local slope of the curve at the point where the curve intersects the center frequency of the range matched filter. Chirp scaling has the effect of shifting the frequency-time curves so that the point where a curve intersects the center frequency of the range matched filter depends on the distance of the scatterer from the reference range. In this case, because of the curvature introduced by the nonlinear FM component, this also has the effect of changing the local slope of the curves at this point. In this way, the interaction of chirp scaling with a nonlinear FM component in the pulse produces a range dependent frequency rate. Thus, by proper choice of the nonlinear FM component, this can be made to cancel the error due to the range dependence of SRC, thereby achieving accurate focussing for all ranges in the swath.

Two possible approaches to incorporating such a nonlinear FM component in the range signal are proposed. The more accurate approach allows the component to vary with azimuth-frequency. This requires an extra filtering step in the two-dimensional frequency domain, and so will be referred to as the ‘nonlinear FM filtering’ method. Another approach makes the

approximation of assuming that the nonlinear FM component can be calculated at the Doppler centroid and kept constant in azimuth frequency. In this case, the component can be introduced by changing the phase modulation of the transmitted pulse according to the squint angle. Thus the range dependence of SRC can be accommodated without added computation during processing. In a sense, this approach uses the pulse phase modulation as a kind of preprocessing, and will be referred to as the ‘nonlinear FM pulse’ method.

In this chapter, the more accurate nonlinear FM filtering method is first described. The derivation of the nonlinear FM component required to cancel the range dependence of SRC is presented, and the accuracy and limitations of the algorithm are discussed. In addition, it is shown how nonlinear FM chirp scaling can be combined with the use of a higher order chirp scaling phase function, as described in Chapter 6, to perform both RCMC and SRC accurately for scatterers at all ranges. Also, the extra computation required for the nonlinear FM filtering method is discussed. This is followed by a description of the nonlinear FM pulse method, where the accuracy and limitations of this method are investigated. Also, for the nonlinear FM pulse method, consideration is given to the accommodation of an error in the squint estimate used to calculate the transmitted pulse, and to the effect on the method of a Doppler shift in the pulse. Both methods are then investigated by processing simulated high squint data from a point scatterer. Finally, to investigate the algorithm on real data, conventional SAR data are skewed to emulate the data that would be received from a squint mode SAR, and processed with the chirp scaling and nonlinear FM chirp scaling algorithms.

## 7.2 Nonlinear FM Filtering Method

### 7.2.1 Description

For nonlinear FM chirp scaling, a cubic phase term in range-frequency needs to be added to the spectrum of the received signal. Also, to provide accurate processing, the nonlinear FM component should vary with azimuth-frequency. In the nonlinear FM filtering method, this is done by filtering range lines at each azimuth-frequency with a cubic phase filter, before the chirp

scaling phase function is applied in the range-Doppler domain. This filtering step is best done in the range-frequency domain. Thus, compared to the original chirp scaling algorithm, this algorithm requires the extra processing steps of a range FFT, a cubic phase filter multiply in the two-dimensional frequency domain, and a range inverse FFT. After the cubic phase filtering step, the processing steps are the same as in the chirp scaling algorithm, as illustrated in the block diagram in Figure 7.31. As in the chirp scaling algorithm, this algorithm requires only FFT and multiply operations.

To describe the nonlinear FM filtering method, start with the SAR transfer function,  $S_2(f_\eta, f_\tau; r)$ , which corresponds to the received data from a point scatterer after the azimuth FFT and the range FFT steps in Figure 7.31. The cubic phase filtering step is then represented by

$$S_{2Y}(f_\eta, f_\tau; r) = S_2(f_\eta, f_\tau; r) \exp[j\frac{2\pi}{3}Y(f_\eta)f_\tau^3], \quad (7.180)$$

where  $Y(f_\eta)$  is the azimuth-frequency varying cubic phase coefficient, and  $S_{2Y}(f_\eta, f_\tau; r)$  is the filtered signal spectrum. In the expansion of the phase of the SAR transfer function in Equation (3.51), the cubic phase term represented by  $\phi_3(f_\eta; r)$  may be significant at high squint angles and should also be included in the SAR signal representation for nonlinear FM chirp scaling. However, this term is still small enough that its range dependence can be safely neglected, so it will be approximated by  $\phi_3(f_\eta; r_{ref})$ . Also, the definitions of the azimuth compression filter, range migration trajectory, and modified range frequency rate that were used in Chapter 3 can be used in representing the filtered signal spectrum:

$$S_{2Y}(f_\eta, f_\tau; r) = F_{ac}(f_\eta; r)M(f_\tau) \exp[-j2\pi\tau_d(f_\eta; r)f_\tau] \quad (7.181)$$

$$\exp[j\pi\frac{f_\tau^2}{K_m(f_\eta; r)}] \exp[j(\frac{2\pi}{3}Y(f_\eta) + \phi_3(f_\eta; r_{ref}))f_\tau^3]. \quad (7.182)$$

In this expression, the cubic phase term from the SAR transfer function,  $\phi_3$ , can be combined with the cubic phase filter coefficient,  $Y(f_\eta)$ , to define a modified coefficient as follows:

$$\frac{2\pi}{3}Y_m(f_\eta) = \frac{2\pi}{3}Y(f_\eta) + \phi_3(f_\eta; r_{ref}). \quad (7.183)$$

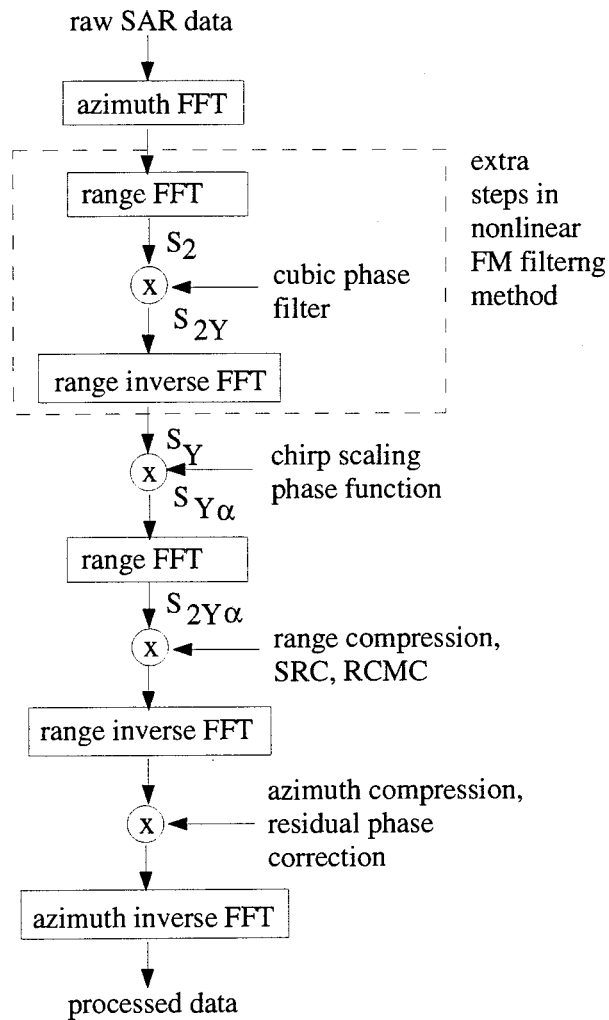


Figure 7.31: Block diagram of nonlinear FM filtering method.

The modified coefficient,  $Y_m(f_\eta)$ , determines the nonlinear FM component that interacts with chirp scaling.

Following the filtering step in the two-dimensional frequency domain, an inverse Fourier transform of  $S_{2Y}(f_\eta, f_\tau; r)$  with respect to  $f_\tau$  is required to take the data to the range-Doppler domain. To simplify the evaluation of the transform, an approximation to the method of stationary phase is used, as described in Appendix A, in which it is assumed that the cubic phase coefficient is small. This leads to the following condition on  $Y_m$ :

$$|Y_m| \ll \frac{1}{|2K_m^2 T_m|}, \quad (7.184)$$

where  $T_m$  is the length of a pulse in the range-Doppler domain, and is defined in Equation (3.61). In addition, when representing the range-Doppler domain signal, the range dependence of the range frequency rate is modelled by  $K_s$ . Thus, the range-Doppler representation of the filtered signal is:

$$\begin{aligned} S_Y(f_\eta, \tau; r) &= F_{ac}(f_\eta; r) m \left[ \frac{K_{mref}}{K} (\tau - \tau_d) + \frac{Y_m K_{mref}^3}{K} (\tau - \tau_d)^2 \right] \\ &\quad \exp[-j\pi(K_{mref} + K_s \Delta\tau)(\tau - \tau_d)^2] \\ &\quad \exp[-j\frac{2\pi}{3} Y_m (K_{mref} + K_s \Delta\tau)^3 (\tau - \tau_d)^3]. \end{aligned} \quad (7.185)$$

This expression has the same form as the range-Doppler representation shown earlier in Equation (5.153), except that a cubic phase term has been added to the pulse. Also, the pulse amplitude in the range-Doppler domain is shifted slightly in range time because of the extra quadratic range-time term in its argument. However, if  $|Y_m|$  is less than just half of the bound shown in Equation (7.184), then the range-time shift in the pulse is only a few percent of the pulse length, and thus does not significantly affect processing.

The next step is the multiplication of the signal by the chirp scaling phase function. To achieve the desired trajectory, a higher order phase function like the one derived in Chapter 6 is used. However, in this case the coefficients of the phase function,  $q_2$  and  $q_3$ , will depend on the nonlinear FM component, since this affects how chirp scaling shifts the scatterer trajectories.

The multiplication of the filtered signal by the chirp scaling phase function is represented as:

$$S_{Y\alpha}(f_\eta, \tau; r) = S_Y(f_\eta, \tau; r) \exp[-j\pi q_2(f_\eta)(\tau - \tau_{ref})^2 - j\frac{2\pi}{3}q_3(f_\eta)(\tau - \tau_{ref})^3]. \quad (7.186)$$

After chirp scaling,  $S_{Y\alpha}(f_\eta, \tau; r)$  is Fourier transformed with respect to  $\tau$  to get the SAR transfer function of the filtered, chirp scaled signal. Again, the stationary point is approximated by assuming the cubic phase coefficient is small, as shown in Appendix B. The effect of assuming a small cubic phase coefficient on processing accuracy will be investigated in the next subsection.

Given the phase terms in the resulting SAR transfer function, the nonlinear FM component and the chirp scaling coefficients can be chosen to remove the range dependence of RCMC and SRC. The phase term corresponding to RCMC gives an expression for the scaled trajectory,  $\hat{\tau}_s(f_\eta; r)$ , as a function of  $\Delta\tau(f_\eta; r)$ . To remove the range dependence of RCMC, the  $\Delta\tau$  and  $\Delta\tau^2$  terms in  $\hat{\tau}_s(f_\eta; r)$  are equated to the terms corresponding to the linear and quadratic scaling factors in the desired trajectory in Equation (6.174). In addition, the range dependent quadratic phase term corresponding to the SRC error, which is linear in  $\Delta\tau(f_\eta; r)$ , is set to zero. This gives a set of three equations for the coefficients,  $q_2$ ,  $q_3$ , and  $Y_m$ . The first equation gives the relationship between the linear scale factor,  $\alpha_B$ , and the quadratic coefficient of the chirp scaling phase function,  $q_2$ :

$$\frac{K_{mref}}{K_{mref} + q_2} = \frac{1}{\alpha_B}. \quad (7.187)$$

Then, given  $\alpha_B$ , the next two equations can be solved simultaneously for  $q_3$  and  $Y_m$ :

$$\begin{aligned} \frac{1}{\alpha_B^3 K_{mref}} [K_s \alpha_B (\alpha_B - 1) - Y_m K_{mref}^3 (\alpha_B - 1)^2 - q_3] &= \beta \\ \frac{1}{\alpha_B^3 K_{mref}^2} \left[ \frac{\alpha_B K_s}{2} - Y_m K_{mref}^3 (\alpha_B - 1) + q_3 \right] &= 0. \end{aligned} \quad (7.188)$$

The solution to these equations gives the following expressions for the chirp scaling coefficients and the nonlinear FM component:

$$\begin{aligned} q_2 &= K_{mref}(\alpha_B - 1) \\ q_3 &= \frac{K_s(\alpha_B - 1)}{2} - \alpha_B^2 K_{mref} \beta \\ Y_m &= \frac{K_s(\alpha_B - 0.5) - \alpha_B^2 K_{mref} \beta}{K_{mref}^3 (\alpha_B - 1)}. \end{aligned} \quad (7.189)$$

The cubic phase filter coefficient,  $Y(f_\eta)$ , is then found from Equation (7.183). The coefficients  $q_2(f_\eta)$ ,  $q_3(f_\eta)$ , and  $Y(f_\eta)$ , define a nonlinear FM chirp scaling algorithm which accommodates the range dependence of RCMC and SRC for high squint angles.

In the nonlinear FM filtering method, the SAR transfer function of the filtered, chirp scaled signal then becomes

$$\begin{aligned}
 S_{2Y\alpha}(f_\eta, f_\tau; r) = & M\left(\frac{f_\tau - \delta f_\tau}{\alpha_B}\right) \exp[-j2\pi\tau_d(f_{\eta r}; r)f_\tau] \\
 & \exp[-j2\pi(\tau_{ref}(f_\eta) - \tau_{ref}(f_{\eta r}))f_\tau] \\
 & \exp\left[\frac{j\pi f_\tau^2}{\alpha_B K_{mref}} + \frac{j2\pi(q_3 + Y_m K_{mref}^3)f_\tau^3}{3\alpha_B^3 K_{mref}^3}\right] \\
 & F_{ac}(f_\eta; r) \exp[j\phi_\Delta(f_\eta; r)]. \tag{7.190}
 \end{aligned}$$

The first factor is the range amplitude spectrum of the compressed pulse. Note that since the nonlinear FM component was introduced by a phase multiply in the frequency domain, it does not affect the range amplitude spectrum. Also, in representing the effect on the amplitude spectrum of the chirp scaling phase function multiply, the small higher order scaling coefficient has been ignored. The next two factors, as in Equations (6.178) and (3.95), correspond to the scatterer position, and the bulk RCMC. Following these is an exponential factor which contains quadratic and cubic phase terms in  $f_\tau$ , and corresponds to bulk range compression including SRC. As in Equation (6.178), the quadratic phase term corresponds to the linear FM component of the range signal, with its frequency rate modified by  $\alpha_B$ . The cubic phase term, in this case, results from both the higher order chirp scaling phase function and the nonlinear FM component. Compared to Equation (6.178), the range dependent quadratic phase error has been removed, and the application of the range matched filter provides accurate focussing for scatterers at all ranges. Finally, the last two factors correspond to azimuth compression and the phase correction, where now the phase correction is given by:

$$\begin{aligned}
 \phi_\Delta(f_\eta; r) = & -\pi K_{mref}\left(1 - \frac{1}{\alpha_B}\right)\Delta\tau(f_\eta; r)^2 \\
 & -\left[\frac{\pi K_s}{3}\left(1 - \frac{1}{\alpha_B}\right) - \frac{2\pi}{3}K_{mref}\beta(2 - \alpha_B)\right]\Delta\tau(f_\eta; r)^3. \tag{7.191}
 \end{aligned}$$

### 7.2.2 Limitations

Chirp scaling shifts scatterer trajectories to the desired trajectory. However, at the reference azimuth-frequency these two trajectories intersect, so no scaling is actually required. That is,  $\alpha_B(f_{\eta r}) = 1$  and  $\beta(f_{\eta r}) = 0$ , so that the coefficients of the chirp scaling phase function for this range line,  $q_2(f_{\eta r})$  and  $q_3(f_{\eta r})$ , are both zero. In nonlinear FM chirp scaling, then, there is no chirp scaling effect to interact with the nonlinear FM component at this range line. This can also be seen from the expression for the cubic phase coefficient in Equation (7.189), which becomes very large as  $\alpha_B$  approaches one. Thus, for nonlinear FM chirp scaling to work, the reference azimuth-frequency must be placed outside of the azimuth-frequency band of the signal. This increases the maximum amount of scaling that takes place across the signal band, thus increasing the side-effects of chirp scaling.

Some approximations in the derivation of the algorithm become more accurate as the size of the cubic phase coefficient decreases – that is, as the condition in Equation (7.184) is more strongly satisfied. As defined in Equation (7.189),  $Y_m$  depends on the scaling factors,  $\alpha_B$  and  $\beta$ , and on the slope of the range frequency rate. The scaling factors are affected by the choice of the reference azimuth-frequency, so that the condition on the cubic phase coefficient can be used to derive a constraint on  $f_{\eta r}$ . Using the definition of  $Y_m$ , Equation (7.184) can be shown to be approximately equivalent to:

$$|f_\eta - f_{\eta r}| \gg \left| \frac{KT f_{\eta r}}{f_0} \right|, \quad (7.192)$$

for all azimuth-frequencies,  $f_\eta$ , in the signal band. Then, recall from Equations (5.144) and (5.145) that the side-effects of chirp scaling, consisting of a change in range bandwidth and a range-frequency shift, both increase with  $|f_\eta - f_{\eta r}|$ . Thus, by ensuring a small cubic phase coefficient, the side-effects of chirp scaling are increased, and this tradeoff must be investigated to determine the limitations of the algorithm. It remains to find out how small the cubic phase coefficient needs to be in order to achieve accurate processing, and this requires an expression for the processing errors in nonlinear FM chirp scaling.

To represent the processing errors, higher order phase terms in the SAR transfer function of the chirp scaled signal are found by approximating the stationary point more accurately. First, the filtered signal spectrum,  $S_{2Y}(f_\eta, f_\tau; r)$ , is inverse transformed in range to obtain the range-Doppler representation of the signal. In Appendix A, the higher order terms are included in the approximation to the method of stationary phase, giving the more accurate representation of the signal:

$$\begin{aligned}
S_Y(f_\eta, \tau; r) = & F_{ac}(f_\eta; r)m\left[\frac{K_{mref}}{K}(\tau - \tau_d) + \frac{Y_m K_{mref}^3}{K}(\tau - \tau_d)^2\right] \\
& \exp[-j\pi(K_{mref} + K_s\Delta\tau)(\tau - \tau_d)^2] \\
& \exp[-j\frac{2\pi}{3}Y_m(K_{mref} + K_s\Delta\tau)^3(\tau - \tau_d)^3] \\
& \exp[-j\pi Y_m^2(K_{mref} + K_s\Delta\tau)^5(\tau - \tau_d)^4]. \tag{7.193}
\end{aligned}$$

This form of the signal includes a higher order phase term, with a  $Y_m^2$  coefficient, due to the higher order term in the approximation of the stationary point. Also, the range dependence of  $K_m$  is modelled by its slope in range-time,  $K_s$ . The cubic coefficient,  $Y_m$  is assumed range-invariant. The chirp scaling phase function is applied to this signal, and higher order terms in  $f_\tau$  and  $\Delta\tau$  are maintained while finding the range Fourier transform, as shown in Appendix B. In the resulting SAR transfer function, this introduces extra phase terms compared to the expression in Equation (7.190), which are not taken into account during processing. Thus, they represent processing errors due to approximations made in deriving the algorithm. The phase error in the SAR transfer function is as follows:

$$\begin{aligned}
\phi_{err}(f_\eta, f_\tau; r) = & \pi c_4 f_\tau^4 \\
& -2\pi(2K_{mref}c_4 + c_3)\Delta\tau f_\tau^3 \\
& +2\pi(3K_{mref}^2c_4 + 3K_{mref}c_3 - c_2)\Delta\tau^2 f_\tau^2 \\
& -2\pi(2K_{mref}^3c_4 + 3K_{mref}^2c_3 - 2K_{mref}c_2 - c_1)\Delta\tau^3 f_\tau, \tag{7.194}
\end{aligned}$$

where the coefficients in this expression,  $c_1$  to  $c_4$ , are given by:

$$c_4 = \frac{(q_3 + Y_m K_{mref}^3)^2 - \alpha_B Y_m^2 K_{mref}^6}{\alpha_B^5 K_{mref}^5}$$

$$\begin{aligned}
c_3 &= \frac{(q_3 - (\alpha_B - 1)Y_m K_{mref}^3)(K_s - 2Y_m K_{mref}^3)}{\alpha_B^4 K_{mref}^4} \\
c_2 &= \frac{(q_3 - (3\alpha_B - 1)Y_m K_{mref}^3)(K_s - Y_m K_{mref}^3) - \frac{1}{2}(K_s - 2Y_m K_{mref}^3)^2}{\alpha_B^3 K_{mref}^3} \\
c_1 &= \frac{3\alpha_B Y_m K_{mref}^3 (K_s - \frac{2}{3}Y_m K_{mref}^3) + (K_s - Y_m K_{mref}^3)(K_s - 2Y_m K_{mref}^3)}{\alpha_B^2 K_{mref}^2}. \quad (7.195)
\end{aligned}$$

Each of the phase error terms in Equation (7.194) corresponds to a higher power of  $f_\tau$  and a higher order of variation in  $\Delta\tau$  than is accommodated in nonlinear FM chirp scaling. Note that errors arise from both the size of the cubic coefficient, and from higher order range dependencies in RCMC and SRC than are accommodated in the algorithm. In particular, the fourth power and cubic phase errors are more sensitive to the size of  $Y_m$ , and hence to the condition in Equation (7.184). The quadratic and linear phase errors (RCMC and SRC errors) are more range dependent.

The significance of these errors as a function of squint angle is shown for spaceborne SAR parameters in Table 7.14 for L-band and Table 7.15 for C-band. These show the maximum phase error for the 4'th power, cubic, and quadratic phase errors, and the maximum RCMC error for a scatterer at 20 km from the reference range. Also, the reference azimuth-frequency was chosen so that the condition

$$|Y_m| < \frac{0.5}{|2K_m^2 T_m|} \quad (7.196)$$

holds for all frequencies in the signal band. Thus the condition in Equation (7.184) is only weakly satisfied. As can be seen from the tables, however, this is enough to keep the maximum phase errors less than 90 degrees and the maximum RCMC error less than a tenth of a cell. Thus, the processing errors at high squint are sufficiently small.

Next, for the same value of reference azimuth-frequency that was used to calculate the above processing errors, the side-effects of chirp scaling were investigated for different squint angles. Table 7.16 shows the percent change in range bandwidth, and the range-frequency shift as a percentage of the range bandwidth, for spaceborne SAR parameters at L-band and C-band. Also, as above, the scatterer was assumed to be at the edge of the range swath, 20 km from

	L-band			
squint	4'th power phase error (degrees)	cubic phase error (degrees)	quadratic phase error (degrees)	RCMC error (cells)
10	0.4	0.0	0.3	0.00
20	2.9	0.4	4.0	0.00
30	12.6	3.2	20.1	0.01
40	55.6	18.5	71.9	0.06

Table 7.14: Maximum phase and RCMC errors for nonlinear FM chirp scaling.

	C-band			
squint	4'th power phase error (degrees)	cubic phase error (degrees)	quadratic phase error (degrees)	RCMC error (cells)
10	0.1	0.0	0.1	0.00
20	0.6	0.1	0.3	0.00
30	1.8	0.2	1.9	0.00
40	6.1	1.0	10.2	0.01
50	28.9	7.1	54.2	0.06

Table 7.15: Maximum phase and RCMC errors for nonlinear FM chirp scaling.

the reference range. The side-effects vary slightly across the interval of azimuth-frequency that is used in processing, and the values shown in the table are the maximum change in range bandwidth and range-frequency shift across the azimuth band. The change in bandwidth and frequency shift that can be tolerated depends on the width of the window in the range matched filter, and on the range oversampling rate. To avoid aliasing, the fractional change in bandwidth should be sufficiently less than the oversampling rate, which is typically about twenty percent. As can be seen from the table, the worst case change in bandwidth is sufficiently less than the oversampling rate, so this is not a problem. To accommodate some frequency shift, the window in the range matched filter should be wider than the nominal range bandwidth, but of course cannot be wider than the sampling rate. The range frequency shift, combined with the change in bandwidth, may be enough to take some frequency components outside of the window. This results in a loss of range bandwidth, leading to a loss of range resolution and signal energy. To keep frequency components within the fundamental interval of range-frequency, the side-effects must satisfy the condition:

$$\frac{(\alpha_B - 1)}{2} + \frac{\delta f_\tau}{\Delta f_\tau} < \frac{os}{2}, \quad (7.197)$$

where  $\delta f_\tau$  is the frequency shift,  $\Delta f_\tau$  is the range bandwidth,  $(\alpha_B - 1)$  is the fractional change in bandwidth, and  $os$  is the oversampling rate. Given an oversampling rate of about twenty percent, this condition is satisfied by the worst case frequency shifts described in Table 7.16, so the side-effects of chirp scaling have a negligible effect on processing with this method. Thus, the nonlinear FM filtering method can achieve accurate processing for squint angles up to the limitations imposed by the SAR imaging constraints and the signal model, which were discussed earlier in Chapter 4.

### 7.2.3 Computation

In describing the nonlinear FM filtering method, the extra computation that is required should be compared to other approaches. First, since this algorithm is an extension of chirp scaling,

squint	% increase in bandwidth		frequency shift (% of bandwidth)	
	L-band	C-band	L-band	C-band
10	0.7	0.2	2.5	0.7
20	1.7	0.4	4.9	1.6
30	3.3	0.8	6.5	2.9
40	6.3	1.6	7.3	4.6
50		3.4		6.7

Table 7.16: Percent change in range bandwidth and percent range-frequency shift due to chirp scaling with nonlinear FM filtering method.

the computation of the chirp scaling algorithm should be mentioned. Compared to the range-Doppler algorithm, the chirp scaling algorithm requires fewer arithmetic operations since RCMC is done with a phase multiply rather than an interpolator. If corner turning is required, the chirp scaling algorithm requires two extra corner turns. However, for higher squint, the chirp scaling algorithm should be compared to the squint imaging mode algorithm, which also accommodates the azimuth-frequency dependence of SRC. In this case, the number of corner turns in each algorithm is the same, while the chirp scaling algorithm performs RCMC more efficiently.

Next, consider the nonlinear FM filtering method, which requires the extra computation of a frequency domain filtering step in addition to the computation required by the chirp scaling algorithm. To evaluate this algorithm, note that since the purpose of the nonlinear FM filtering step is the accommodation of the range dependence of SRC, an alternative to this step is the use of a time domain, range-variant filter which performs residual SRC in the range-Doppler domain. Such a filter would be applied after azimuth-frequency dependent SRC was done in the two-dimensional frequency domain, so that only the range dependence of SRC is accommodated. In general, range-variant, time domain filtering is more difficult to implement than FFT's and multiplies, so that the nonlinear FM filtering method is advantageous from this point of view. However, the number of operations can also be compared between the two approaches. For a range line with  $N$  samples, the number of complex multiplications for the nonlinear FM filtering

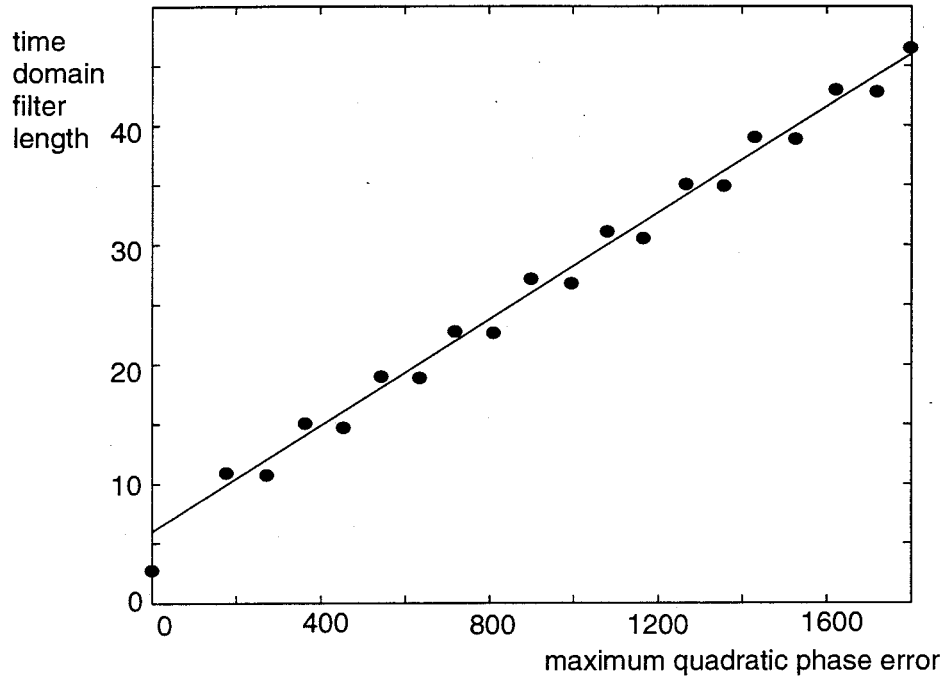


Figure 7.32: Time domain filter length required for less than 3 percent broadening, versus maximum quadratic phase error in degrees.

step (consisting of a range FFT, range multiply, and range inverse FFT) is:

$$n_{ops} = 2\left(\frac{N}{2} \log_2(N)\right) + N. \quad (7.198)$$

The number of operations for the time domain filter depends the number of filter coefficients, and this in turn depends on the compression error being compensated. Thus, it is first necessary to know the time domain filter length needed for a given compression error. This was determined by simulating a compressed pulse with a given maximum quadratic phase error, and then finding the time domain filter length which resulted in a final resolution broadening of less than 3 percent. Figure 7.32 shows a graph of the required filter length,  $l$ , versus the absolute value of quadratic phase error,  $\phi_{max}$ . Also shown is a line that fits the points, which is given by

$$l = 6 + \frac{\phi_{max}}{45}, \quad (7.199)$$

for  $\phi_{max}$  given in degrees. Then, the fact that the compression error varies across the range line needs to be taken into account. The quadratic phase error due to the range dependence

of SRC is given in Equation (5.155). In this expression let  $m$  be the number of samples from the reference range, so that  $\Delta\tau = m/f_{sr}$ , where  $f_{sr}$  is the range sampling rate. The maximum quadratic phase error at sample  $m$  can then be expressed as

$$\phi_{max} = \phi_s m, \quad (7.200)$$

where  $\phi_s$  is the slope of the phase error per sample:

$$\phi_s = 180 \frac{|K_s|}{\alpha_B^2 K_{mref}^2} \frac{\Delta f_\tau^2}{4 f_{sr}}. \quad (7.201)$$

The total number of operations for the range line is the sum of the operations for all range samples. Assuming the reference range is at midswath, then, the number of complex multiplications required in the time domain filtering approach can be shown to be:

$$n_{ops} = 6N + \frac{\phi_s N^2}{180}. \quad (7.202)$$

Because of the appearance of  $K_s$ ,  $K_{mref}$ , and  $\alpha_B$  in the definition of  $\phi_s$ , the amount of computation in the time domain SRC approach depends on the wavelength and the squint angle. Figure 7.33 compares the computation of time domain residual SRC with that of the frequency domain cubic phase filtering step. Each of the graphs in this figure shows a plot of the number of complex multiplications versus the number of samples in the range line. The top graph shows the results for L-band, and the bottom graph shows the results for C-band. As can be seen, the number of operations in each approach is comparable. The nonlinear FM filtering approach requires slightly more operations than the time domain approach for moderate squint angles, and requires about half the computation of residual SRC at high squint. This, combined with the ability to implement nonlinear FM filtering using FFT's and multiplies, makes it an attractive approach for high squint SAR processing.

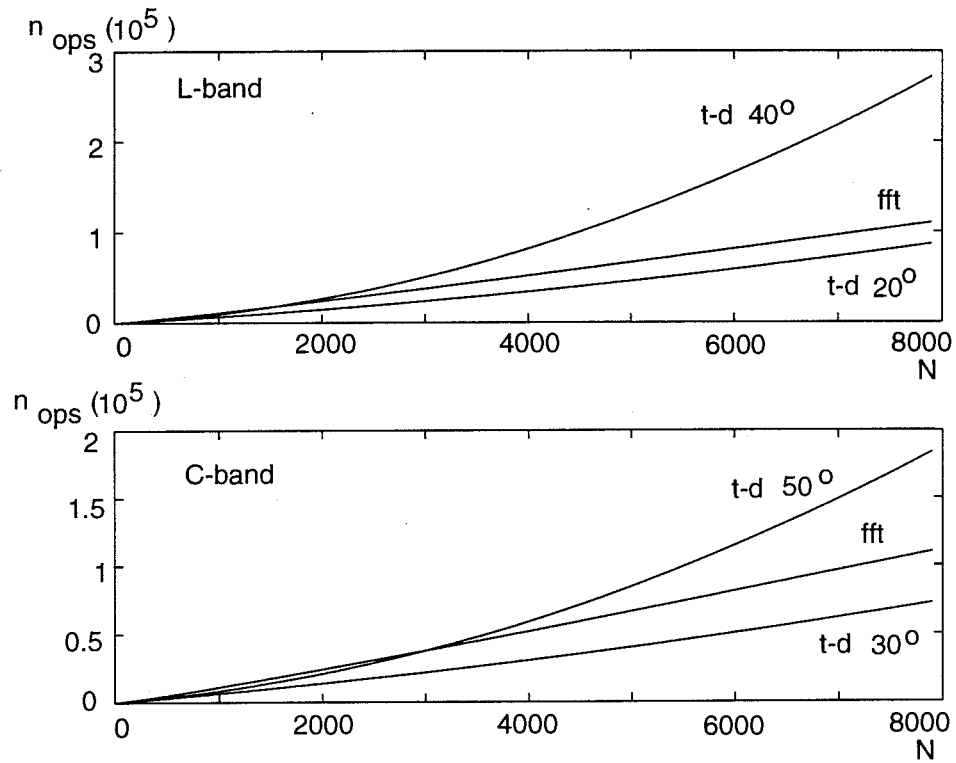


Figure 7.33: Computation of time domain SRC filter (t-d) versus frequency domain cubic phase filtering step (fft). Top: L-band SAR at squint angles of 20 and 40 degrees. Bottom: C-band SAR at squint angles of 30 and 50 degrees.

### 7.3 Nonlinear FM Pulse Method

#### 7.3.1 Description and Limitations

To avoid an increase in computation over that of the chirp scaling algorithm, the nonlinear FM component can be incorporated directly into the transmitted pulse. However, this requires the approximation that the nonlinear FM component be constant in azimuth-frequency. To minimize the error due to this approximation, the component should be calculated at the Doppler centroid. Thus, this requires the phase modulation of the transmitted pulse to be modified according to the squint angle. This approach is feasible given digital signal generation and an estimate of the squint angle from the attitude control of the antenna.

To determine the value of the nonlinear FM component in this case, the required cubic phase coefficient of the SAR transfer function, as defined in Equation (7.189), is evaluated at the Doppler centroid. Then, from Equation (7.183), the corresponding cubic phase filter coefficient is determined:

$$Y_c = Y_m(f_{\eta c}) - \frac{3\phi_3(f_{\eta c}; r_{ref})}{2\pi}. \quad (7.203)$$

It is desired to obtain the same effect on the signal as was obtained by filtering with the cubic phase filter, except with the approximation of using a filter coefficient that is constant in azimuth-frequency,  $Y_c$ . This can be done by using a transmitted pulse with a cubic phase term in the phase modulation, as follows:

$$p(\tau) = m(\tau + Y_c K^2 T^2 / 4) \exp[-j\pi K \tau^2 - j\frac{2\pi}{3} Y_c K^3 \tau^3]. \quad (7.204)$$

In the pulse the amplitude is shifted by a small amount that depends on the cubic phase coefficient, in order to span the same interval of instantaneous range-frequency as in the linear FM case. Using this transmitted pulse, the two-dimensional Fourier transform of the received SAR signal can be shown to be

$$S_{2Y_c}(f_\eta, f_\tau; r) = F_{ac}(f_\eta; r) M(f_\tau) \exp[-j2\pi\tau_d(f_\eta; r) f_\tau] \quad (7.205)$$

$$\exp[j\pi \frac{f_\tau^2}{K_m(f_\eta; r)}] \exp[j(\frac{2\pi}{3} Y_c + \phi_3(f_\eta; r_{ref})) f_\tau^3]. \quad (7.206)$$

This expression is the same as the filtered signal in Equation (7.182), except for the constant coefficient,  $Y_c$ . Finally, as before, the cubic term of the SAR focussing phase,  $\phi_3(f_\eta; r_{ref})$ , should be accounted for. This term can be combined with  $Y_c$  to produce the modified cubic phase coefficient of the SAR transfer function that interacts with chirp scaling:

$$\frac{2\pi}{3}Y_{mc}(f_\eta) = \frac{2\pi}{3}Y_c + \phi_3(f_\eta; r_{ref}). \quad (7.207)$$

This modified coefficient  $Y_{mc}(f_\eta)$  plays the same role as  $Y_m(f_\eta)$  did in the nonlinear FM filtering method, although it will not be accurate for azimuth-frequencies other than the Doppler centroid.

With the SAR data collected with the nonlinear FM pulse in Equation (7.204), the processing follows the same steps as the chirp scaling algorithm. The only differences from the original chirp scaling algorithm that result from using this approach are the choice of the reference azimuth-frequency, and the fact that the chirp scaling phase function coefficients are the ones used in the nonlinear FM filtering method described above. The approximation of using a cubic phase coefficient that is constant in azimuth-frequency has a negligible effect on RCMC. However, the ability to remove the range dependent quadratic phase error is impaired at azimuth-frequencies other than the Doppler centroid. Thus, in the SAR transfer function of the chirp scaled signal, a range and azimuth-frequency dependent quadratic phase error appears. This error is zero at the Doppler centroid and increases toward the edges of the azimuth-frequency band. By substituting the definition of  $Y_{mc}$  for  $Y_m$  in the expression for the range dependent quadratic phase term in the SAR transfer function, the phase error due to the approximation in the nonlinear FM pulse method can be shown to be:

$$\phi_{err}(f_\eta, f_\tau; r) = -2\pi \frac{K_{mref}(\alpha_B - 1)\Delta\tau(f_\eta; r)}{\alpha_B^3} (Y(f_\eta) - Y_c) f_\tau^2. \quad (7.208)$$

By using the definitions of  $\alpha_B(f_\eta)$  and  $Y_m(f_\eta)$ , this error can be shown to be approximately:

$$\phi_{err}(f_\eta, f_\tau; r) \approx \frac{\pi K_s \Delta\tau(f_\eta; r) (f_\eta - f_{\eta c}) f_\tau^2}{\alpha_B^3 K_{mref}^2 (f_{\eta c} - f_{\eta r})}. \quad (7.209)$$

Note that because of the  $(f_{\eta c} - f_{\eta r})$  term in the denominator, the error can be made to decrease by choosing a greater azimuth-frequency offset between the reference and the Doppler centroid.

However, the side-effects of chirp scaling increase with this offset. This indicates a tradeoff between the side-effects of chirp scaling and the focussing error due to the approximation in this method.

Since the phase error varies across the azimuth-frequency band, the resulting broadening of the range compressed pulses increases towards the edges of the band. After azimuth compression, this broadening is averaged in azimuth to get an overall range broadening in the point spread function. This is similar to the effect of the approximation in the range-Doppler algorithm, in which SRC is calculated at the Doppler centroid. This focussing error can be characterized by the maximum phase error of the SAR transfer function in the two-dimensional frequency domain, which is the maximum quadratic error in range-frequency, evaluated at the edges of the azimuth-frequency band. To keep the overall broadening to less than five percent, this maximum phase error should be less than about 120 degrees [44].

To investigate the tradeoff between side-effects and focussing error as a function of squint angle, Tables (7.17) and (7.18) show the change in range bandwidth, range-frequency shift, and maximum phase error due to the approximation in this method. The results are presented for spaceborne SAR parameters at L-band and C-band, with the scatterer at the edge of the swath where  $(r - r_{ref}) = 20 \text{ km}$ . Also, to achieve an acceptable level of error, the azimuth-frequency offset from the reference,  $|f_{\eta c} - f_{\eta r}|$ , has to be increased compared to the value used in the nonlinear FM filtering method. This corresponds to ensuring that the constraint in Equation (7.184) is more strongly satisfied. In this case, for each squint angle,  $f_{\eta r}$  was chosen so that the condition

$$|Y_m| < \frac{0.2}{|2K_m^2 T_m|} \quad (7.210)$$

was satisfied across the azimuth-frequency band. The side-effects vary across the azimuth-frequency band, and the table shows the maximum change in bandwidth and frequency shift. For L-band, the processing error and increased side-effects in this method start to become noticeable at thirty degrees squint, although performance is still acceptable. For C-band, the side-effects and errors in this approach become noticeable at about forty degrees squint. Thus,

L-band			
squint (degrees)	% bandwidth change	frequency shift (% of bandwidth)	maximum phase error (degrees)
10	0.9	3.1	25.5
20	2.5	7.0	71.2
30	4.2	10.4	123.6
40	9.0	12.6	177.5

Table 7.17: Side-effects of chirp scaling and error due to approximation in the nonlinear FM pulse method: Change in range bandwidth, range-frequency shift, and maximum quadratic phase error at azimuth band edge.

C-band			
squint (degrees)	% bandwidth change	frequency shift (% of bandwidth)	maximum phase error (degrees)
10	0.2	0.9	7.3
20	0.6	2.4	21.5
30	1.4	5.0	43.1
40	2.9	8.6	80.3
50	6.7	13.3	158.5

Table 7.18: Side-effects of chirp scaling and error due to approximation in the nonlinear FM pulse method: Change in range bandwidth, range-frequency shift, and maximum quadratic phase error at azimuth band edge.

although the nonlinear FM pulse method is not as accurate as the nonlinear FM filtering method, it can still achieve good focussing performance at high squint.

### 7.3.2 Accommodation of Error in Squint Estimate

In the nonlinear FM pulse method, the determination of the phase modulation of the transmitted pulse in Equation (7.204) requires a knowledge of the Doppler centroid, which in turn requires an accurate knowledge of the squint angle. However, in spaceborne SAR, the antenna pointing direction can only be measured to within half of a degree or so, and a more accurate

estimate of the Doppler centroid is obtained using the received data during processing [26]. Thus, an initial, inaccurate estimate of the Doppler centroid is used to calculate the cubic phase coefficient of the transmitted pulse. If chirp scaling proceeds without accounting for this erroneous coefficient, the accommodation of the range dependence of SRC would be impaired, with a corresponding degradation in image quality. Fortunately, the processing can be modified so that errors in the initial estimate of the Doppler centroid can be accommodated without a significant degradation in performance. To see how this can be done, note that the correct value of  $Y_c$  depends not only on the Doppler centroid, but also on the value of  $f_{\eta r}$  that is used during chirp scaling. Note that while an initial value of reference azimuth-frequency, based on the initial estimate of Doppler centroid, was used to calculate  $Y_c$ , a different value of  $f_{\eta r}$  can be used when processing the data. Thus, a value for  $f_{\eta r}$  can be found such that the cubic coefficient that is required for accurate nonlinear FM chirp scaling, is equal to the one that was actually used in the transmitted pulse.

The appropriate value of  $f_{\eta r}$  can be found as follows. Let the cubic phase coefficient for nonlinear FM chirp scaling, as defined in Equation (7.189), be represented by  $Y_m(f_{\eta c}; f_{\eta r})$ . In this form, the dependence on  $f_{\eta r}$  is due to the presence of the scaling factors,  $\alpha_B$  and  $\beta$ , in the definition of  $Y_m$ . At the Doppler centroid,  $Y_m(f_{\eta c}; f_{\eta r})$  can be thought of as a function of  $f_{\eta r}$ . Thus, given the value of  $Y_c$  that was used in the transmitted pulse, it is required to find the value of  $f_{\eta r}$  that satisfies the equation:

$$Y_m(f_{\eta c}; f_{\eta r}) = Y_{cc}, \quad (7.211)$$

where, to simplify notation,  $Y_{cc}$  is

$$Y_{cc} = Y_c + \frac{3}{2\pi} \phi_3(f_{\eta c}). \quad (7.212)$$

For the case of a constant  $B$  parameter, where  $\alpha_B = \alpha$  and  $\beta = 0$ , Equation (7.211) can be solved explicitly to obtain

$$f_{\eta r} = \sqrt{\frac{4B}{\lambda^2} \left[ 1 - \left( \frac{\gamma(f_{\eta c}; r_{ref}) k_2}{2k_1} \right)^2 \right]}, \quad (7.213)$$

where the terms  $k_1$  and  $k_2$  are defined as

$$k_1 = K_s - Y_{cc}K_{mref}^3 \quad (7.214)$$

$$k_2 = K_s - 2Y_{cc}K_{mref}^3. \quad (7.215)$$

More generally, for a range varying  $B$ , it was found that the required value of  $f_{\eta r}$  can be found very accurately by the following iterative scheme:

1. Pick an initial estimate of reference azimuth-frequency,  $f_{\eta ri}$ . This could be obtained from the initial value of reference azimuth-frequency used in calculating the transmitted pulse, or from Equation (7.213) for  $f_{\eta r}$  assuming a constant  $B$ .
2. Using the definition of  $Y_m$ , write Equation (7.211) as

$$\frac{K_s(\alpha_B - 0.5)}{K_{mref}^3(\alpha_B - 1)} = Y_{cc} + \frac{\alpha_{B_i}^2 \beta_i}{K_{mref}^2(\alpha_{B_i} - 1)}, \quad (7.216)$$

where  $\alpha_{B_i}$  and  $\beta_i$  are calculated using the initial estimate,  $f_{\eta ri}$ . This equation can be solved explicitly for  $\alpha_B$ .

3. Given the value of  $\alpha_B$  found above, use the definitions of  $\alpha_B$  and  $a(f_{\eta r})$  in Equations (6.173) and (6.171) to write the following equation for  $\gamma(f_{\eta r}; r_{ref})$ :

$$\gamma(f_{\eta r}; r_{ref}) = \frac{\alpha_B}{a(f_{\eta c})} \frac{2}{c} \left( 1 - \frac{r_{ref}(1 - \gamma^2(f_{\eta ri}; r_{ref}))B_s}{2\gamma^2(f_{\eta ri}; r_{ref})B_r} \right). \quad (7.217)$$

4. Use the value of  $\gamma(f_{\eta r}; r_{ref})$  found above to solve for a new value of  $f_{\eta r}$ .
5. Replace  $f_{\eta ri}$  with  $f_{\eta r}$  and repeat.

With this scheme it was found that at most four iterations are required to find the required value of  $f_{\eta r}$ . Then, the cubic phase that was used in the transmitted pulse can be used in the nonlinear FM pulse method to accommodate the range dependence of SRC.

Note that the value of  $f_{\eta r}$  required to make use of the transmitted pulse will be slightly different than what would have been used if there were no error in the initial estimate of the

L-band			
squint (degrees)	% bandwidth change	frequency shift (% of bandwidth)	maximum phase error (degrees)
10	0.9	3.2	27.6
20	2.5	7.2	75.6
30	5.5	10.8	133.3
40	11.3	13.2	197.8

Table 7.19: Side-effects and maximum phase error with  $f_{\eta r}$  changed to accommodate a  $\pm 1$  degree squint estimate error.

Doppler centroid. The initial reference azimuth-frequency, used to calculate the transmitted pulse, may have been chosen to achieve acceptable levels of side-effects and focussing error. However, the change in  $f_{\eta r}$  to accommodate the error in squint estimate will cause a change in the side-effects and in the approximation in the nonlinear FM pulse method. For example, a change in  $f_{\eta r}$  toward the Doppler centroid will decrease the side-effects of chirp scaling but increase the maximum phase error due to the approximation. A change in  $f_{\eta r}$  away from the Doppler centroid will do the reverse. To investigate this, Tables 7.19 and 7.20 show the worst case changes in range bandwidth, range-frequency shift and maximum phase error that result from a  $\pm 1^\circ$  error in measuring the squint angle. The same parameters as in Tables 7.17 and 7.18 were used in the calculations. The results do not differ significantly from those given in the previous subsection for the case of no squint estimate error. Thus, the nonlinear FM pulse method is robust to moderate errors in squint angle measurement for calculation of the transmitted pulse.

### 7.3.3 Effect of Pulse Doppler Shift

The use of a nonlinear FM transmitted pulse raises the question of the effect of a Doppler shift of a pulse on the matched filter output. A linear FM pulse is Doppler tolerant in that the effect of a Doppler mismatch in the matched filter is a shift in the compressed pulse. For a nonlinear FM pulse, the Doppler shift has the potential to cause a mismatch in the range

	C-band		
squint (degrees)	% bandwidth change	frequency shift (% of bandwidth)	maximum phase error (degrees)
10	0.2	0.9	7.7
20	0.7	2.5	22.1
30	1.4	5.1	44.6
40	3.0	8.9	85.2
50	7.2	14.3	179.4

Table 7.20: Side-effects and maximum phase error with  $f_{\eta r}$  changed to accommodate a  $\pm 1$  degree squint estimate error.

matched filter [11]. To minimize the Doppler shift in the signals before processing, the received signals are frequency shifted to remove the Doppler shift corresponding to the shift at the estimated Doppler centroid. Even for an error in Doppler centroid estimate corresponding to a one degree squint estimate error, the remaining Doppler shifts in the signals are much smaller than the Doppler resolution of an individual pulse. Thus, as described in the section on the stop-start assumption in Chapter 4, frequency shifting the received signals is sufficient to ensure an accurate matching of a received pulse with the range matched filter.

To verify this, consider a transmitted pulse for the nonlinear FM pulse method, of the form in Equation (7.204). Then consider the compression of a single received pulse which, after frequency shifting of the received signal, has a remaining Doppler shift of  $\delta f_d$ . The spectrum of the received pulse is given by

$$P(f_\tau - \delta f_d) = M(f_\tau - \delta f_d) \exp\left[j\pi \frac{(f_\tau - \delta f_d)^2}{K} + j \frac{2\pi}{3} Y_c (f_\tau - \delta f_d)^3\right]. \quad (7.218)$$

Thus, with a compression filter matched to the transmitted pulse, the remaining Doppler shift results in the following error terms in the phase of the compressed pulse spectrum:

$$\phi_{err} = -2\pi Y_c \delta f_d f_\tau^2 - 2\pi \left(\frac{\delta f_d}{K} - Y_c \delta f_d^2\right) f_\tau + 2\pi \left(\frac{\delta f_d^2}{2K} - \frac{Y_c \delta f_d^3}{3}\right). \quad (7.219)$$

To evaluate this error, assume  $Y_c$  is equal to its maximum value determined by the constraint in Equation (7.210) for the nonlinear FM pulse method. Also, assume a one degree error in the

squint estimate for frequency shifting the received signal. Then, for the worst case squint angle and wavelength, the maximum quadratic phase error due to the remaining Doppler shift is less than four degrees, which is negligible. Similarly, the change in pulse position and phase error is very small. Thus, the use of a nonlinear FM pulse does not significantly impair the matched filtering of the received signal.

#### 7.4 Simulations

In order to verify the analytical results describing nonlinear FM chirp scaling, point scatterer data was simulated and processed with the two different approaches. The point scatterer response was generated using the signal model for high squint, spaceborne SAR described in Chapter 4. In this model, a circular orbit was assumed in calculating the  $B$  parameter and the rate of change of  $B$  with range. Data was generated for L-band and C-band SAR, to simulate the signal from Seasat and ERS-1 platforms, respectively, and the scatterer was placed at the edge of the swath with  $(r - r_{ref}) = 20 \text{ km}$ . For the data that was to be processed with the nonlinear FM filtering method, the point scatterer response was simulated using a linear FM pulse. For the nonlinear FM pulse method, the data was generated with a nonlinear FM component in the pulse, and a one degree error in the squint estimate was assumed in calculating the nonlinear FM component. In all cases, rectangular amplitude weighting of the signal was used, and the width of the window in the range matched filter was 13 percent larger than the nominal range bandwidth. The results of processing the point scatterer data were then analyzed to determine the effect of processing errors and chirp scaling side-effects on the point spread function.

First, the accuracy of processing can be illustrated by the shape of the point spread function. Thus, to show the improvement in high squint SAR processing with nonlinear FM chirp scaling, Figure 7.34 shows contour plots of three point spread functions which result from processing simulated point scatterer data. The data was simulated at L-band and 25 degree squint, with the point scatterer placed 20 km from the reference range. Each of the contour plots corresponds to a different approach in processing the data: the original chirp scaling algorithm, the nonlinear

FM filtering method, and the nonlinear FM pulse method. As can be seen, the original chirp scaling algorithm results in severe distortion of the point spread function at high squint for scatterers away from the reference range, due to the range dependence of SRC. In contrast, the point spread function for the nonlinear FM filtering method is accurately focussed, and has the expected shape of a rotated *sinc* function. The nonlinear FM pulse method shows a slight distortion due to the approximation in the method, but is still adequately focussed.

Next, measurements of resolution, sidelobe level, registration, and phase were made on the point spread functions that resulted from processing simulated high squint data with the nonlinear FM filtering and nonlinear FM pulse methods. The following results are given for the range direction, since the point spread function in the azimuth direction is not significantly affected by the approximations in chirp scaling. Figure 7.35 presents plots of 3 dB range resolution width, in cells, versus squint angle, where a range cell is the 3dB width of a *sinc* function. Results are shown for L-band and C-band, for the filtering and pulse methods of nonlinear FM chirp scaling. Also, for comparison, the corresponding results for the original chirp scaling algorithm are repeated from Figure 5.29. As can be seen, the use of nonlinear FM chirp scaling dramatically improves the range resolution as a function of squint angle. The resolution for the filtering method is practically independent of squint angle, for squints up to the limitations described in Chapter 4. The approximation in the pulse method causes a slight degradation in resolution for squint angles above 30 degrees for L-band, and above 40 degrees for C-band.

Another effect of compression error is an increase in sidelobe level, and Table 7.21 shows the maximum sidelobe level for the two nonlinear FM chirp scaling approaches, for different squint angles at L-band and C-band. With accurate focussing, the rectangular weighting used in the matched filter results in the  $-13.2$  dB sidelobe level of a *sinc* function. Compared to the results for the original chirp scaling algorithm in Table 5.11, both methods of nonlinear FM chirp scaling preserve a relatively low sidelobe level for high values of squint.

The focussing of a point scatterer response in the range direction is mainly affected by

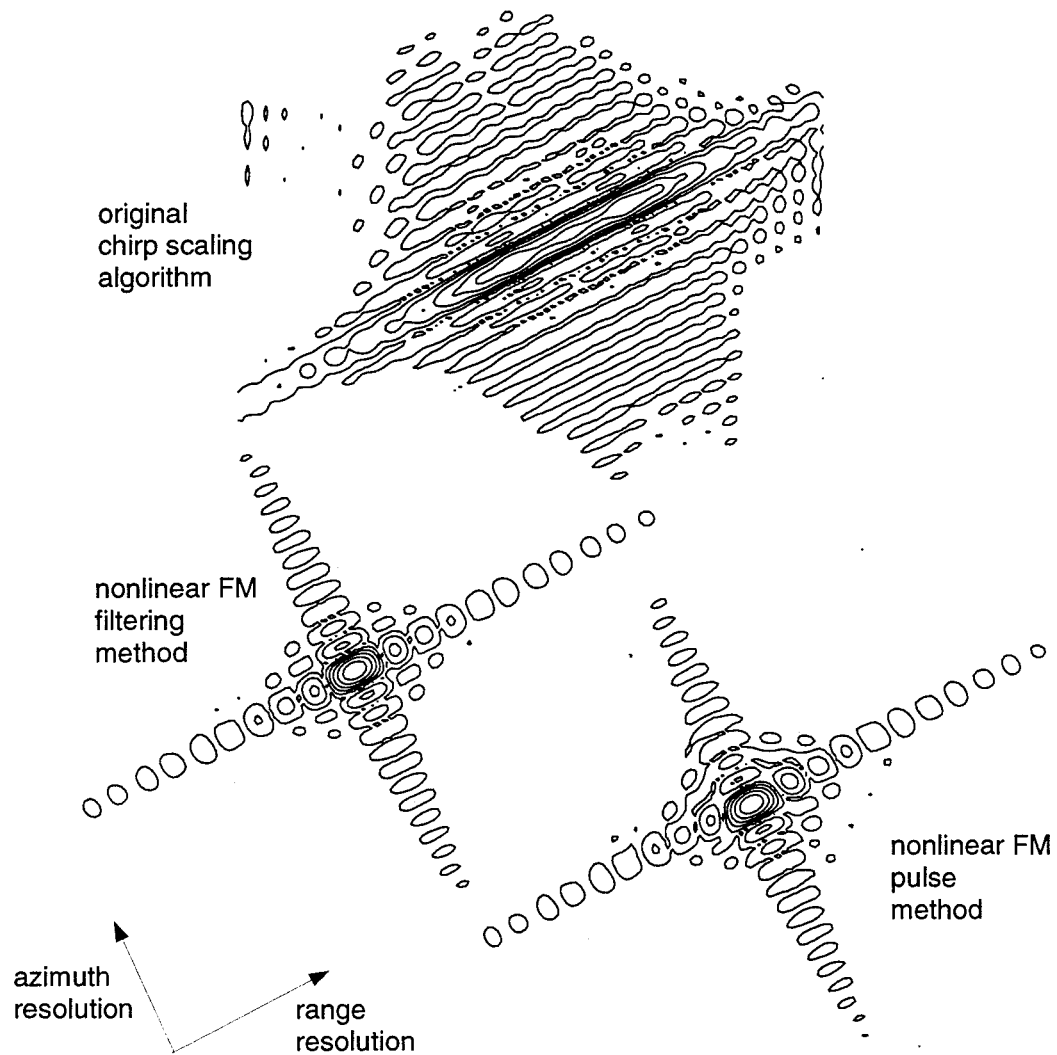


Figure 7.34: Contour plots of point spread functions for L-band at  $25^\circ$  squint,  $(r - r_{ref}) = 20\text{km}$ , using original chirp scaling algorithm, nonlinear FM filtering method, and nonlinear FM pulse method.

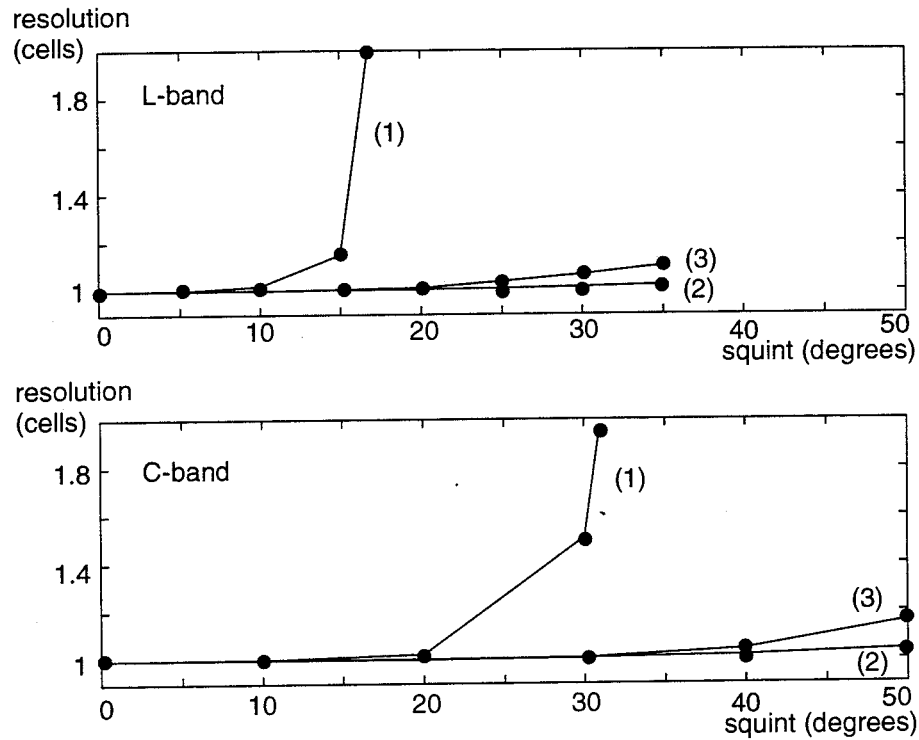


Figure 7.35: Simulation results of measured range resolution in cells vs. squint angle in degrees: (1) original chirp scaling algorithm; (2) nonlinear FM filtering method; and (3) nonlinear FM pulse method.

		Maximum Sidelobe Level in Range (dB)			
		L-band		C-band	
squint		filtering method	pulse method	filtering method	pulse method
10		-13.2	-13.1	-13.2	-13.2
20		-13.2	-12.5	-13.2	-13.0
30		-12.8	-11.7	-13.2	-12.9
40				-13.2	-12.1
50				-13.1	-11.3

Table 7.21: Simulation results of measured maximum sidelobe level of point spread function in range direction: nonlinear FM filtering method and nonlinear FM pulse method.

Range Registration Error (cells)				
L-band			C-band	
squint	filtering method	pulse method	filtering method	pulse method
10	0.00	0.00	0.00	0.00
20	0.01	0.02	0.00	0.00
30	0.03	0.05	0.00	0.01
40			0.00	0.02
50			0.04	0.07

Table 7.22: Simulation results of measured range registration error of point spread function: nonlinear FM filtering method and nonlinear FM pulse method.

the accuracy of SRC. Errors in RCMC may contribute to broadening slightly, but are more noticeable in their effect on the range registration of the compressed pulse. A registration error is a shift in the location of the compressed pulse from its expected position,  $\tau_d(f_{nr}; r)$ . Since an RCMC error is range dependent, a registration error increases toward the edge of the swath resulting in a geometric distortion of the image. In order to verify the accuracy of RCMC in the extensions to chirp scaling for orbital geometries, the range registration error of the compressed pulse was measured as a function of squint angle for the two methods of nonlinear FM chirp scaling. The results are presented in Table 7.22, for a scatterer at the edge of the swath. Although the error is slightly larger for the nonlinear FM pulse method, both methods of nonlinear FM chirp scaling give a very small registration error for squint angles up to 30 degrees for L-band, and up to 50 degrees for C-band.

Besides broadening, sidelobes, and registration, another performance criterion is the phase of the compressed pulse, which is used in SAR applications such as interferometry. Because of phase errors due to additive noise, and the fact that phase is very sensitive to inaccuracies in processing, a phase error of less than about 5 degrees indicates very good performance. Table 7.23 shows the phase error in the compressed pulse at the expected peak sample for the two nonlinear FM chirp scaling methods. In all cases, the phase error is very small, although again the error in the nonlinear FM pulse method is slightly larger.

	Peak Phase Error (degrees)			
	L-band		C-band	
	squint	filtering method	pulse method	filtering method
10	0.0	0.0	0.0	0.0
20	0.2	0.9	0.0	0.0
30	1.1	2.5	0.0	0.5
40			0.3	1.7
50			1.7	5.2

Table 7.23: Simulation results of measured phase error at expected peak sample of point spread function: nonlinear FM filtering method and nonlinear FM pulse method.

Finally, to show the worst case range impulse responses for the nonlinear FM chirp scaling methods, Figures 7.36 and 7.37 show plots of the amplitude of a slice of the point spread function in the range direction, for L-band at 35 degree squint and for C-band at 50 degree squint, respectively. As indicated by the previous results, in each case the range impulse response for the filtering method is essentially the same as the theoretical *sinc* function. Also, the range impulse response for the pulse method is slightly distorted by the approximation in this method.

Overall, the processing of simulated high squint data from a point scatterer has shown the accurate focussing that can be achieved with nonlinear FM chirp scaling. In addition, the slight distortion that results from the nonlinear FM pulse method demonstrates that this approach can be used to achieve accurate processing at high squint, without increasing the amount of computation.

## 7.5 Experiments With Skewed Seasat Data

### 7.5.1 Approach

The above results have shown the effectiveness of nonlinear FM chirp scaling on simulated point scatterer data. Next, the performance of the algorithm on real data is investigated.

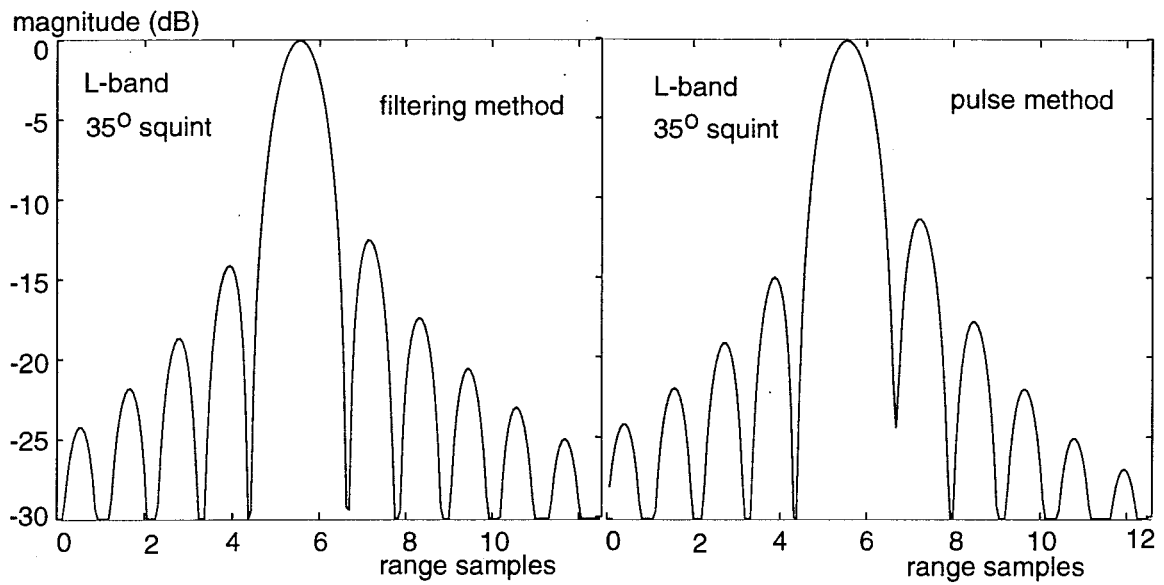


Figure 7.36: Magnitude of range slice of point spread function for L-band at  $35^\circ$  squint,  $(r - r_{ref}) = 20km$ , using nonlinear FM chirp scaling: filtering method and pulse method.

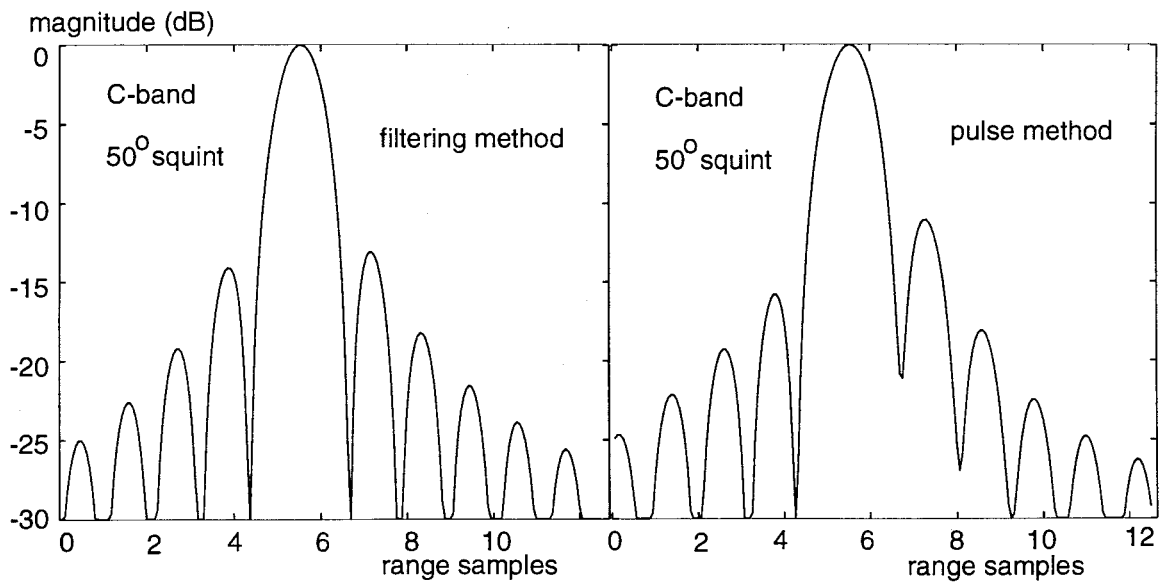


Figure 7.37: Magnitude of range slice of point spread function for C-band at  $50^\circ$  squint,  $(r - r_{ref}) = 20km$ , using nonlinear FM chirp scaling: filtering method and pulse method.

Since suitable data from a squint mode, strip-mapping SAR was not available, the approach was taken of skewing conventional SAR data in order to emulate squinted SAR data. This is done by shifting the received echos in raw SAR data in such a way that the point scatterer response in the data resembles that obtained with a high squint angle. This approach involves approximations in the signal model, so that in general the reverse operation cannot be used to remove the effect of squint from squint mode SAR data. However, for a short strip of data in the azimuth direction, the approach is adequate for the purpose of demonstrating the ability of nonlinear FM chirp scaling to process squinted SAR data.

The approach is illustrated in Figure 7.38, which shows the point scatterer responses from two scatterers separated in azimuth, before and after skewing the data. The data are skewed by shifting the received echos in range, by an amount that depends on the azimuth-time difference from some fixed azimuth-time,  $\eta_{ref}$ . This changes the apparent trajectory of the point scatterer response to correspond to that of a high squint angle. In addition, the data are multiplied by an azimuth varying phase factor, in order to make the azimuth phase term of the point scatterer response consistent with the high squint implied by the shifted data. After skewing, both point scatterer responses in Figure 7.38 have shapes that correspond to high squint data. However, the response that is located farther from  $\eta_{ref}$  is also shifted in its range position. Thus, the closest approach range that is used to process this response will not accurately match the range with which this signal was generated. The most significant effect of this range mismatch is an azimuth compression error, which will cause an azimuth broadening for scatterers located away from  $\eta_{ref}$ . For this reason, only a narrow strip in the azimuth direction is used.

### 7.5.2 Signal Model

Each range line of the SAR data is shifted by multiplying its Fourier transform by a linear phase factor that depends on the azimuth time of that range line. Thus, including the azimuth varying phase factor, this means the skewing of the data is accomplished in the range-frequency

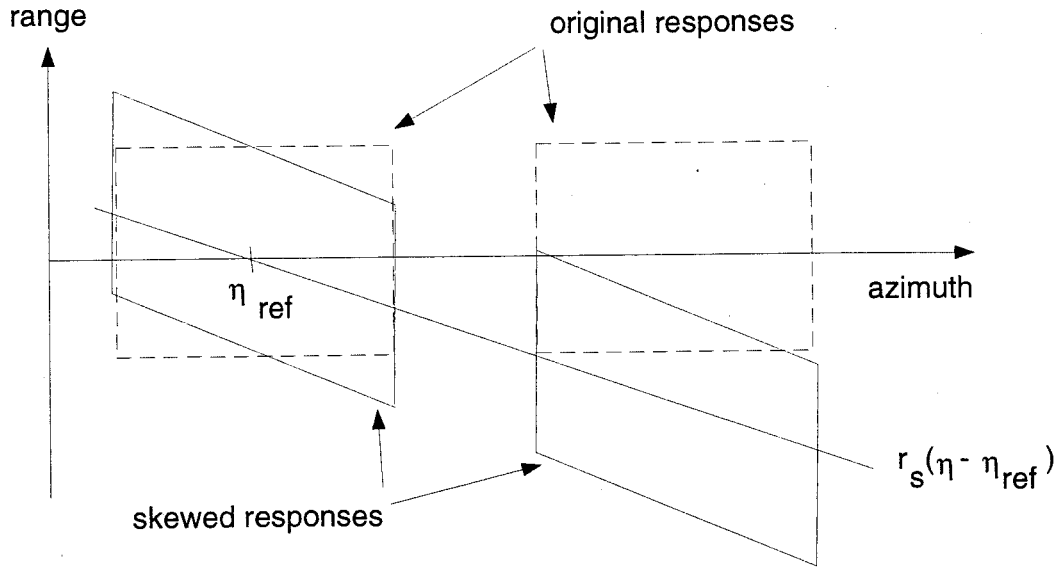


Figure 7.38: Illustration of skewed SAR data.

domain by multiplying the Fourier transform of each range line by:

$$\exp\left[\frac{-j4\pi(f_0 + f_\tau)}{c}r_s(\eta - \eta_{ref})\right], \quad (7.220)$$

where  $r_s$  is the slope of the skew. Consider the signal received from a scatterer at  $\eta_0$ , with an original distance equation of  $R(\eta - \eta_0; r_0)$ . After skewing the data, the signal will have the form:

$$s(\eta, \tau) = w(\eta - \eta_0 - \eta_c)p\left[\tau - \frac{2R_s(\eta - \eta_0; r_0)}{c}\right]\exp\left[\frac{-j4\pi f_0 R_s(\eta - \eta_0; r_0)}{c}\right], \quad (7.221)$$

where the distance equation of the skewed data is:

$$R_s(\eta - \eta_0; r_0) = R(\eta - \eta_0; r_0) + r_s(\eta - \eta_{ref}). \quad (7.222)$$

First, by taking the derivative of the azimuth phase term, the Doppler centroid of the skewed data can be shown to be

$$f_{\eta cs} = f_{\eta c} + \frac{2r_s}{\lambda}, \quad (7.223)$$

where  $f_{\eta c}$  is the Doppler centroid of the original data. Next, to obtain a model of the point scatterer response that can be used for processing, a hyperbolic equation can be fit to the

distance equation of the skewed data using the method described in Chapter 4. That is, a hyperbolic model of the distance equation is found such that

$$R_s(\eta - \eta_0; r_0) \approx R_h(\eta - \eta_0 - \eta_h; r_h), \quad (7.224)$$

where

$$R_h(\eta - \eta_0 - \eta_h) = \sqrt{r_h^2 + B_h(\eta - \eta_0 - \eta_h)^2}. \quad (7.225)$$

The parameters  $r_h$ ,  $B_h$ , and  $\eta_h$ , of the hyperbolic are found by equating  $R_h^2$  and its first and second derivatives, evaluated at  $\eta = (\eta_0 + \eta_c)$ , to the corresponding values for  $R_s^2$ . Note that since  $R_s$  depends on  $\eta_{ref}$ , the resulting model for the point scatterer response will depend on the azimuth position of the scatterer with respect to  $\eta_{ref}$ . Thus, an approximation is made in which the model is evaluated for the signal whose energy is centered on  $\eta_{ref}$ . This corresponds to ignoring the shift in the range position of the point scatterer response described above. Then, setting  $\eta_{ref} = (\eta_0 + \eta_c)$  gives the following expressions for the parameters of the signal model of the skewed data, as a function of the slope of the skew,  $r_s$ , and the parameters of the original data,  $r_0$ ,  $B$ , and  $\eta_c$ :

$$\begin{aligned} B_h &= \left( \frac{B\eta_c}{\sqrt{r_0^2 + B\eta_c^2}} + r_s \right)^2 + \frac{Br_0^2}{r_0^2 + B\eta_c^2} \\ \eta_h &= \eta_c - \frac{B\eta_c + r_s\sqrt{r_0^2 + B\eta_c^2}}{B_h} \\ r_h &= \sqrt{r_0^2 + B\eta_c^2 - B_h(\eta_c - \eta_h)^2}. \end{aligned} \quad (7.226)$$

With the hyperbolic model of the distance equation, the point scatterer response of the skewed data becomes

$$s(\eta, \tau) = w(\eta - (\eta_0 + \eta_h) - (\eta_c - \eta_h)) p\left[\tau - \frac{2R_h(\eta - \eta_0 - \eta_h; r_h)}{c}\right] \exp\left[\frac{-j4\pi f_0 R_h(\eta - \eta_0 - \eta_h; r_h)}{c}\right], \quad (7.227)$$

where the azimuth and range position of the scatterer are assumed to be  $(\eta_0 + \eta_h)$  and  $r_h$ , respectively. Also, the beam center offset time has been changed to  $(\eta_c - \eta_h)$ , corresponding to a higher squint angle.

### 7.5.3 Results

The above approach was used to skew conventional, spaceborne SAR data from the Seasat satellite. The Seasat SAR was operated at L-band, and the data was obtained over the city of Vancouver, B.C. The original squint angle of the data was about 3 degrees, and the data was skewed to emulate a squint angle of 25 degrees.

The skewed data was processed with the original chirp scaling algorithm, and with the filtering method of the nonlinear FM chirp scaling algorithm. In each case, the signal model for processing the data was determined as shown above. The data was filtered to reduce the azimuth bandwidth to  $1100\text{ Hz}$ , compared to the  $PRF$  of  $1647\text{ Hz}$ . This was done to reduce the length of the azimuth matched filter thereby reducing the overhead for producing a narrow azimuth strip of an image, and to avoid aliasing in the image spectrum as described in Chapter 4. To register the image correctly in azimuth, a linear phase term was added to the azimuth compression filter to remove the offset  $\eta_h$ . Finally, the skew was removed from the image after processing, to retain the original shape of features in the image.

Figures 7.39 and 7.40 show the results of processing with the original chirp scaling algorithm and the nonlinear FM chirp scaling algorithm, respectively. The single-look complex images that were produced were detected and averaged in the azimuth direction by a factor of four, in order to achieve the effect of multilooking that is commonly used to reduce speckle. Small portions of the processed images were extracted to show the detail, and the images shown in the figures are 256 samples in azimuth by 575 samples in range. The width of the images in the azimuth direction is about  $4.5\text{ km}$ , and the difference in slant range across the image is about  $3.9\text{ km}$ . Also, in each case the reference range was set to be  $20\text{ km}$  from the center of the image. For the original chirp scaling algorithm, this distance from the reference range results in a noticeable degradation in the image due to the range dependence of secondary range compression. The blur in the image is particularly noticeable at points and at edges that run perpendicular to the range direction. In contrast, the image formed with nonlinear FM chirp scaling is much better focussed. For comparison, Figure 7.41 shows an image formed with the

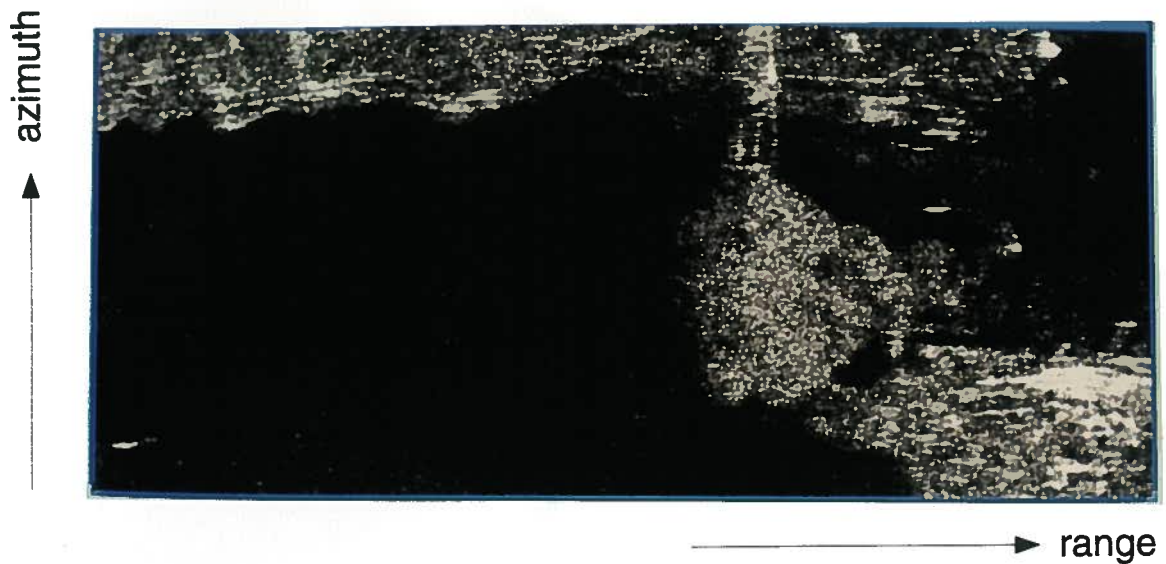


Figure 7.39: Image of Vancouver scene formed from skewed data with the original chirp scaling algorithm, with the reference range  $20\text{ km}$  from the center of the image.

original chirp scaling algorithm, but with the reference range in the center of the image. Since the image formed with the nonlinear FM chirp scaling algorithm is comparable to the image with the reference range at the center, this shows that nonlinear FM chirp scaling successfully accommodates the range dependence of SRC.

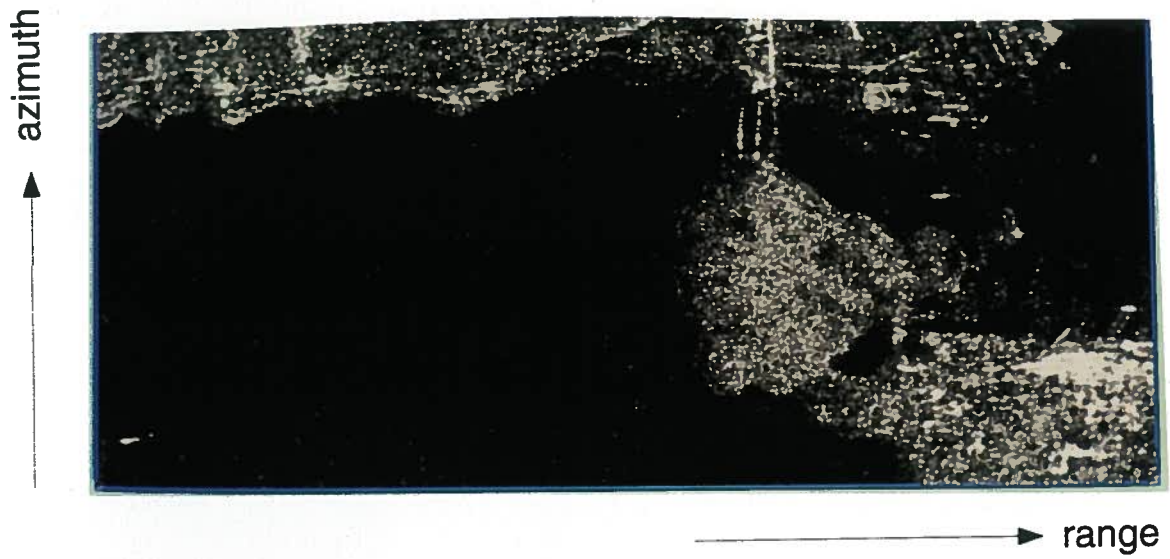


Figure 7.40: Image of Vancouver scene formed from skewed data with the nonlinear FM chirp scaling algorithm, with the reference range 20 km from the center of the image.



Figure 7.41: Image of Vancouver scene formed from skewed data with the original chirp scaling algorithm, with the reference range at the center of the image.

## Chapter 8

### Conclusion

#### 8.1 Summary

The objective of this thesis has been the investigation of the processing of squint mode strip-map SAR data, particularly by extending the chirp scaling algorithm. The following is a summary of the work contained in the thesis.

The theory of strip-map SAR imaging has been reviewed, in which SAR processing has been presented in terms of matching the range dependent phase of the SAR transfer function. Then, SAR processing algorithms were reviewed and compared according to how accurately they match the phase of the SAR transfer function, and the type of processing operations they require. Range-Doppler domain algorithms accommodate the range-dependence of some processing steps in the range-Doppler domain, and generally use an interpolator to perform RCMC. In the range-Doppler algorithm, approximations are made in SRC by assuming that the SRC filter is invariant in both azimuth-frequency and range. The squint imaging mode algorithm is more accurate by allowing SRC to vary with azimuth-frequency, while still assuming it to be invariant in range. The polar format and wave equation algorithms match the range dependent phase by an interpolation in the two-dimensional frequency domain, in order to take advantage of the definition of the Fourier transform. The relationship between the polar format and wave equation algorithms has been shown. In the polar algorithm, scatterers are assumed to be close enough together that the relationship between azimuth-time and azimuth-frequency is given by that at a reference point. However, this assumption makes the polar algorithm unsuitable for strip-map SAR data. The Stolt algorithm is more general in the sense that the azimuth-frequency domain is obtained by a Fourier transform of the data in the azimuth

direction. Then, a range-frequency domain interpolation provides focussing. However, since frequency domain interpolation is computationally expensive, approximations have been made to the Stolt method to avoid interpolation. The resulting algorithm also avoids interpolation in the range-Doppler domain during RCMC, but the approximation means that RCMC and SRC are calculated at a fixed range, and the error in RCMC becomes noticeable for moderate squint angles. The chirp scaling algorithm has been developed recently as a means of providing accurate RCMC without an interpolator, and this has been described in detail. The chirp scaling algorithm also allows SRC to vary with azimuth-frequency, although it is still calculated at a fixed range.

Next, the effect of squint mode on SAR signal properties was considered. In particular, the effect on the Doppler centroid and the azimuth bandwidth of the yaw and pitch angles used to achieve the desired squint angle were described. The squint angle was derived as a function of yaw, pitch, and elevation. Also, to minimize Doppler centroid variation with range and terrain height, a solution was presented for the yaw and pitch angles which minimizes the variation of squint with elevation angle within the beam. The Doppler centroid error that results at the edge of the swath or at a terrain height change of 1000 *km* was calculated as a function of desired squint angle, including the effects of antenna pointing errors. It was found that for a satellite platform the effect of terrain height variation was negligible. In addition, for L-band, even with pointing errors up to one degree, the maximum Doppler centroid error at the edge of the swath was less than 10 percent of the *PRF*. For C-band, the Doppler centroid variation in range was acceptable for the far incidence case, but was as high as a third of the *PRF* in the near incidence case. The yaw and pitch angles also affect the squinted beamwidth, or the change in instantaneous squint angle seen by a scatterer as it passes through the footprint. A general expression for the squinted beamwidth was derived. Also, it was shown that minimizing the variation of squint with elevation angle preserves, in squint mode, the SAR signal property of an azimuth bandwidth that is independent of range. This gives an azimuth bandwidth that decreases with squint, which turns out to be an important property with respect to satisfying

the SAR imaging constraint. For a given range swath, wavelength, and antenna length, the SAR signal constraint places a fundamental limit on the squint angle. For typical spaceborne SAR parameters at L-band, this is about 35 degrees, and for C-band it is about 50 degrees.

Other effects of high squint on the SAR signal were investigated. The effect of the stop-start assumption on the distance equation was examined, and the main effect of platform motion during the pulse was shown to be a Doppler shift of a received pulse. At high squint this can become significant compared to the Doppler resolution of an individual pulse. However, by frequency shifting the received signal to remove the shift corresponding to the beam center, the only effect is the variation of the pulse Doppler shift across the aperture, which is negligible. Next, a method for modelling the distance equation at high squint was discussed in which a hyperbola was fit to the equation at the beam center time. This gives a good approximation to the distance equation over the aperture for squint angles up to 40 degrees for L-band and 50 degrees for C-band. However, it requires the definition of a new closest approach range variable that needs to be taken into account when resampling to ground coordinates. Finally, the difference between the data spectrum and the image spectrum at high squint was discussed. The region of support of the data spectrum has the form of a parallelogram, where the width of the spectrum is equal to the azimuth bandwidth. However, the total spectrum spans an interval of azimuth-frequencies that may be greater than the  $PRF$ , so that during processing some range-frequency lines at the edges of the spectrum may need to be repeated to avoid aliasing in azimuth. The image spectrum, which results after range-variant processing, was shown to be a rotation of the zero-squint spectrum along an arc in the two dimensional frequency domain. The corresponding point spread function for high squint is a rotated *sinc* function, so that range and azimuth resolutions are measured in different directions in the image than they are for zero squint.

The chirp scaling algorithm was implemented on Seasat data, and the image quality was compared with that of a commercial range-Doppler processor. Visual inspection of the images showed the effects of the truncation of the interpolator in the range-Doppler algorithm. Also,

point scatterer analysis of the images of corner reflectors showed that the range resolution of the chirp scaling algorithm was about four percent better than that of the range-Doppler algorithm. Next, the performance of the algorithms as a function of squint angle was compared for simulated point scatterer data. For a scatterer at the reference range, the range resolution of the chirp scaling algorithm was equal to the theoretical resolution independently of squint angle. For the range-Doppler algorithm, resolution began to degrade at about five degrees squint for L-band, and at thirty degrees for C-band.

The side-effects and approximations of the chirp scaling algorithm were then investigated. It was shown that an effect of the chirp scaling phase function multiply was a change in range bandwidth by the scale factor. Also, in the two-dimensional frequency domain, the signal experiences a range-frequency shift that varies with the range of the scatterer, which must be small enough to avoid a loss of range bandwidth when matched filtering in the frequency domain. Both these effects are small when the reference azimuth-frequency is at the Doppler centroid. Also, the range-frequency shift is later removed in the range-Doppler domain by the phase correction step. The approximations in chirp scaling were shown to consist of: 1) approximation to the desired trajectory by assuming a constant  $B$  parameter; 2) assumption of a range-invariant range frequency rate, affecting SRC and the calculation of the chirp scaling phase function; and 3) assumption of linear FM by ignoring the cubic phase term in the SAR transfer function. The effects of these approximations were calculated as a function of squint angle. The constant  $B$  assumption introduced noticeable RCMC errors for squint angles above about 15 degrees for L-band and 30 degrees for C-band. The effect of the linear FM assumption was fairly small, the most noticeable effect being the introduction of a quadratic phase error above 30 degrees squint for L-band, and was negligible for C-band. Of all the approximations, the SRC error due to assuming a range-invariant frequency rate was found to have the most significant affect on performance as the squint angle increased. For a scatterer at the edge of the swath, resolution degraded rapidly for squint angles above 10 degrees for L-band and above 20 degrees for C-band. These results were verified by processing simulated point scatterer data.

Finally, since the chirp scaling algorithm depends on a linear FM pulse, the effect of deviations from linear FM and a specified frequency rate in the transmitted pulse were investigated. A general form for the phase error in the SAR transfer function due to a pulse phase error was derived. In general, the effects were found to be small, indicating that chirp scaling is robust to errors in the transmitted pulse.

The chirp scaling algorithm was extended to provide accurate RCMC at higher squint angles. The range dependence of the  $B$  parameter was taken into account to derive a more accurate representation of the desired trajectory, and the range dependence of  $K_m$  was included in the signal model. Then, a higher order phase term was included in the chirp scaling phase function. Expressions for the chirp scaling coefficients were determined by equating terms of the scaled trajectory and the desired trajectory, thus removing higher order range dependence of RCMC. The resulting RCMC error in this case is negligible, although the higher order chirp scaling adds a small term to the range dependent quadratic phase error.

Finally, a new approach to accommodating the range dependence of SRC was introduced, providing an accurate and efficient algorithm for processing high squint data. This approach makes use of a nonlinear FM component in the range signal while chirp scaling. The equations for the nonlinear FM component and the coefficients of the chirp scaling phase function can be solved simultaneously so that both SRC and RCMC are performed accurately across the range swath. To allow the nonlinear FM component to vary with azimuth-frequency, an extra filtering step is required during processing to introduce the component in the two-dimensional frequency domain. This approach, called the nonlinear FM filtering method, is the most accurate. Also, the extra computation required is favourable compared to a range-variant, time domain SRC filter, especially since the nonlinear FM filter method of chirp scaling requires only FFT and multiply operations. Alternatively, the nonlinear FM component can be introduced directly into the transmitted pulse, so that no extra computation beyond that of the chirp scaling algorithm is required. This is called the nonlinear FM pulse method, and it makes the approximation of calculating the nonlinear FM component at the Doppler centroid. The nonlinear FM component

is calculated for the transmitted pulse using the estimate of the squint angle available at that time. Then, during processing, an error in the squint estimate can be accommodated by adjusting the reference azimuth-frequency. This changes the chirp scaling phase function to correspond to the nonlinear FM component that was actually used in the transmitted pulse, thus providing the correct compensation of range dependent SRC.

In chirp scaling, the amount of scaling increases with the azimuth-frequency difference from the reference azimuth-frequency. In order for there to be a nonzero chirp scaling effect at all azimuth-frequencies in the band, which can interact with the nonlinear FM component in the signal, nonlinear FM chirp scaling requires the reference azimuth-frequency to be placed outside of the signal band. In addition, the effect of the approximation in the nonlinear FM pulse method decreases as the reference azimuth-frequency is moved further from the signal band. However, the increased scaling with greater  $(f_\eta - f_{\eta r})$  means that the side-effects of chirp scaling increase. Thus, the algorithm is limited by the range dependent range-frequency shift that is introduced by the chirp scaling phase function, since this must be small enough to keep the range-frequencies in the signal less than the Nyquist rate. Otherwise some signal energy and range bandwidth are lost when multiplying the data by the range matched filter in the frequency domain.

Both methods of nonlinear FM chirp scaling were used to process simulated point scatterer data for a scatterer at the edge of the swath. The nonlinear FM filtering method is more accurate, and can process data with a negligible increase in resolution width or sidelobes for squint angles up to 35 degrees for L-band and 50 degrees for C-band. The nonlinear FM pulse method is less accurate, and requires a reference azimuth-frequency such that a greater range-frequency shift is introduced. Nevertheless, the effect on resolution width is negligible for squint angles up to about 30 degrees for L-band and 40 degrees for C-band, and is still acceptable for higher squint. Furthermore, both methods of nonlinear FM chirp scaling resulted in negligible errors in range registration and peak phase of the point spread function. Thus, nonlinear FM chirp scaling can provide accurate processing for squint angles up to the limitations imposed by

the SAR imaging constraints. In addition, the nonlinear FM pulse method provides adequate focussing at no extra cost in computation.

Finally, the nonlinear FM chirp scaling algorithm was verified on real data. Since no suitable squinted data was available, conventional SAR data from the Seasat satellite was skewed in order to emulate squinted data, and then processed with the original chirp scaling algorithm and the filtering method of nonlinear FM chirp scaling. In each case the reference range was set to be 20 km from the center of the image, and the resulting images show the improvement in range resolution with nonlinear FM chirp scaling.

Overall, this thesis has shown how strip-map, squint mode SAR data can be collected such that SAR imaging constraints can be satisfied, and signal properties that are useful for processing are preserved. In addition, nonlinear FM chirp scaling provides a means of accurately and efficiently processing squint mode SAR data.

## 8.2 Contributions

The following is a list of the major contributions of the thesis:

- Understanding of the relationship between the polar algorithm and the Stolt interpolation algorithm as applied to SAR processing.
- Derivation of yaw and pitch angles to minimize Doppler centroid variation as a function of elevation angle, thus minimizing Doppler centroid variation with range and terrain height.
- Derivation of the squinted beamwidth and azimuth bandwidth as a function of yaw and pitch. Understanding of the importance of choosing yaw and pitch that minimize Doppler centroid variation, in order to maintain an azimuth bandwidth that is independent of elevation and that decreases with squint to satisfy SAR imaging constraints.
- Derivation of side-effects, and errors due to approximations in chirp scaling.
- Derivation of the effect of general pulse phase errors on the SAR transfer function due to chirp scaling.

- Extension of the chirp scaling algorithm for accurate RCMC, which allows for a range variant  $B$  in an orbital geometry and a range variant range frequency rate.
- Introduction of the concept of nonlinear FM chirp scaling to accommodate the range dependence of SRC. Development of the nonlinear FM filtering method of chirp scaling and the derivation of squint limitations due to the range-frequency shift.
- Introduction of the nonlinear FM pulse method for squint mode SAR data collection and processing, including the accommodation during processing of an error in the squint estimate.

### 8.3 Further Work

SAR processing requires knowledge of processing parameters describing the distance equation and the Doppler centroid. It is possible that a high squint imaging geometry or the use of the chirp scaling algorithm may affect the estimation of these parameters, and this should be investigated. In addition, the considerations for squint mode data collection and processing that have been presented in this thesis should be verified on actual high squint data.

The thesis has been concerned with spaceborne platforms. However, the considerations and processing for high squint data apply equally well to airborne platforms, and comparable results could be obtained for airborne SAR. A consideration in this case is motion compensation, and its effect on high squint, strip-map SAR processing could be investigated.

It may be possible to apply the concept of chirp scaling and nonlinear FM chirp scaling to other fields. For example, it may be possible to apply chirp scaling concepts to the interpolation required in spotlight SAR, thus improving the efficiency. Other imaging applications that may benefit include seismic processing and tomography.

Finally, the applications of squint mode SAR imagery should be investigated. With real high squint data, the effect of different azimuth viewing angles on the measurement of various surface properties could be studied.

## Bibliography

- [1] C. Elachi. *Spaceborne Radar Remote Sensing: Applications and Techniques*. I.E.E.E. Press, 1988.
- [2] J. C. Curlander and R. N. McDonough. *Synthetic Aperture Radar: Systems and Signal Processing*. John Wiley and Sons, Inc., New York, 1991.
- [3] J. Way and E. A. Smith. The evolution of synthetic aperture radar systems and their progression to the EOS SAR. *I.E.E.E. Trans. on Geoscience and Remote Sensing*, 29(6):962–985, 1991.
- [4] E. P. W. Attema. The active microwave instrument on-board the ERS-1 satellite. *Proceedings of the I.E.E.E.*, 79(6):791–799, 1991.
- [5] Y. Nemoto, H. Nishino, M. Ono, H. Mizutamari, K. Nishikawa, and K. Tanaka. Japanese earth resources satellite-1 synthetic aperture radar. *Proceedings of the I.E.E.E.*, 79(6):800–809, 1991.
- [6] R. K. Raney, A. P. Luscombe, E. J. Langham, and S. Ahmed. RADARSAT. *Proceedings of the I.E.E.E.*, 79(6):839–849, 1991.
- [7] R. L. Jordan, B. L. Huneycutt, and M. Werner. The SIR-C/X-SAR synthetic aperture radar system. *Proceedings of the I.E.E.E.*, 79(6):827–838, 1991.
- [8] F. T. Ulaby, D. Held, M. C. Dobson, K. C. McDonald, and T. B. A. Senior. Relating polarization phase difference of SAR signals to scene properties. *I.E.E.E. Trans. on Geoscience and Remote Sensing*, GE-25(1):83–91, 1987.
- [9] C. Prati, F. Rocca, A. M. Guarnieri, and E. Damonti. Seismic migration for SAR focussing: interferometrical applications. *I.E.E.E. Transactions on Geoscience and Remote Sensing*, 28(4):627–640, 1990.
- [10] C. E. Cook and M. Bernfeld. *Radar Signals*. Academic Press, New York, 1967.
- [11] A. W. Rihaczek. *Principles of High-Resolution Radar*. McGraw-Hill, New York, 1969.
- [12] R. O. Harger. *Synthetic aperture radar systems: theory and design*. Academic Press, New York, 1970.
- [13] K. Tomiyasu. Tutorial review of synthetic-aperture radar (SAR) with applications to imaging of the ocean surface. *Proceedings of the I.E.E.E.*, 66(5):563–583, 1978.
- [14] I. G. Cumming and J. R. Bennett. Digital processing of SEASAT SAR data. In *ICASSP'79 Proceedings*, pages 710–718, 1979.

- [15] C. Wu, K. Y. Liu, and M. Jin. Modeling and a correlation algorithm for spaceborne SAR signals. *I.E.E.E. Transactions on Aerospace and Electronic Systems*, AES-18:563–575, 1982.
- [16] B. C. Barber. Theory of digital imaging from orbital synthetic-aperture radar. *International Journal of Remote Sensing*, 6(7):1009–1057, 1985.
- [17] R. K. Raney. An exact wide field digital imaging algorithm. *International Journal of Remote Sensing*, 13(5):991–998, 1992.
- [18] I. G. Cumming, F. H. Wong, and R. K. Raney. A SAR processing algorithm with no interpolation. In *IGARSS'92 Proceedings*, pages 376–379, 1992.
- [19] H. Runge and R. Bamler. A novel high precision SAR focussing algorithm based on chirp scaling. In *IGARSS'92 Proceedings*, pages 372–375, 1992.
- [20] J. L. Walker. Range-Doppler imaging of rotating objects. *I.E.E.E. Transactions on Aerospace and Electronic Systems*, AES-16(1):23–52, 1980.
- [21] D. L. Mensa, S. Halevy, and G. Wade. Coherent Doppler tomography for microwave imaging. *Proceedings of the I.E.E.E.*, 71(2):254–261, 1983.
- [22] D. C. Munson Jr., J. D. OBrian, and W. K. Jenkins. A tomographic formulation of spot-light mode synthetic aperture radar. *Proceedings of the I.E.E.E.*, 71:917–925, 1983.
- [23] D. A. Ausherman, A. Kozma, J. L. Walker, H. M. Jones, and E. C. Poggio. Developments in radar imaging. *I.E.E.E. Transactions on Aerospace and Electronic Systems*, AES-20(4):363–398, 1984.
- [24] C. Y. Chang, M. Jin, and J. C. Curlander. Squint mode SAR processing algorithms. In *IGARSS'89 Proceedings*, pages 1702–1706, 1989.
- [25] R. K. Raney. Doppler properties of radars in circular orbits. *International Journal of Remote Sensing*, 7(9):1153–1162, 1986.
- [26] F. Li, D. N. Held, J. C. Curlander, and C. Wu. Doppler parameter estimation for spaceborne synthetic-aperture radars. *I.E.E.E. Trans. on Geoscience and Remote Sensing*, GE-23(1):47–55, 1985.
- [27] R. Bamler. Doppler frequency estimation and the cramer-rao bound. *I.E.E.E. Trans. on Geoscience and Remote Sensing*, 29(3):385–390, 1991.
- [28] I. G. Cumming, P. Kavanagh, and M. R. Ito. Resolving the Doppler ambiguity for spaceborne synthetic aperture radar. In *IGARSS'86 Proceedings*, pages 1639–1643, 1986.
- [29] C. Y. Chang and J. C. Curlander. Doppler centroid estimation ambiguity for synthetic aperture radars. In *IGARSS'89 Proceedings*, pages 2567–2571, 1989.

- [30] R. Bamler and H. Runge. Prf-ambiguity resolving by wavelength diversity. *I.E.E.E. Trans. on Geoscience and Remote Sensing*, 29(6):997–1003, 1991.
- [31] R. K. Raney. Considerations for SAR image quantification unique to orbital systems. *I.E.E.E. Trans. on Geoscience and Remote Sensing*, 29(5):754–760, 1991.
- [32] C. Cafforio, C. Prati, and F. Rocca. SAR focusing using seismic migration techniques. *I.E.E.E. Trans. on Aerosp. and Elect. Syst.*, 27(2):194–207, 1991.
- [33] V. J. Mantle. Wave equation SAR algorithm project report: notes on the range equation. Technical report, MacDonald Dettwiler, 1990. Report number RX-TN-MDA-SY-0029.
- [34] D. Casey and J. Way. Orbit selection for the EOS mission and its synergism implications. *I.E.E.E. Transactions on Geoscience and Remote Sensing*, 29(6):822–835, 1991.
- [35] R. W. Bayma and P. A. McInnes. Aperture size and ambiguity constraints for a synthetic aperture radar. In *Record of the I.E.E.E. 1975 International Radar Conference*, pages 499–504, 1975.
- [36] A. Papoulis. *Signal Analysis*. McGraw-Hill Co., New York, 1977.
- [37] I. G. Cumming and F. H. Wong. A new algorithm for accurate processing for RADARSAT SAR processor. Technical report, MacDonald Dettwiler, 1991. Report number RT-RP-50-3264.
- [38] R. K. Raney. A new and fundamental Fourier transform pair. In *IGARSS'92 Proceedings*, pages 106–107, 1992.
- [39] R. Bamler. A comparison of range-Doppler and wavenumber domain SAR focusing algorithms. *I.E.E.E. Trans. on Geoscience and Remote Sensing*, 30(4):706–713, 1992.
- [40] L. J. Porcello, N. G. Massey, R. B. Innes, and J. M. Marks. Speckle reduction in sythentic-aperture radars. *Journal of the Optical Society of America*, 66(11):1305–1311, 1976.
- [41] A. M. Smith. A new approach to range-Doppler SAR processing. *International Journal of Remote Sensing*, 12(2):235–251, 1991.
- [42] C. J. Oliver. Synthetic-aperture radar imaging. *Journal of Physics D: Applied Physics*, 22:871–890, 1989.
- [43] M. Y. Jin and C. Wu. A SAR correlation algorithm which accommodates large range migration. *I.E.E.E. Trans. on Geoscience and Remote Sensing*, GE-22(6):592–597, 1984.
- [44] F. H. Wong and I. G. Cumming. Error sensitivities of a secondary range compression algorithm for processing squinted satellite SAR data. In *IGARSS'89 Proceedings*, pages 2584–2587, 1989.
- [45] C. Y. Chang, M. Y. Jin, and J. C. Curlander. SAR processing based on the exact two-dimensional transfer function. In *IGARSS'92 Proceedings*, pages 355–359, 1992.

- [46] A. R. Schmidt. Secondary range compression for improved range-Doppler processing of SAR data with high squint. Master's thesis, University of British Columbia, 1986.
- [47] R. H. Stolt. Migration by Fourier transform. *Geophysics*, 43(1):23–48, 1978.
- [48] J. W. Goodman. *Introduction to Fourier Optics*. McGraw-Hill, New York, 1968.
- [49] J. F. Claerbout. *Fundamentals of Geophysical Data Processing*. McGraw-Hill, New York, 1976.
- [50] J. Gazdag and P. Sguazzero. Migration of seismic data. *Proceedings of the I.E.E.E.*, 72(10):1302–1315, 1984.
- [51] R. K. Raney, I. G. Cumming, and F. H. Wong. Synthetic aperture radar processor to handle large squint with high phase and geometric accuracy. U. S. Patent 5179383, 1993.
- [52] M. Y. Jin, S. Hensley, and A. Chu. Spaceborne SAR processing for wide beam and large squint angle systems. In *SPIE Proceedings*, 1993.
- [53] H. Runge. Benefits of antenna yaw steering for SAR. In *IGARSS'91 Proceedings*, pages 257–261, 1991.
- [54] B. Aster and P. Di Stasio. Modelling earth rotation and spaceborne attitude errors for theoretic Doppler parameters evaluation. In *IGARSS'91 Proceedings*, pages 2409–2411, 1991.
- [55] C. Y. Chang and J. C. Curlander. Attitude steering for space shuttle based synthetic aperture radars. In *IGARSS'92 Proceedings*, pages 297–301, 1992.
- [56] W. H. Press, B. P. Flannery, S. A. Teukolsky, and W. T. Vetterling. *Numerical Recipes in C*. Cambridge University Press, Cambridge, 1988.
- [57] W. J. van de Lindt. Digital technique for generating synthetic aperture radar images. *IBM Journal of Research and Development*, pages 415–432, 1977.
- [58] J. C. Curlander. Location of spaceborne SAR imagery. *I.E.E.E. Transactions on Geoscience and Remote Sensing*, GE-20(3):359–364, 1986.
- [59] D. C. Munson and J. L. C. Sanz. Image reconstruction from frequency-offset Fourier data. *Proceedings of the I.E.E.E.*, 72(6):661–669, 1984.
- [60] Radarsat phase CI/C Radarsat space segment system preliminary design review. Technical report, SPAR, 1991. Report number RML-009-91-089.
- [61] F. H. Wong, I. G. Cumming, and R. K. Raney. Processing of simulated RADARSAT SAR data with squint by a high precision algorithm. In *IGARSS'93 Proceedings*, pages 1176–1178, 1993.

## Appendix A

### Approximation to Inverse Fourier Transform With Cubic Phase Term

In this appendix, the approximation to the method of stationary phase is described for evaluating the range inverse Fourier transform of a SAR transfer function with a cubic phase term. Thus, it is desired to approximate the solution to the integral:

$$S_Y(f_\tau, \tau; r) = F_{ac}(f_\tau; r) \int M(f_\tau) \exp[j2\pi((\tau - \tau_d)f_\tau + \frac{f_\tau^2}{2K_m} + \frac{Y_m}{3} f_\tau^3)] df_\tau, \quad (\text{A.228})$$

where  $M(f_\tau)$  is the amplitude,  $\tau_d$  is the signal delay,  $K_m$  is the frequency rate, and  $Y_m$  is the cubic phase coefficient. The equation for the stationary point is

$$(\tau - \tau_d) + \frac{f_\tau}{K_m} + Y_m f_\tau^2 = 0, \quad (\text{A.229})$$

which has the solution

$$f_{\tau^*} = \frac{-1}{2Y_m K_m} \pm \frac{1}{2Y_m K_m} \sqrt{1 - 4K_m^2 Y_m (\tau - \tau_d)}. \quad (\text{A.230})$$

For small enough  $Y_m$ , assume that the condition

$$|Y_m K_m^2 (\tau - \tau_d)| \ll 1 \quad (\text{A.231})$$

is satisfied for all values of  $\tau$  within the pulse. Since the pulse length in the range-Doppler domain is  $T_m$ , this leads to the condition on  $Y_m$  that is given in Equation (7.184). Then, using the expansion

$$\sqrt{1-x} = 1 - \frac{x}{2} - \frac{x^2}{8} - \frac{x^3}{16} - \dots, \quad |x| < 1, \quad (\text{A.232})$$

the stationary point can be approximated by

$$f_{\tau^*} \approx -K_m(\tau - \tau_d) - Y_m K_m^3 (\tau - \tau_d)^2 - 2Y_m K_m^5 (\tau - \tau_d)^3. \quad (\text{A.233})$$

From the method of stationary phase, the range inverse transform is found by substituting for the stationary point in the integrand. Since amplitude generally varies more slowly than phase, fewer terms in the approximation to the stationary point are used in the amplitude than in the phase. An expression for the range inverse transform then becomes

$$S_Y(f_\eta, \tau; r) = F_{ac}(f_\eta; r) \sqrt{\frac{2\pi |K_m|}{|1 + 2Y_m K_m^2(\tau - \tau_d)|}} M[-K_m(\tau - \tau_d) - Y_m K_m^3(\tau - \tau_d)^2] \exp[-j\pi K_m(\tau - \tau_d)^2 - \frac{j2\pi}{3} Y_m K_m^3(\tau - \tau_d)^3 - j\pi Y_m^2 K_m^5(\tau - \tau_d)^4]. \quad (\text{A.234})$$

Finally, because of the condition on  $Y_m$ , the square root term in the result which arises from the method of stationary phase is not greatly affected by the cubic phase term. Thus this is nearly a constant and will be neglected. Also, using the definition of  $M(f_\tau)$  in terms of the pulse amplitude, the result can be expressed as

$$S_Y(f_\eta, \tau; r) = F_{ac}(f_\eta; r) m \left[ \frac{K_m}{K}(\tau - \tau_d) - \frac{Y_m K_m^3}{K}(\tau - \tau_d)^2 \right] \exp[-j\pi K_m(\tau - \tau_d)^2 - \frac{j2\pi}{3} Y_m K_m^3(\tau - \tau_d)^3 - j\pi Y_m^2 K_m^5(\tau - \tau_d)^4]. \quad (\text{A.235})$$

## Appendix B

### Approximation to Fourier Transform With Higher Order Phase Terms

Given the range-Doppler signal derived in Appendix B, the purpose of this appendix is to derive the range Fourier transform of this signal after the chirp scaling phase function has been applied. The result is the SAR transfer function of the chirp scaled signal. In this appendix, higher order terms than those actually used in processing are derived, in order to evaluate the processing errors of the nonlinear FM chirp scaling algorithm in Chapter 7. The higher order phase terms in the range-Doppler signal in Equation (A.235) are shown to decrease as higher powers of a small parameter, and this is used to find an approximation in the method of stationary phase for evaluating the Fourier transform.

The result in this appendix is found for a chirp scaling function with both quadratic and cubic terms, given by

$$\exp[-j\pi q_2(\tau - \tau_{ref})^2 - \frac{j2\pi}{3}q_3(\tau - \tau_{ref})^3]. \quad (\text{B.236})$$

The use of a cubic term in the chirp scaling function is described in Chapters 6 and 7. Thus, given the range-Doppler signal in Equation (A.235), the integral that needs to be evaluated is

$$\begin{aligned} S_{2Y\alpha}(f_\eta, f_\tau; r) = & F_{ac}(f_\eta; r) \int m \left[ \frac{K_m}{K}(\tau - \tau_d) - \frac{Y_m K_m^3}{K}(\tau - \tau_d)^2 \right] \\ & \exp[-j2\pi f_\tau \tau - j\pi K_m(\tau - \tau_d)^2 - j\pi q_2(\tau - \tau_{ref})^2] \\ & \exp\left[\frac{-j2\pi}{3}Y_m K_m^3(\tau - \tau_d)^3 - \frac{j2\pi}{3}q_3(\tau - \tau_{ref})^3\right] \\ & \exp[-j\pi Y_m^2 K_m^5(\tau - \tau_d)^4] d\tau. \end{aligned} \quad (\text{B.237})$$

Furthermore, to model the range dependence of the range frequency rate,  $K_m$  will be expressed as

$$K_m = K_{mref} + K_s \Delta\tau \quad (\text{B.238})$$

as described in Chapter 5. Also, it will be assumed that

$$K_s \Delta \tau \ll K_{mref}, \quad (\text{B.239})$$

so that the approximation

$$(K_{mref} + K_s \Delta \tau)^n \approx K_{mref}^n \left(1 + \frac{n K_s \Delta \tau}{K_{mref}}\right) \quad (\text{B.240})$$

can be made.

The stationary point is found by solving:

$$\begin{aligned} 0 = & f_\tau + (K_{mref} + K_s \Delta \tau)(\tau - \tau_d) + q_2(\tau - \tau_{ref}) \\ & + Y_m (K_{mref} + K_s \Delta \tau)^3 (\tau - \tau_{ref})^2 + q_3(\tau - \tau_{ref})^2 \\ & + 2Y_m^2 (K_{mref} + K_s \Delta \tau)^5 (\tau - \tau_d)^3. \end{aligned} \quad (\text{B.241})$$

To approximate the solution for the stationary point, it is first necessary to rearrange this equation so that a small parameter can be identified. To do this, normalize the range time by the pulse length in the range-Doppler domain. That is, let  $\zeta$  be a normalized time variable so that

$$\zeta = \frac{\tau - \tau_{ref}}{T_m}. \quad (\text{B.242})$$

Then, from the condition on  $Y_m$  in Equation (7.184), let

$$\epsilon = Y_m K_{mref}^2 T_m. \quad (\text{B.243})$$

With these definitions, and keeping terms up to  $\epsilon^2$  or  $\epsilon \frac{K_s \Delta \tau}{K_{mref}}$ , an equation for the stationary point in normalized time can be found to be

$$\begin{aligned} 0 = & 2\epsilon^2 \zeta^3 \\ & + \epsilon \left(1 + \frac{3K_s \Delta \tau}{K_{mref}} + \frac{q_3}{Y_m K_{mref}^3} - 6Y_m K_{mref}^2 \Delta \tau\right) \zeta^2 \\ & + \left(1 + \frac{q_2}{K_{mref}} + \frac{K_s \Delta \tau}{K_{mref}} - 2Y_m K_{mref}^2 \Delta \tau \left(1 + \frac{3K_s \Delta \tau}{K_{mref}}\right) + 6Y_m^2 K_{mref}^4 \Delta \tau^2\right) \zeta \\ & + \left(\frac{f_\tau}{K_m T_m} - \left(1 + \frac{K_s \Delta \tau}{K_{mref}}\right) \frac{\Delta \tau}{T_m} + Y_m K_{mref}^2 \frac{\Delta \tau^2}{T_m} \left(1 + \frac{3K_s \Delta \tau}{K_{mref}}\right) - 2Y_m^2 K_{mref}^4 \frac{\Delta \tau^3}{T_m}\right). \end{aligned} \quad (\text{B.244})$$

This cubic equation in  $\zeta$  has the form

$$2\epsilon^2\zeta^3 + \epsilon a\zeta^2 + b\zeta + c = 0, \quad (\text{B.245})$$

in which the cubic and quadratic coefficients include higher powers of the small parameter  $\epsilon$ . An approximate solution to this equation can be found by iterating, keeping terms up to  $\epsilon^2$ . Begin by solving for the first power of  $\zeta$ , taking higher powers to the other side of the equation:

$$\zeta \approx -\frac{c}{b} - \frac{\epsilon a}{b}\zeta^2 - \frac{2\epsilon^2}{b}\zeta^3. \quad (\text{B.246})$$

Then substitute this approximation for  $\zeta$  into the higher order terms on the right hand side of the equation:

$$\zeta \approx -\frac{c}{b} - \frac{\epsilon a}{b}\left(-\frac{c}{b} - \frac{\epsilon a}{b}\zeta^2\right)^2 - \frac{2\epsilon^2}{b}\left(-\frac{c}{b}\right)^3. \quad (\text{B.247})$$

Repeating this iteration once more and rearranging gives the following approximate solution for  $\zeta$ :

$$\zeta \approx -\frac{c}{b} - \frac{\epsilon a c^2}{b^3} + \frac{2\epsilon^2 c^3(1-a^2)}{b^4}. \quad (\text{B.248})$$

Substituting for the coefficients,  $a$ ,  $b$ , and  $c$ , and then using the definition of  $\zeta$  gives the stationary point.

Substituting the stationary point into the integrand gives the SAR transfer function of the chirp scaled signal. To simplify the form of the solution, let it be represented as

$$S_{2Y\alpha}(f_\eta, f_\tau; r) = F_{ac}(f_\eta; r)M\left(\frac{f_\tau - \delta f_\tau}{\alpha_B}\right) \exp[j\phi_{cs}(f_\eta, f_\tau; r) + j\phi_{cub}(f_\eta, f_\tau; r) + j\phi_{err}(f_\eta, f_\tau; r)]. \quad (\text{B.249})$$

Here  $\phi_{cs}(f_\eta, f_\tau; r)$  is the phase for the original chirp scaling algorithm without the cubic phase term, including scatterer position:

$$\phi_{cs}(f_\eta, f_\tau; r) = \frac{\pi f_\tau^2}{\alpha_B K_{mref}} - 2\pi\left(\frac{\Delta\tau}{\alpha_B} + \tau_{ref}\right)f_\tau - \pi K_{mref}\left(1 - \frac{1}{\alpha_B}\right)\Delta\tau^2. \quad (\text{B.250})$$

Here  $\alpha_B$  is the modified linear scaling factor derived in Chapter 6, and for a constant  $B$  it reduces to  $\alpha$ . It is related to only the quadratic coefficient of the chirp scaling phase function,

$q_2$ , as shown in Chapter 7. The  $\phi_{cub}(f_\eta, f_\tau; r)$  term in the SAR transfer function includes terms that arise from that cubic phase term, and which are used in processing in the nonlinear FM chirp scaling algorithm:

$$\begin{aligned} \phi_{cub}(f_\eta, f_\tau; r) = & \frac{2\pi(q_3 + Y_m K_{mref}^3) f_\tau^3}{3\alpha_B^3 K_{mref}^3} \\ & - \frac{2\pi}{\alpha_B^3 K_{mref}^2} (0.5\alpha_B K_s - Y_m K_{mref}^3 (\alpha_B - 1) + q_3) \Delta\tau f_\tau^2 \\ & - \frac{2\pi}{\alpha_B^3 K_{mref}} (K_s \alpha_B (\alpha_B - 1) - Y_m K_{mref}^3 (\alpha_B - 1)^2 - q_3) \Delta\tau^2 f_\tau \\ & - \frac{2\pi}{3\alpha_B^3} (1.5K_s \alpha_B (\alpha_B - 1)^2 - Y_m K_{mref}^3 (\alpha_B - 1)^3 + q_3) \Delta\tau^3. \quad (\text{B.251}) \end{aligned}$$

As shown in Chapter 7, the nonlinear FM coefficient,  $Y_m$ , and the cubic coefficient of the chirp scaling phase function,  $q_3$ , are chosen to remove range dependencies of RCMC and SRC. Finally,  $\phi_{err}(f_\eta, f_\tau; r)$  represents higher order terms in  $f_\tau$  and  $\Delta\tau$  than are accommodated in the nonlinear FM chirp scaling algorithm, and thus represent processing errors:

$$\begin{aligned} \phi_{err}(f_\eta, f_\tau; r) = & \pi c_4 f_\tau^4 \\ & - 2\pi(2K_{mref} c_4 + c_3) \Delta\tau f_\tau^3 \\ & + 2\pi(3K_{mref}^2 c_4 + 3K_{mref} c_3 - c_2) \Delta\tau^2 f_\tau^2 \\ & - 2\pi(2K_{mref}^3 c_4 + 3K_{mref}^2 c_3 - 2K_{mref} c_2 - c_1) \Delta\tau^3 f_\tau, \quad (\text{B.252}) \end{aligned}$$

The coefficients in this expression,  $c_1$  to  $c_4$ , are given by:

$$\begin{aligned} c_4 = & \frac{(q_3 + Y_m K_{mref}^3)^2 - \alpha_B Y_m^2 K_{mref}^6}{\alpha_B^5 K_{mref}^5} \\ c_3 = & \frac{(q_3 - (\alpha_B - 1) Y_m K_{mref}^3)(K_s - 2Y_m K_{mref}^3)}{\alpha_B^4 K_{mref}^4} \\ c_2 = & \frac{(q_3 - (3\alpha_B - 1) Y_m K_{mref}^3)(K_s - Y_m K_{mref}^3) - \frac{1}{2}(K_s - 2Y_m K_{mref}^3)^2}{\alpha_B^3 K_{mref}^3} \\ c_1 = & \frac{3\alpha_B Y_m K_{mref}^3 (K_s - \frac{2}{3} Y_m K_{mref}^3) + (K_s - Y_m K_{mref}^3)(K_s - 2Y_m K_{mref}^3)}{\alpha_B^2 K_{mref}^2}. \quad (\text{B.253}) \end{aligned}$$

## Appendix C

### Approximation to Fourier Transform With General Pulse Phase Error

In this appendix the SAR transfer function of the chirp scaled signal is derived for the case of a general, small phase modulation error in the transmitted pulse. Thus, a transmitted pulse of the form

$$p(\tau) = m(\tau) \exp[-j\pi K\tau^2 - j2\pi\varepsilon(\tau)] \quad (\text{C.254})$$

is assumed.

First, the Fourier transform of the pulse is found, which requires evaluation of the integral:

$$P(f_\tau) = \int m(\tau) \exp[-j\pi K\tau^2 - j2\pi\varepsilon(\tau) - j2\pi f_\tau\tau] d\tau. \quad (\text{C.255})$$

The equation for the stationary point is

$$K\tau + \varepsilon'(\tau) + f_\tau = 0, \quad (\text{C.256})$$

for which an approximate solution is desired. To take advantage of the fact that the pulse error is small compared to the pulse phase, let  $\varepsilon(\tau)$  be represented as

$$\varepsilon(\tau) = \epsilon\rho(\tau), \quad (\text{C.257})$$

where  $\epsilon$  is a small parameter. First, approximate the solution for the stationary point by iterating, in which  $\tau$  is solved for as follows:

$$\tau \approx \frac{-f_\tau}{K} - \frac{\epsilon}{K} \rho' \left( \frac{-f_\tau}{K} - \frac{\epsilon}{K} \rho'(\tau) \right). \quad (\text{C.258})$$

Then, to evaluate this expression further, expand the second term in a series about  $\frac{-f_\tau}{K}$  to give the following result after the first iteration:

$$\tau \approx \frac{-f_\tau}{K} - \frac{\epsilon}{K} \rho' \left( \frac{-f_\tau}{K} \right) + \frac{\epsilon^2}{K^2} \rho'' \left( \frac{-f_\tau}{K} \right) \rho'(\tau). \quad (\text{C.259})$$

Proceeding in this way, it can be seen that higher order terms in the approximation decrease as higher powers of the small parameter  $\epsilon$ , thus forming an asymptotic expansion for the stationary point. Keeping only the first term in  $\epsilon$  and substituting for the stationary point in the integrand gives an approximation for the Fourier transform of the pulse:

$$P(f_\tau) = M(f_\tau) \exp\left[\frac{j\pi f_\tau^2}{K} - j2\pi\epsilon\left(\frac{-f_\tau}{K}\right)\right], \quad (\text{C.260})$$

where the effect of the pulse phase error on the amplitude has been ignored.

The next step is the substitution of  $P(f_\tau)$  into the expression for the SAR transfer function in Equation (2.43), and an inverse range Fourier transform of the result to get the range-Doppler domain representation of the signal for this case. Thus, the integral

$$S(f_\eta, \tau; r) = F_{ac}(f_\eta; r) \int M(f_\tau) \exp\left[j2\pi f_\tau(\tau - \tau_d) + \frac{j\pi f_\tau^2}{K_m} - j2\pi\epsilon\left(\frac{-f_\tau}{K}\right)\right] df_\tau, \quad (\text{C.261})$$

needs to be evaluated, and the stationary point is found from

$$(\tau - \tau_d) + \frac{f_\tau}{K_m} + \frac{1}{K}\epsilon\left(\frac{-f_\tau}{K}\right) = 0. \quad (\text{C.262})$$

Using the method of approximation described above and keeping first order terms, an approximation to the stationary point is

$$f_\tau \approx -K_m(\tau - \tau_d) - \frac{K_m}{K}\epsilon'\left(\frac{K_m}{K}(\tau - \tau_d)\right). \quad (\text{C.263})$$

Substituting this into the integrand, the range-Doppler signal becomes

$$S(f_\eta, \tau; r) = F_{ac}(f_\eta; r) m\left[\frac{K_m}{K}(\tau - \tau_d)\right] \exp\left[-j\pi K_m(\tau - \tau_d)^2 - j2\pi\epsilon\left(\frac{K_m}{K}(\tau - \tau_d)\right)\right]. \quad (\text{C.264})$$

Finally, the chirp scaling phase function,

$$\exp[-j\pi q_2(\tau - \tau_{ref})^2] \quad (\text{C.265})$$

is applied and a range Fourier transform is taken of the result to get the SAR transfer function of the chirp scaled signal:

$$S_{2\alpha}(f_\eta, f_\tau; r) = F_{ac}(f_\eta; r) \int m\left[\frac{K_m}{K}(\tau - \tau_d)\right] \exp\left[-j\pi K_m(\tau - \tau_d)^2 - j\pi q_2(\tau - \tau_{ref})^2\right] \exp\left[-j2\pi\epsilon\left(\frac{K_m}{K}(\tau - \tau_d)\right) - j2\pi f_\tau \tau\right] d\tau. \quad (\text{C.266})$$

The stationary point is found from

$$K_m(\tau - \tau_d) + q_2(\tau - \tau_{ref}) + \frac{K_m}{K} \varepsilon' \left( \frac{K_m}{K} (\tau - \tau_d) \right) + f_\tau = 0, \quad (\text{C.267})$$

which has the following approximation, using the method described above:

$$\tau \approx \frac{-f_\tau}{\alpha K_m} + \frac{\Delta\tau}{\alpha} + \tau_{ref} - \frac{1}{\alpha K} \varepsilon' \left( \frac{-f_\tau}{\alpha K} - \frac{K_m}{K} \left(1 - \frac{1}{\alpha}\right) \Delta\tau \right). \quad (\text{C.268})$$

In this expression, the relationship between  $\alpha$  and the coefficient of the chirp scaling function,  $q_2$  has been used to simplify notation. Substituting for the stationary point in the integrand gives the SAR transfer function. The result is the same as the expression in Equation (3.95), except for an extra phase term which represents the processing error due to the pulse phase error:

$$\phi_{err} = -2\pi \varepsilon \left[ \frac{-f_\tau}{\alpha K} - \frac{K_m}{K} \left(1 - \frac{1}{\alpha}\right) \Delta\tau \right]. \quad (\text{C.269})$$